

UNIVERSITÀ DEGLI STUDI DI UDINE  
DOTTORATO DI RICERCA IN SCIENZE  
DELL'INGEGNERIA ENERGETICA E AMBIENTALE



**DEVELOPMENT OF A HYBRID  
CONTINUUM-KINETIC SOLVER FOR  
MICRO GAS FLOW SIMULATION**

Dott.ssa Olga Rovenskaya

COMMISSIONE

---

Prof. Irina Graur Martin	REVISORE
Dr. Vladimir Titarev	REVISORE
Prof. Luca Brandt	COMISSARIO
Dr. Cristian Marchioli	COMISSARIO
Dr. Francesco Picano	COMISSARIO
Prof. Giulio Croce	SUPERVISORE

---

Prof. Alfredo Soldati	COORDINATORE DEL DOTTORATO
-----------------------	----------------------------



## Abstract

The aim of the present work is to produce a general, robust and efficient solver allowing to simulate non-continuum, multi-scale flows for diverse engineering applications. The wide development of MEMS application requires special methods for an investigation of the flow in them, since the rarefaction plays a major role in such flow and the Navier-Stokes equations even provided with slip boundary conditions become invalid in the whole flow field.

The methodology used involves the decomposition of a physical domain into kinetic and hydrodynamic sub-domains by computing appropriate criteria, based on the local Knudsen number and gradients of macroparameters. The size of sub-domains will change during the evolution depending on the current value of the criterion. The hybrid solver is the combination of a kinetic solver for the S-model of the Boltzmann kinetic equation (based on the discrete velocity method) and a Navier–Stokes solver based on a hybrid finite-difference finite volume scheme. The solution is advanced in time simultaneously in both kinetic and hydrodynamic domains and the coupling is achieved by matching half fluxes at the interface of the kinetic and Navier–Stokes sub-domains, thus taking care of the conservation of momentum, energy and mass through the coupling interface. Parallelization via MPI (Message Passing Interface) increases the efficiency of the hybrid solver, thus making simulations of complex geometry feasible.

The hybrid solver is validated via the numerical investigation of gas flow through a slit in a wide range of pressure ratio, including flow into vacuum and Knudsen number from slip to transitional regime. The capability of hybrid solver as applied to vacuum science problems is demonstrated. Furthermore, the hybrid solver is applied for the investigation of the effect of the surface roughness. The competition between compressibility, rarefaction and roughness effects is analysed. The improvement in accuracy over Navier-Stokes equations and the computational efficiency of the proposed hybrid solver is assessed via comparison with a pure kinetic solution. Thus, the elaborated hybrid solver demonstrates capabilities to predict numerical results close to kinetic ones up to 10 times quicker.

# Contents

Nomenclature.....	6
1. Introduction .....	10
1.1. Hybrid solver strategies .....	11
1.2. Objectives of the present work .....	12
2. Hybrid solver methodology .....	14
2.1. Coupling technique .....	14
2.2. Breakdown parameter .....	18
3. Hybrid solver implementation .....	20
3.1. Kinetic solver .....	20
3.1.1. Governing equations and boundary conditions .....	20
3.1.2. Numerical scheme .....	25
3.2. Navier-Stokes solver .....	29
3.2.1. Governing equations and boundary conditions .....	29
3.2.2. Numerical scheme .....	31
3.3. MPI parallelization .....	32
4. Validation: gas flow through the slit .....	34
4.1. Introduction.....	34
4.2. Statement of the problem.....	36
4.3. Parameters of modelling .....	37
4.4. Results and discussion .....	39
4.5. Conclusions.....	49
5. Near wall modelling .....	50
5.1. Introduction.....	50
5.2. Statement of the problem.....	54
5.2. Parameters of modelling .....	57
5.3. Breakdown criteria comparison .....	58
5.4. Hybrid results discussion .....	61

5.4.1. Smooth channel .....	61
5.4.2. Flow over a rough surface .....	69
5.5. Conclusion .....	89
Conclusions .....	91
References .....	93
List of Publications .....	100

# Nomenclature

## *Roman Symbols*

$A_k$	computational cell face area, $\text{m}^2$
$\mathbf{c} = \xi - \mathbf{V}$	relative speed of a single particle against a background gas, $\text{m/s}$
CFL	Courant - Friedrichs - Lewy number, dimensionless
$C(\Delta t)$	collision step
$c_v$	specific heat capacity at constant volume
$d$	artificial dissipation term
$e_{tot}$	macroscopic total energy, $\text{J/m}^3$
$e_{int}$	macroscopic internal energy, $\text{J/kg}$
$f(t, \mathbf{x}, \xi)$	particle velocity distribution function, $\text{s}^3/\text{m}^6$
$fr$	friction coefficient, dimensionless
$\mathbf{F}(\mathbf{U})$	flux
$J$	determinant of the Jacobian matrices
$H$	height of the channel, $\text{m}$
$\mathbf{I}$	identity matrix
$I_c$	coupling interface, $\text{m}$
$J(f, f)$	Boltzmann collision integral
$J_s(f, f)$	S model of Boltzmann collision integral
$k$	Boltzmann constant, $1.38 \cdot 10^{-23} \text{J/K}$
$Kn$	Knudsen number, dimensionless
$M(t, \mathbf{x}, \xi)$	Maxwellian distribution function, $\text{s}^3/\text{m}^6$
$Ma$	Mach number, dimensionless

$m$	mass of the particle, kg
$n$	local number density, $1/\text{m}^3$
$N_c$	number of cells in physical space
$N_\xi$	number of velocity nodes
$N_p$	number of processes
$p$	pressure, Pa
$Po$	Poiseuille number, dimensionless
$\mathbf{q}$	heat flux vector, $\text{W}/\text{m}^2$
$R = k/m$	ideal gas constant, $8.3145 \text{ J}/\text{mol K}$
$f^s(t, \mathbf{x}, \xi)$	Shakhov distribution function, $\text{s}^3/\text{m}^6$
$\mathbf{s}(\xi)$	collision vector
$s$	Van Albada limiter
$s_T$	temperature jump coefficient, dimensionless
$s_p$	slip coefficient, dimensionless
$t$	time, s
$T$	temperature, K
$T(\Delta t)$	transport step
$\mathbf{U}$	vector of conservative macroscopic variables
$u_\zeta, u_\eta$	component of flow velocity tangential and normal to the surface, m/s
$\mathbf{V} = (u, v, w)$	macroscopic bulk velocity vector, m/s
$\mathbf{x} = (x, y, z)$	position vector, m

### ***Greek Symbols***

$\Gamma = (\alpha, \beta)$	velocity grid point indices
----------------------------	-----------------------------

$\gamma$	specific heat ratio, dimensionless
$\delta_{ij}$	Kronecker delta
$\delta$	rarefaction parameter, dimensionless
$\varepsilon$	relative roughness, dimensionless
$\Xi$	threshold value, dimensionless
$\eta(\mathbf{x})$	outward normal vector, m
$\kappa$	thermal conductivity, W/(m·K)
$\Lambda_{ij}$	computational cell volume, m <sup>3</sup>
$\lambda$	mean free path, m
$\mu$	gas viscosity, kg/m s
$\xi$	particle velocity vector, m/s
$\xi_x, \xi_y, \xi_z$	components of particle velocity vector, m/s
$\rho$	density, kg/m <sup>3</sup>
$\sigma_T$	temperature accommodation coefficient
$\sigma_v$	part of incident particles scattered diffusely
$\tau$	shear stress tensor, N/m <sup>2</sup>
$\Omega_K$	kinetic domain, m <sup>2</sup>
$\Omega_{NS}$	Navier-Stokes domain, m <sup>2</sup>
$\zeta(\mathbf{x})$	tangential vector, m

***Subscripts***

$CE$	Chapman-Enskog
$c$	coupling

<i>e</i>	exit
<i>i</i>	incoming
inv	inviscid (convective)
K	kinetic
NS	Navier-Stokes
<i>o</i>	outcoming
<i>p</i>	process
s	smooth
<i>v</i>	velocity, volume
vis	viscous (diffusive)
<i>w</i>	wall
0	total value, equilibrium state

### ***Superscripts***

<i>T</i>	transposed
<i>S</i>	S-model

### ***Abbreviations***

CFD	Computational Fluid Dynamics
CFL	Courant-Friedrichs-Lewy
DSMC	Direct Simulation Monte-Carlo
DVM	Discrete Velocity Method
MEMS	Micro-electro-mechanical-systems
MUSCL	Monotonic Upstream-Centered Scheme for Conservation Laws
TVD	Total variation diminishing

# 1. Introduction

Current development in micro and nano technologies have dramatically increased possible applications of micro scale flow simulations, from micro-electro-mechanical-systems (MEMS) devices to genuinely multi-scale problems. Despite the recent success in numerical/experimental investigation of MEMS a micro gaseous flow simulation still represents a major challenge, and is the main topic of several research projects at international level.

The coexistence of rarefied and continuum flow regime areas is a typical feature of gas flow in micro systems. Near wall flows offer additional complexity due to appearance of highly rarefied region near the solid wall: the flow near a solid surface can be divided into a thin boundary layer, of the order of a few mean free path (so thin to be negligible for a macro configuration), which is a rarefied regime area and the internal core flow, which can be considered as continuum one.

It is well known that, unfortunately, kinetic solvers, even for model kinetic equations, involve a considerable effort in terms of CPU time and memory requirements, due to the discretization in both physical and velocity spaces. On the other hand, hydrodynamics Euler or Navier–Stokes equations, describing the flow in terms of mere average gas velocity, density and temperature, are much more efficient, but less accurate in rarefied areas. However, the inaccuracy of Navier–Stokes equations in boundary layer can be partially overcome by introducing slip boundary and temperature jump conditions on the solid surface. Nonetheless, as indicated in the literature, slip conditions are valid only for local Knudsen numbers  $Kn$  less than 0.1, and any attempts to increase their range, resorting to higher order slip boundary conditions, is not trivial and highly geometrical dependent.

On the other hand, in many applications rarefied areas cover only a limited portion of the whole computational domain; therefore, the development of hybrid solvers applying a kinetic model in the region with a high rarefaction, while keeping continuum model in the rest of the

flow, allow us to simulate flows with an accuracy close to the full kinetic consideration and computational expenses close to continuum ones. The development of hybrid solvers combining kinetic and continuum models has become an important area of research over the last decade, see, e.g., [1-14].

Potential applications of such solvers range from gas flows in complex micro systems to aerospace applications, such as high altitude flights. Major challenges in the development of hybrid code are the identification of kinetic and continuum domains and the choice of the coupling technique. The key parameter defining the choice of the appropriate physical model is usually related to some definition of a local Knudsen number, although more complex approaches have been suggested as well [7].

## **1.1. Hybrid solver strategies**

Different methods presented so far in the open literature can be classified into three categories. The first relies on the domain decomposition in a physical space: the computational domain is thus decomposed into kinetic and continuum sub-domains using appropriate criteria [1-12]. The second is based on the domain decomposition in a velocity space, where fast and slow particles are treated separately [13]. The third category includes hybrid models: both kinetic and fluid equations are solved in the entire domain, using a velocity distribution function to compute transport coefficients for fluid equations [14-16]. However, most of published works fall into the first category.

Typically, particle methods such as Direct Simulation Monte-Carlo (DSMC) method or Molecular Dynamics are used in regions with strong deviation from equilibrium, and a continuum fluid dynamics CFD (Euler or Navier-Stokes, depending on problem features) solver is used elsewhere, e.g., [1-6]. Nonetheless, the direct numerical solution of kinetic equations [17-21] is a viable alternative to the DSMC method and may be preferable to DSMC method, for coupling purposes, since both kinetic and continuum models use similar numerical techniques.

In the past few years, several attempts have been presented for coupled continuum and kinetic methods (see, e.g., [8-11]). It should be noticed that they are limited by applying a coupled methodology on a simulation with fixed chosen kinetic and continuum domains or special “kinetic” treatment of Navier -Stokes equations. A combination of the numerical solution of the Boltzmann equation and its model with kinetic schemes of continuum fluid dynamics was presented in [8, 9]. From the very beginning in [10, 11] a direct Boltzmann solver was combined with a Navier-Stokes solver using a priori decomposition of the domain, chosen on the basis of a previous continuum solution and not updated during the computation. Further, an improved over [10, 11] version of hybrid solver, including a dynamically decomposition of the physical domain into kinetic and continuum sub-domains by computing gradient-length Knudsen number  $Kn_{GL}$  based on the local Knudsen number and macroparameters gradients [6, 7] was used in [12] for a wall boundary independent problem (the gas flow through the slit).

Thus, the development of the multiscale hybrid solver capable of the accurate and efficient simulation of non-continuum flows for engineering technologies is an open problem in scientific community. The multi-scalability is a main feature of micro gaseous flows and often encountered in actual application of practical interest, such as effect of surface roughness on the gas flow. In this case, the macroscales, or continuum flows are well described by Navier-Stokes equations provided with appropriate slip boundary conditions, while microscales are described by more general kinetic equations.

## **1.2. Objectives of the present work**

The main challenges in the development of hybrid code are the identification of kinetic and continuum domains, as well as the choice of a proper coupling between these domains. The advantage of the present hybrid algorithm is that it allows to couple existing in-house codes for the numerical solution of the Boltzmann kinetic (and its models) and Navier-Stokes equations.

This research project is therefore aimed at the elaboration of a novel and sustainable multiscale solver for MEMS problems coupling a solver for the S-model of kinetic and Navier-Stokes equations, with the objectives of:

1. Developing multiscale coupling technique, allowing flexible changing the size of continuum and kinetic domains, depending on the flow regime.
2. Increasing the efficiency of the solver by parallelization using MPI (Message Passing Interface) for computation on multiprocessors systems, making it tractable for complex two/three-dimensional flow problems;
3. Validation of developed solver via comparison with well known problems;
4. Application of hybrid solver for diverse engineering problems;
5. Estimate the reliability of first order slip boundary conditions for the simulation of flows along of fine-textured geometries;

## 2. Hybrid solver methodology

### 2.1. Coupling technique

The coupling strategy between kinetic and continuum solvers is completely general, and can be applied to either the full Boltzmann kinetic equation or its different models and either Navier-Stokes (NS) or Euler equations. In this section the main ideas allowing to elaborate a hybrid solver are presented.

The flow of rarefied gas starting from the equilibrium initial condition is described by the Boltzmann transport equation [22]:

$$\frac{\partial f}{\partial t} + \xi \frac{\partial f}{\partial \mathbf{x}} = J_B(f, f), \quad (1)$$

$$f(0, \mathbf{x}, \xi) = M(\rho_0, \mathbf{c}_0, T_0). \quad (2)$$

where  $f = f(t, \mathbf{x}, \xi)$  is the velocity distribution function, i.e. the probability of finding a molecule with velocity  $\xi = (\xi_x, \xi_y, \xi_z) \in \mathbf{R}^3$  in the position  $\mathbf{x} = (x, y, z)$  at the time  $t$ ,  $J_B(f, f)$  is the Boltzmann collision integral,  $M(\rho_0, \mathbf{c}_0, T_0)$  is the equilibrium Maxwell distribution function,  $\rho_0$ ,  $\mathbf{c}_0 = \xi - \mathbf{V}_0$  and  $T_0$  are the equilibrium gas density, peculiar velocity, i.e., the relative speed of a single molecule against a background gas with bulk velocity  $\mathbf{V}_0 = (u_0, v_0, w_0)$  and temperature, respectively.

In kinetic description of the gas flow the macroscopic density, momentum, internal energy  $e$  per unit mass and heat flux are defined by integration over whole velocity space  $\mathbf{R}^3 \in [-\infty; \infty]$  as following [22]:

$$\rho = \int f d\xi, \quad \rho(u, v)^T = \int (\xi_x, \xi_y)^T f d\xi, \quad \rho e = \frac{1}{2} \int \mathbf{c}^2 f d\xi, \quad (q_x, q_y)^T = m \int (c_x, c_y)^T \mathbf{c}^2 f d\xi \quad (3)$$

According to the Chapman-Enskog theory [23] Navier-Stokes equations are the first order approximation of the Boltzmann kinetic equation. The Chapman-Enskog (CE) velocity distribution function  $f_{CE}(\mathbf{C})$  can be written as:

$$f_{CE}(\mathbf{C}) = M(\rho, \mathbf{c}, T)(1 + f_1(\mathbf{C})) = M(\rho, \mathbf{c}, T)\Psi(\mathbf{C}), \quad \mathbf{C} = \mathbf{c}\sqrt{\frac{m}{2kT}} \quad (4)$$

$$M(\rho, \mathbf{c}, T) = \frac{\rho}{(2\pi kT/m)^{3/2}} \exp(-\mathbf{C}^2), \quad (5)$$

$$f_1(\mathbf{C}) = q_i^* C_i \left( \frac{2}{5} \mathbf{C}^2 - 1 \right) - \tau_{ij}^* C_i C_j, \quad (6)$$

$$\tau_{ij}^* = \frac{\mu}{p} \left( \frac{\partial u_i}{\partial x_j} + \frac{\partial u_j}{\partial x_i} - \frac{2}{3} \delta_{ij} \frac{\partial u_k}{\partial x_k} \right), \quad q_i^* = -\frac{\kappa}{p} \sqrt{\frac{2m}{kT}} \frac{\partial T}{\partial x_i} \quad (7)$$

where  $\rho$ ,  $T$  and  $p$  is the gas density, temperature and pressure, respectively,  $\mathbf{c} = \boldsymbol{\xi} - \mathbf{V}$  is the relative speed of a single molecule against a background gas with bulk velocity  $\mathbf{V} = (u, v, w)$ ,  $f_1(\mathbf{C})$  is the correction term,  $\tau_{ij}^*$  is the normalized shear stress tensor,  $\delta_{ij}$  is the Kronecker delta,  $q_i^*$  is the normalized heat flux vector,  $\mu$  is the dynamic viscosity and  $\kappa$  is the thermal conductivity of the gas at temperature  $T$ ; for monatomic gas  $\kappa$  can be computed as  $(5/2) \mu c_v$ , where  $c_v$  is the specific heat capacity at constant volume (for monatomic gas  $c_v = 3k/2m$ ),  $k$  is the Boltzmann constant. Substituting  $f_{CE}(\mathbf{C})$  in equation (1) and multiplying by the collision vector  $\mathbf{s}(\boldsymbol{\xi}) = (1, \boldsymbol{\xi}, \boldsymbol{\xi}^2/2)$ , integration over the whole velocity domain  $\mathbb{R}^3 \in [-\infty; \infty]$  recovers the usual conservation laws of mass, momentum and energy:

$$\frac{\partial}{\partial t} \left( \int_{\mathbb{R}^3} f_{CE} \varphi^T d\boldsymbol{\xi} \right) + \frac{\partial}{\partial \mathbf{x}} \int_{\mathbb{R}^3} f_{CE} \boldsymbol{\xi} s^T d\boldsymbol{\xi} = 0. \quad (8)$$

The use of  $f_{CE}$  ensures that equation (7) is equivalent to the usual conservative form of Navier-Stokes equations:

$$\frac{\partial \mathbf{U}}{\partial t} + \frac{\partial \mathbf{F}(\mathbf{U})}{\partial \mathbf{x}} = 0, \quad (9)$$

$$\mathbf{U} = \int f_{CE} \mathbf{s}^T d\xi = (\rho, \rho \mathbf{V}, \rho(e + \mathbf{V}^2 / 2))^T, \quad (10)$$

$$\mathbf{F}(\mathbf{U}) = \int \xi f_{CE} \mathbf{s}(\xi)^T d\xi, \quad (11)$$

where  $\mathbf{U}$  is the vector of macroscopic values,  $\mathbf{F}(\mathbf{U})$  is the flux vector.

The sketch of coupling procedure between kinetic domain  $\Omega_K$  and continuum (NS) domain  $\Omega_{NS}$  is shown in Fig. 1. To solve a kinetic equation in a physical cell  $x_{i+1} \in \Omega_K$  we need to know the distribution function of incoming particles from the neighbouring cell  $x_i \in \Omega_{NS}$  (see Fig. 1). On the coupling interface  $I_c$  this information has to be provided by the continuum solution; thus, assuming that equation (8) holds true in the continuum sub-domain we impose a Chapman–Enskog distribution function  $f_{CE}$ , equation (4):

$$f|_{I_c}(\mathbf{x}) = f_{CE}(x_i) \quad \text{if } \xi \cdot \boldsymbol{\eta}(\mathbf{x}) > 0 \quad (12)$$

where  $\boldsymbol{\eta}(\mathbf{x})$  is the inward normal vector to the boundary of  $\Omega_K$  (see Fig. 1). Macroscopic values  $\rho$ ,  $\mathbf{V}$ ,  $T$  appearing in the CE distribution function  $f_{CE}(x_i)$  are computed at the grid point  $x_i \in \Omega_{NS}$  and the evaluation of macroparameters gradients ( $\partial T / \partial \mathbf{x}$  and  $\partial \mathbf{V} / \partial \mathbf{x}$ ) involves also values in the neighbor to  $x_i$  points, i.e.  $x_{i-1}$  and  $x_{i+1}$ .

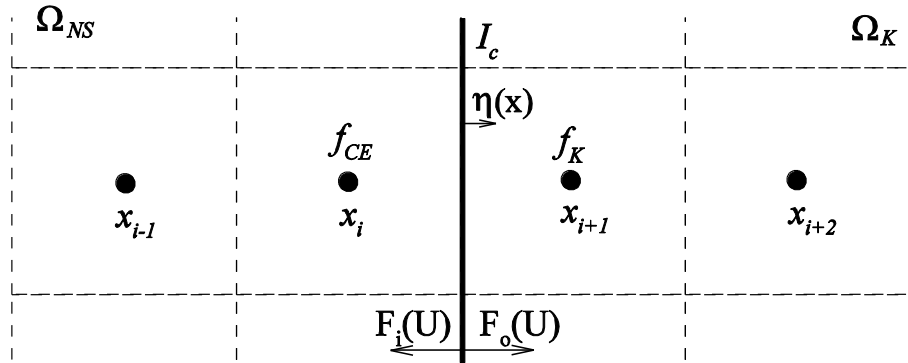


**Fig. 1.** Hybrid coupling procedure.

The interface  $I_c$  position depends on the value of breakdown parameter, recomputed at each time step (the choice of breakdown parameter and its effect on hybrid solution will be discussed later); thus, it may happen that some nodes considered as continuum at previous time step can

become kinetic ones at the current time step. In this case, the kinetic distribution function in “new” kinetic nodes will be initialized as the CE distribution function  $f_{CE}(\mathbf{x})$  computed using current macroscopic values  $\rho$ ,  $\mathbf{V}$ ,  $T$  and their gradients.

Thus, at the coupling interface  $I_c$  the following boundary condition is imposed:

$$\mathbf{F}(\mathbf{U}) \cdot \boldsymbol{\eta}(\mathbf{x})|_{I_c} = \mathbf{F}_i(\mathbf{U}) \cdot \boldsymbol{\eta}(\mathbf{x}) + \mathbf{F}_o(\mathbf{U}) \cdot \boldsymbol{\eta}(\mathbf{x}) \quad (13)$$

where  $\mathbf{F}_i(\mathbf{U}) \cdot \boldsymbol{\eta}(\mathbf{x})$  and  $\mathbf{F}_o(\mathbf{U}) \cdot \boldsymbol{\eta}(\mathbf{x})$  are incoming and outgoing half fluxes. Thus, the coupling between kinetic and NS solvers is achieved by imposing into  $\Omega_{NS}$  domain the incoming half flux  $\mathbf{F}_i(\mathbf{U}) \cdot \boldsymbol{\eta}(\mathbf{x})$ , predicted by the kinetic solver:

$$\mathbf{F}_i(\mathbf{U}) \cdot \boldsymbol{\eta}(\mathbf{x}) = \int_{\boldsymbol{\xi} \cdot \boldsymbol{\eta}(\mathbf{x}) < 0} \boldsymbol{\xi} \cdot \boldsymbol{\eta}(\mathbf{x}) f(t, \boldsymbol{\xi}, \mathbf{x}) \mathbf{s}(\boldsymbol{\xi})^T d\boldsymbol{\xi} \quad (14)$$

where  $f(t, \mathbf{x}, \boldsymbol{\xi}) \equiv f_K$  is the solution of kinetic equation for molecules exiting from  $\Omega_K$ . The outgoing flux  $\mathbf{F}_o(\mathbf{U}) \cdot \boldsymbol{\eta}(\mathbf{x})$  from  $\Omega_{NS}$  to  $\Omega_K$  domain can be computed as:

$$\mathbf{F}_o(\mathbf{U}) \cdot \boldsymbol{\eta}(\mathbf{x}) = \int_{\boldsymbol{\xi} \cdot \boldsymbol{\eta}(\mathbf{x}) > 0} \boldsymbol{\xi} \cdot \boldsymbol{\eta}(\mathbf{x}) f_{CE}(t, \boldsymbol{\xi}, \mathbf{x}) \mathbf{s}(\boldsymbol{\xi})^T d\boldsymbol{\xi} \quad (15)$$

It can be seen, that the NS model acts on the kinetic one by imposing the incoming Chapman–Enskog function  $f_{CE}$  on the coupling interface  $I_c$ , while the macroscopic parameters  $\rho$ ,  $\mathbf{V}$ ,  $T$  and their gradients for  $f_{CE}$  are computed locally.

If a boundary node at the inlet/outlet falls in continuum domain the conditions are specified according to the Navier-Stokes statement of the problem. If an inlet/outlet boundary node falls in the rarefied domain the Maxwell velocity distribution function is assumed for incoming in computational domain particles with density, temperature and velocity specified by a considered problem.

At solid wall in  $\Omega_K$  domain the Maxwell diffuse reflecting boundary condition with the full accommodation is applied, while in  $\Omega_{NS}$  subdomain the first order slip and Smoluchowski temperature jump boundary conditions are used.

## 2.2. Breakdown parameter

The choice of breakdown criterion, defined the size of kinetic  $\Omega_K$  and  $\Omega_{NS}$  sub-domains, is important since the wrong domain decomposition could lead to a non-positive velocity distribution function or even incorrect numerical results [7]. On the other hand, the overestimation of kinetic domain size results in inefficiency, forcing the use of kinetic solver where a continuum one could have been accurate enough. Therefore, choosing a breakdown parameter along with a threshold value in numerical simulation we always should find the balance between a computational efficiency of the hybrid solver and reliability of the computed results.

One of the options for the breakdown parameter proposed in the open literature is the gradient-length Knudsen number  $Kn_{GL}(\mathbf{x})$  [6, 7]:

$$Kn_{GL}(\mathbf{x}) = \max(Kn_{GL\rho}, Kn_{GLV}, Kn_{GLT}), \quad (16)$$

$$Kn_{GL\rho}(\mathbf{x}) = Kn \frac{|\nabla\rho|}{\rho}, \quad (17)$$

$$Kn_{GL|\mathbf{V}|}(\mathbf{x}) = Kn \frac{|\nabla\mathbf{V}|}{|\mathbf{V}|^*}, \quad (18)$$

$$Kn_{GLT}(\mathbf{x}) = Kn \frac{|\nabla T|}{T}, \quad (19)$$

where  $\rho$  is the local density,  $\mathbf{V} = (u, v, w)$  is the local bulk velocity and  $T$  is the local temperature.

It should be noticed that in the present work  $Kn_{GL}$  is based on the gradient of the velocity magnitude  $|\mathbf{V}|$ , rather than its components as was proposed in [6, 7]. It is clear that the new definition takes into account shear stresses, which are essential for near wall problems. Moreover, in low-speed flow regions, the velocity magnitude gradient in  $Kn_{GL|\mathbf{V}|}$  is normalized by some chosen speed  $v_{\min}$ , in order to avoid singularities where the flow velocity approaches to zero. This is imposed defining  $|\mathbf{V}|^* = |\mathbf{V}|$  if  $|\mathbf{V}| \geq v_{\min}$  and  $|\mathbf{V}|^* = v_{\min}$  if  $|\mathbf{V}| < v_{\min}$ . One of the

possible ways to define  $v_{\min}$  is based on the isentropic velocity, i.e.  $u_{is} = Ma_{is}(\gamma RT_0)^{0.5}$ . Here,  $v_{\min}$  is equal to  $0.05 u_{is}$  considered as sufficiently small.

In [6] the threshold value  $\Xi$  was chosen from the assumption that NS equations are valid up to local Knudsen number  $Kn = 0.05-0.1$ , therefore the kinetic solution was performed where gradient-length Knudsen number  $Kn_{GL}(\mathbf{x}) \geq 0.05$ . However, as will be reported below, the particular choice of the threshold value  $\Xi$  should be supported by preliminary numerical tests.

Another breakdown parameter, proposed in the literature, is based on the CE distribution function [24, 7]. When  $f_1(\mathbf{C})$  (equation (4)) is small, then  $\Psi(\mathbf{C})$  slightly deviates from 1 and NS equations are valid; when  $\Psi(\mathbf{C})$  is sufficiently far from unity then NS equations may fail, and a kinetic approach is required. The direct evaluation of  $f_1(\mathbf{C})$  is difficult and numerically expensive because it is a function of not only flow field gradients but also the random peculiar velocity  $\mathbf{C}$  and therefore, either an average or maximum value of  $f_1(\mathbf{C})$  should be evaluated over the full distribution function. Therefore, in [24, 7] an approximate breakdown parameter based on the normalized shear stress  $\tau_{ij}^*$  and heat flux  $q_i^*$  was proposed:

$$B_{q\tau} = \max(|\tau_{ij}^*|, |q_i^*|) \quad (20)$$

where normalized shear stress  $\tau_{ij}^*$  and heat flux  $q_i^*$  are computed using eqs. (7). The kinetic solution is activated when  $B_{q\tau} > 0.1$ .

Tiwari [25] has proposed another criterion based on the norm of additional term in Chapman-Enskog distribution function  $\|f_1(\mathbf{C})\|$ :

$$\|f_1(\mathbf{C})\| = \frac{1}{\rho RT} \sqrt{\frac{1}{2} |\tau_{ij}|^2 + \frac{2}{5} \frac{|q_i|^2}{RT}} \quad (21)$$

For the continuum approximation to hold this parameter should be much less than unity.

### 3. Hybrid solver implementation

The elaborated hybrid solver is constructed by coupling two in-house codes for the solution of hydrodynamic NS equations and kinetic equation written using FORTRAN and C++ programming languages, respectively. The efficiency of the hybrid solver is enhanced by parallelization via MPI (Message Passing Interface).

#### 3.1. Kinetic solver

##### 3.1.1. Governing equations and boundary conditions

The kinetic solver is based on the numerical solution of the Boltzmann transport equation (1) describing the evolution of particle velocity distribution function  $f=f(t, \mathbf{x}, \boldsymbol{\xi})$  in six dimensional phase space (physical space  $\mathbf{x}=(x, y, z)$  and velocity space  $\boldsymbol{\xi}=(\xi_x, \xi_y, \xi_z)\in\mathbb{R}^3[-\infty;\infty]$ ). The general form of the Boltzmann collision integral is the following [22]:

$$J_B(f, f) = \int_{-\infty}^{\infty} \int_0^{2\pi} \int_0^{b_m} (f(\boldsymbol{\xi}') f(\boldsymbol{\xi}'_1) - f(\boldsymbol{\xi}) f(\boldsymbol{\xi}_1)) g b db d\alpha d\xi_1 \quad (22)$$

where  $\boldsymbol{\xi}, \boldsymbol{\xi}_1, \boldsymbol{\xi}, \boldsymbol{\xi}_1$  are velocities of pair of particles before and after collision,  $g = |\boldsymbol{\xi} - \boldsymbol{\xi}_1|$  is the relative velocity, and  $b, \alpha$  are impact parameters, the distance of the closest approach, bounded by a  $b_m$ , and azimuth angle, respectively. Furthermore, the velocity distribution function  $f=f(t, \mathbf{x}, \boldsymbol{\xi})$  can be treated as the probability of finding a molecule with velocity  $\boldsymbol{\xi}=(\xi_x, \xi_y, \xi_z)$  in the position  $\mathbf{x}=(x, y, z)$  at the time moment  $t$ .

Let us consider the initial-boundary value problem for the Boltzmann transport equation (1) starting from the equilibrium initial condition (2). We discretize time into discrete values  $t^n = n\Delta t$ , and denote by  $f^n(\mathbf{x}, \boldsymbol{\xi})$  an approximation of the distribution function  $f=f(t^n, \mathbf{x}, \boldsymbol{\xi})$ . The standard approach to solve the kinetic equation (1) is the time splitting method, which is

obtained considering, in a small time interval  $t = t^{n+1} - t^n$ , the numerical solution of the transport step:

$$\begin{cases} \frac{\partial f^*}{\partial t} + \xi \frac{\partial f^*}{\partial \mathbf{x}} = 0 \\ f^*(0, \mathbf{x}, \xi) = f^n(\mathbf{x}, \xi) \end{cases} \quad (23)$$

and the space homogeneous collision step:

$$\begin{cases} \frac{\partial f^{**}}{\partial t} + \xi \frac{\partial f^{**}}{\partial \mathbf{x}} = J_B(f^{**}, f^{**}) \\ f^{**}(0, \mathbf{x}, \xi) = f^*(\Delta t, \mathbf{x}, \xi) \end{cases} \quad (24)$$

Denoting  $T(\Delta t)$  and  $C(\Delta t)$  as solution operators (exact or at least second order) corresponding respectively to the transport and collision steps, i.e. we can write:

$$f^*(0, \mathbf{x}, \xi) = T(\Delta t)f^n(\mathbf{x}, \xi) \quad (25)$$

$$f^{**}(\Delta t, \mathbf{x}, \xi) = C(\Delta t)f^*(\Delta t, \mathbf{x}, \xi) \quad (26)$$

The approximated value for the velocity distribution function at next time level  $t^{n+1}$  is then given by:

$$f^{n+1}(\mathbf{x}, \xi) = f^{**}(\Delta t, \mathbf{x}, \xi) = C(\Delta t)T(\Delta t)f^n(\mathbf{x}, \xi) \quad (27)$$

It should be mentioned that a second order scheme in time can be easily derived simply by symmetrizing the first order scheme:

$$f^{n+1}(\mathbf{x}, \xi) = T(\Delta t/2)C(\Delta t)T(\Delta t/2)f^n(\mathbf{x}, \xi) \quad (28)$$

The computation of the Boltzmann collision integral  $J_B(f, f)$  (eq. (22)) is, in general, time and memory consuming. For the sake of simplicity, in the present work, the full Boltzmann collision integral  $J_B(f, f)$  is approximated by the S-model [26], which can be written as:

$$J_S(f, f) = \frac{p}{\mu} \left( M \left( 1 + \frac{2m^2 \mathbf{q} \mathbf{c}}{15\rho(kT)^2} \left( \frac{m\mathbf{c}^2}{2kT} - \frac{5}{2} \right) \right) - f \right) = \frac{p}{\mu} (f^S - f), \quad (29)$$

$$M(\rho, \mathbf{V}, T) = \frac{\rho}{(2\pi kT/m)^{3/2}} \exp\left(-\frac{m\mathbf{c}^2}{2kT}\right). \quad (30)$$

$f^S(\rho, \mathbf{c}, T)$  and  $M(\rho, \mathbf{c}, T)$  are the local Shakhov and Maxwell distribution functions, respectively,  $\rho$ ,  $T$  and  $p$  is the gas density, temperature and pressure, respectively,  $\mathbf{c} = \boldsymbol{\xi} - \mathbf{V}$  is the relative speed of a single molecule with the mass  $m$  against a background gas with bulk velocity  $\mathbf{V} = (u, v, w)$ ,  $\mathbf{q}$  is the heat flux vector,  $\mu$  is the dynamic viscosity of the gas at temperature  $T$ ,  $\kappa = (5/2) \mu c_v$  is the thermal conductivity,  $c_v$  is the specific heat capacity at constant volume (for monatomic gas  $c_v = 3k/2m$ ),  $k$  is the Boltzmann constant. The S-model provides the correct Prandtl number  $\text{Pr} = 2/3$  in contrast to the BGK model [27], but the H-theorem for the S-model was proved only for its linearized form.

To proceed to dimensionless variables scales specified by equilibrium values are introduced. The specific choice of reference values is dictated by the particular problem under consideration and will be additionally indicated further for each considered in the present work problems. Generally speaking we can introduce the following equilibrium values as reference ones: number density  $n_0$ , temperature  $T_0$ , most probable velocity  $v_0 = (2kT_0/m)^{0.5}$ , reference dynamic viscosity  $\mu_0$ , reference length  $L$ , time  $t_0 = L/v_0$ . Thus, we have the following dimensionless variables:

$$\tilde{\mathbf{x}} = \mathbf{x}/L, \quad \tilde{\boldsymbol{\xi}} = \boldsymbol{\xi}/v_0, \quad \tilde{t} = t/t_0 \quad (31)$$

$$\tilde{\rho} = \rho/mn_0, \quad \tilde{T} = T/T_0, \quad \tilde{\mathbf{V}} = \mathbf{V}/v_0, \quad \tilde{p} = p/p_0, \quad \tilde{\mathbf{q}} = \mathbf{q}/p_0v_0 \quad (32)$$

$$\tilde{\mu} = \mu/\mu_0, \quad \tilde{f} = f v_0^3 / \rho_0 \quad (33)$$

Further, for simplicity the tildes above dimensionless variables are omitted.

In kinetic gas theory the one of the most important parameters is the Knudsen number  $Kn$  characterized the rarefaction level of the gas flow and defined as the ration between characteristic length of the flow to mean free path  $\lambda$ . Here, the reference Knudsen number  $Kn$  is

the ratio between the reference length  $L$  and the mean free path  $\lambda_0$  at reference conditions. Choosing the hard-sphere molecular model, for the present study, the mean free path is defined as:

$$\lambda_0 = \frac{16\mu_0}{5\rho_0} \sqrt{\frac{m}{2\pi kT_0}}. \quad (34)$$

Another rarefaction parameter  $\delta$ , characterized rarefaction of the gas flow, can be introduced as:

$$\delta = \frac{p_0 H}{\mu_0 v_0} = \frac{8}{5Kn \sqrt{\pi}}, \quad (35)$$

Using dimensionless variables, the transport kinetic equation (1) with S-model collision integral and initial condition (2) can be rewritten as following [20, 21]:

$$\frac{\partial f}{\partial t} + \xi \frac{\partial f}{\partial \mathbf{x}} = \delta \rho \sqrt{T} (f^S - f), \quad (36)$$

$$f(0, \mathbf{x}, \xi) = M(1, \mathbf{c}_i, 1) \quad (37)$$

$$f^S(\rho, \mathbf{c}, T) = M(\rho, \mathbf{c}, T) \left( 1 + \frac{4}{5} (1 - \text{Pr}) \frac{2\mathbf{q}\mathbf{c}}{\rho T^2} \left( \frac{\mathbf{c}^2}{T} - \frac{5}{2} \right) \right), \quad (38)$$

$$M(\rho, \mathbf{c}, T) = \frac{\rho}{(\pi T)^{3/2}} \exp\left(-\frac{\mathbf{c}^2}{T}\right), \quad (39)$$

Moreover, for monatomic gas the dimensionless viscosity coefficient, for hard-sphere molecular model, is  $\mu = T^{0.5}$  and thermal conductivity is  $\kappa = (15/4) \mu$ .

The dimensionless macroscopic (bulk) distributions of number density, velocity vector, temperature and heat flux, respectively, are computed using the following formulas:

$$\rho = \int f d\xi, \quad \rho(u, v)^T = \int (\xi_x, \xi_y)^T f d\xi, \quad \frac{3}{2} \rho T = \int \mathbf{c}^2 f d\xi, \quad (q_x, q_y)^T = \frac{1}{2} \int (c_x, c_y)^T \mathbf{c}^2 f d\xi \quad (40)$$

Replacing the Boltzmann collision integral  $J_B(f, f)$  by the S-model and taking into account two-dimensionality of the flow (problems considered in the present work are two-dimensional)

we can eliminate  $z$  component of the molecular velocity by the projection procedure, thus, essentially decrease the CPU time and the memory requirement in comparison with the solution of the full Boltzmann equation in which the velocity space is always three-dimensional. This is performed by introducing the new reduced distribution functions:

$$\varphi(t, \mathbf{x}, \xi_x, \xi_y) = \int_{-\infty}^{\infty} f(t, \mathbf{x}, \xi) d\xi_z \quad (41)$$

$$\psi(t, \mathbf{x}, \xi_x, \xi_y) = \int_{-\infty}^{\infty} f(t, \mathbf{x}, \xi) \xi_z^2 d\xi_z \quad (42)$$

Multiplying equation (36) by 1 and  $\xi_z$  and integrating with respect to  $d\xi_z$  we obtain the following coupled set of integro-differential equations:

$$\frac{\partial \varphi}{\partial t} + \xi \frac{\partial \varphi}{\partial \mathbf{x}} = \delta \sigma(\rho, T)(\Phi^s - f) \quad (43)$$

$$\frac{\partial \psi}{\partial t} + \xi \frac{\partial \psi}{\partial \mathbf{x}} = \delta \sigma(\rho, T)(\Psi^s - f) \quad (44)$$

where the reduced Shakhov and Maxwell distribution functions are read as:

$$\Phi^s = \Phi_M \left( 1 + \frac{4}{5} (1 - \text{Pr})(\Sigma_x c_x + \Sigma_y c_y)(\mathbf{c}^2 - 2) \right) \quad (45)$$

$$\Psi^s = \frac{1}{2} T \Phi_M \left( 1 + \frac{4}{5} (1 - \text{Pr})(\Sigma_x c_x + \Sigma_y c_y)(\mathbf{c}^2 - 1) \right) \quad (46)$$

$$\Phi_M = \frac{\rho}{\pi T} \exp \left[ -\frac{\mathbf{c}^2}{T} \right], \quad \Psi_M = \frac{T}{2} \Phi_M, \quad \Sigma_i = \frac{2q_i}{\rho T^{3/2}} \quad (47)$$

The Maxwell diffuse reflecting boundary condition with the full accommodation at walls is applied, i.e. in the kinetic subdomain  $\Omega_K$ . Incident molecules are assumed to be absorbed by the wall and re-emitted with the wall temperature  $T_w$  and with a random velocity, according to the Maxwell distribution function centred on the velocity of the wall  $\mathbf{V}_w$ :

$$f|_w(t, \mathbf{x}, \xi) = \omega(\mathbf{x}) M(1, \mathbf{c}_w, T_w), \xi \cdot \boldsymbol{\eta}(\mathbf{x}) > 0 \quad (48)$$

where  $\eta(\mathbf{x})$  is the vector normal to the wall (direct toward the gas), and  $\omega(\mathbf{x})$  is determined so as to avoid a mass flux across the wall [18]:

$$\omega(\mathbf{x}) = - \frac{\int_{\xi \cdot \eta(\mathbf{x}) < 0} \xi \cdot \eta(\mathbf{x}) f(t, \mathbf{x}, \xi) d\xi}{\int_{\xi \cdot \eta(\mathbf{x}) > 0} \xi \cdot \eta(\mathbf{x}) M(1, \mathbf{V}_w, T_w) d\xi}, \quad (49)$$

At inlet/outlet boundary conditions the Maxwell velocity distribution function is imposed, as well, for incoming in the computational domain particles. The density, temperature and bulk velocity, defining Maxwell distribution function, are specified by considered problem. At the symmetry line the specular boundary condition is imposed.

### 3.1.2. Numerical scheme

The system of kinetic equations (43) and (44) is solved by using the discrete velocity method (DVM). The obtained system of two equations are discretized on a 2D grid in velocity space  $\{\xi_{\Gamma}\} = (\xi_x^{\alpha} = -v_{max} + \alpha\Delta\xi_x, \quad \xi_y^{\beta} = -v_{max} + \beta\Delta\xi_y), \quad \alpha = 1, \dots, \alpha_{max}, \quad \beta = 1, \dots, \beta_{max},$  where  $\Gamma = (\alpha, \beta) \leq N_{\xi} = \alpha_{max} \times \beta_{max}$  defines velocity grid point indices. In general, the velocity grid is the Cartesian uniform one, but there are other opportunities to discretize velocity space. For example, if velocity space nodes are located at Gaussian abscissas, Gaussian integration may be performed via proper Gaussian weight function.

Denoting  $\varphi_{\Gamma}^n$  and  $\psi_{\Gamma}^n$  as the approximations of  $\varphi(t^n, \xi_{\Gamma}, \mathbf{x})$  and  $\psi(t^n, \xi_{\Gamma}, \mathbf{x})$ , respectively, the obtained set of equations for  $\varphi_{\Gamma}^n$  and  $\psi_{\Gamma}^n$  is numerically solved explicitly/implicitly in time [28, 29]:

$$\frac{\varphi_{\Gamma}^{n+1} - \varphi_{\Gamma}^n}{\Delta t} + \xi_{\Gamma} \frac{\partial \varphi_{\Gamma}^n}{\partial \mathbf{x}} = \delta \sigma^{n+1} (\Phi_S^{n+1} - \varphi_{\Gamma}^{n+1}) \quad (50)$$

$$\frac{\psi_{\Gamma}^{n+1} - \psi_{\Gamma}^n}{\Delta t} + \xi \frac{\partial \psi_{\Gamma}^n}{\partial \mathbf{x}} = \delta \sigma^{n+1} (\Psi_S^{n+1} - \psi_{\Gamma}^{n+1}) \quad (51)$$

or

$$\Phi_{\Gamma}^{n+1} = \frac{1}{1 + \Delta t \delta \sigma^{n+1}} \left( \Phi_{\Gamma}^n - \Delta t \xi_{\Gamma} \frac{\partial \Phi_{\Gamma}^n}{\partial \mathbf{x}} \right) + \frac{\Delta t \delta \sigma^{n+1}}{1 + \Delta t \delta \sigma^{n+1}} \Phi_S^{n+1} \quad (52)$$

$$\Psi_{\Gamma}^{n+1} = \frac{1}{1 + \Delta t \delta \sigma^{n+1}} \left( \Psi_{\Gamma}^n - \Delta t \xi_{\Gamma} \frac{\partial \Psi_{\Gamma}^n}{\partial \mathbf{x}} \right) + \frac{\Delta t \delta \sigma^{n+1}}{1 + \Delta t \delta \sigma^{n+1}} \Psi_S^{n+1} \quad (53)$$

where  $\sigma^{n+1} = \sigma(\rho^{n+1}, T^{n+1})$ . In spite of the collision part is written at time moment  $t^{n+1}$  macroscopic quantities: density  $\rho^{n+1}$ , bulk velocity  $\mathbf{V}^{n+1}$  and temperature  $T^{n+1}$  can be obtained explicitly:

$$(\rho, \rho \mathbf{V}, \frac{3}{2} \rho T)^{n+1} = \int_{R^3} \mathbf{s}^T(\xi) \left( (\varphi, \psi)^n - \Delta t \xi \frac{\partial (\varphi, \psi)^n}{\partial \mathbf{x}} \right) d\xi \quad (54)$$

where  $\mathbf{s}(\xi) = (1, \xi, \xi^2/2)$  is the collision vector. Thus, allow us to compute reduced Shakhov functions  $\Phi_S^{n+1}$ ,  $\Psi_S^{n+1}$  and  $\sigma^{n+1}$  [29].

The transport term in equations (52) and (53) is treated explicitly and approximated by a standard finite volume TVD scheme. Introducing in the physical space a 2D, uniform Cartesian grid defined by nodes  $(x_i, y_j) = (i\Delta x, j\Delta y)$ , for  $i = 1, \dots, i_{\max}$  and  $j = 1, \dots, j_{\max}$  and  $N_c = i_{\max} \times j_{\max}$  and cells  $(x_{i-1/2}, x_{i+1/2}) \times (y_{j-1/2}, y_{j+1/2})$  centred around each node. Assuming  $\varphi_{\Gamma, i, j}^n$  and  $\psi_{\Gamma, i, j}^n$  are the approximations of  $\varphi(t^n, \xi_{\Gamma}, x_i, y_j)$  and  $\psi(t^n, \xi_{\Gamma}, x_i, y_j)$  and distribution function values are known at time  $t^n = n\Delta t$  the numerical solution of the transport step can be written as:

$$\Phi_{\Gamma, i, j}^{n+1} = \Phi_{\Gamma, i, j}^n - \frac{\Delta t}{\Delta x} \left( F_{i+1/2, j}(\Phi_{\Gamma}^n) - F_{i-1/2, j}(\Phi_{\Gamma}^n) \right) - \frac{\Delta t}{\Delta y} \left( F_{i, j+1/2}(\Phi_{\Gamma}^n) - F_{i, j-1/2}(\Phi_{\Gamma}^n) \right), \quad (55)$$

The similar solution can be written for the second reduction function  $\psi_{\Gamma, i, j}^n$ .

Numerical fluxes  $F_{i+1/2, j}(\Phi_{\Gamma}^n)$  and  $F_{i, j+1/2}(\Phi_{\Gamma}^n)$  are defined as following:

$$F_{i+1/2,j}(\varphi_{\Gamma}^n) = \frac{1}{2} \left( \xi_x^\alpha (\varphi_{\Gamma,i+1,j}^n + \varphi_{\Gamma,i,j}^n) - |\xi_x^\alpha| (\Delta\varphi_{\Gamma,i+1/2,j}^n - \Theta_{\Gamma,i+1/2,j}^n) \right), \quad (56)$$

$$F_{i,j+1/2}(\varphi_{\Gamma}^n) = \frac{1}{2} \left( \xi_y^\beta (\varphi_{\Gamma,i,j+1}^n + \varphi_{\Gamma,i,j}^n) - |\xi_y^\beta| (\Delta\varphi_{\Gamma,i,j+1/2}^n - \Theta_{\Gamma,i,j+1/2}^n) \right), \quad (57)$$

$$\Delta\varphi_{\Gamma,i+1/2,j}^n = \varphi_{\Gamma,i+1,j}^n - \varphi_{\Gamma,i,j}^n, \quad \Delta\varphi_{\Gamma,i,j+1/2}^n = \varphi_{\Gamma,i,j+1}^n - \varphi_{\Gamma,i,j}^n. \quad (58)$$

$\Theta_{\Gamma,i+1/2,j}^n$  is the flux limiter function provided a second order of the scheme. For the most part of computations the minmod limiter function is used [30, 31]:

$$\Theta_{\Gamma,i+1/2,j}^n = \min \text{ mod} \left( \Delta\varphi_{\Gamma,i-1/2,j}^n, \Delta\varphi_{\Gamma,i+1/2,j}^n, \Delta\varphi_{\Gamma,i+3/2,j}^n \right) \quad (59)$$

where the minmod function can be computed as:

$$\min \text{ mod} (a_1, a_2, a_3) = \begin{cases} \min_i |a_i|, & \text{if } \text{sign}(a_1) = \text{sign}(a_2) = \text{sign}(a_3), \\ 0, & \text{otherwise} \end{cases} \quad (60)$$

The high order scheme, the third order MUSCL scheme with the Van Albada limiter is used for computations as well [32, 33]. The numerical flux  $F_{i+1/2,j}(\varphi_{\Gamma}^n)$  (formula for  $F_{i,j+1/2}(\varphi_{\Gamma}^n)$  flux is similar and not presented here) can be rewritten in different form:

$$F_{i+1/2,j}(\varphi_{\Gamma}^n) = \begin{cases} (\varphi_L)_{\Gamma,i+1/2,j}, & \xi_x^\alpha \geq 0 \\ (\varphi_R)_{\Gamma,i+1/2,j}, & \xi_x^\alpha \leq 0 \end{cases} \quad (61)$$

where  $\varphi_L$  and  $\varphi_R$  are the distribution functions on the left and right side of the interface  $(i + 1/2, j)$ . They are determined by the third order MUSCL with the smooth limiter to extrapolate the value of  $\varphi_{\Gamma,i,j}^n$  on the two sides of an interface:

$$\begin{cases} (\varphi_L)_{\Gamma,i+1/2,j} = \varphi_{\Gamma,i,j} + \left[ \frac{s}{4} ((1-ks)\Delta_- + (1+ks)\Delta_+) \right]_i, \\ (\varphi_R)_{\Gamma,i+1/2,j} = \varphi_{\Gamma,i+1,j} - \left[ \frac{s}{4} ((1-ks)\Delta_+ + (1+ks)\Delta_-) \right]_{i+1}, \end{cases} \quad (62)$$

where  $k = 1/3$  and  $s$  is the Van Albada limiter [34]:

$$s = \frac{2\Delta_+\Delta_- + \theta^2}{\Delta_+^2 + \Delta_-^2 + \theta}. \quad (63)$$

Here  $\theta$  is a small number ( $\theta = 10^{-6}$ ) preventing division by zero in the region of null gradient and

$$(\Delta_+)_i = \varphi_{\Gamma,i+1,j} - \varphi_{\Gamma,i,j}, \quad (\Delta_-)_i = \varphi_{\Gamma,i,j} - \varphi_{\Gamma,i-1,j} \quad (64)$$

The transport time step follows the condition:

$$\Delta t = CFL / \max(v_{\max} / \Delta x + v_{\max} / \Delta y), \quad (65)$$

where  $CFL$  is the Courant - Friedrichs - Lewy number,  $v_{\max}$  is an upper boundary of the velocity space and  $\Delta x$  and  $\Delta y$  are the mesh sizes in the  $x$  and  $y$  directions, respectively.

Complex geometries may require a more general nonuniform structured mesh, which should be treated with a curvilinear mesh. To approximate space derivatives on 2D curvilinear grid the following curvilinear coordinates  $\zeta(x, y)$  and  $\eta(x, y)$  are used [17]. Thus, the transport equation for 2D case can be rewritten as:

$$\frac{1}{J} \frac{\partial \varphi_{\Gamma}}{\partial t} + \partial(\xi_{\Gamma} \bullet \frac{\nabla \zeta}{J} \varphi_{\Gamma})_{\zeta} + \partial(\xi_{\Gamma} \bullet \frac{\nabla \eta}{J} \varphi_{\Gamma})_{\eta} = 0, \quad (66)$$

where  $\nabla \zeta = (\partial \zeta_x, \partial \zeta_y)$ ,  $\nabla \eta = (\partial \eta_x, \partial \eta_y)$  and  $J = \partial \zeta_x \partial \eta_y - \partial \zeta_y \partial \eta_x$  is the determinant of the Jacobian matrices of the transformation. If we define a uniform grid ( $\zeta = i\Delta \zeta$ ,  $\eta_j = j\Delta \eta$ ), then a scheme similar to (55) can be used:

$$\varphi_{\Gamma,i,j}^{n+1} = \varphi_{\Gamma,i,j}^n - \frac{\Delta t}{\Delta \zeta} (F_{i+1/2,j}(\varphi_{\Gamma}^n) - F_{i-1/2,j}(\varphi_{\Gamma}^n)) J_{i,j} - \frac{\Delta t}{\Delta \eta} (F_{i,j+1/2}(\varphi_{\Gamma}^n) - F_{i,j-1/2}(\varphi_{\Gamma}^n)) J_{i,j} \quad (67)$$

The numerical fluxes  $F_{i+1/2,j}(\varphi_{\Gamma}^n)$  and  $F_{i,j+1/2}(\varphi_{\Gamma}^n)$  are defined as following:

$$F_{i+1/2,j}(\varphi_{\Gamma}^n) = \frac{1}{2} \left( \xi_{\mathbf{r}} \bullet \left( \frac{\nabla \zeta}{J} \right)_{i+1/2,j} (\varphi_{\Gamma,i+1,j}^n + \varphi_{\Gamma,i,j}^n) - \left| \xi_{\mathbf{r}} \bullet \left( \frac{\nabla \zeta}{J} \right)_{i+1/2,j} \right| (\Delta \varphi_{\Gamma,i+1/2,j}^n - \Theta_{\Gamma,i+1/2,j}^n) \right), \quad (68)$$

$$F_{i,j+1/2}(\varphi_{\Gamma}^n) = \frac{1}{2} \left( \xi_{\mathbf{r}} \cdot \left( \frac{\nabla \eta}{J} \right)_{i,j+1/2} (\varphi_{\Gamma,i,j+1}^n + \varphi_{\Gamma,i,j}^n) - \left| \xi_{\mathbf{r}} \cdot \left( \frac{\nabla \eta}{J} \right)_{i,j+1/2} \right| (\Delta \varphi_{\Gamma,i,j+1/2}^n - \Theta_{\Gamma,i,j+1/2}^n) \right), \quad (69)$$

Geometric coefficients  $(\nabla \zeta/J)_{i\pm 1/2,j}$ ,  $(\nabla \eta/J)_{i,j\pm 1/2}$  and  $J_{i,j}$  are standard approximations used in order to preserve the free stream [17]. This scheme has the same properties as scheme (55) (i.e., positivity, conservation of moments, and dissipation of entropy), provided that a *CFL* condition similar to formula (65) is satisfied.

## 3.2. Navier-Stokes solver

### 3.2.1. Governing equations and boundary conditions

For the continuum regime, the standard approach used to describe the gas flow is based on continuum Navier-Stokes equations. These equations describe the flow in terms of mere average flow velocity, gas density and temperature, thus are much more efficient than kinetic equations, but much less accurate in critical rarefied areas. The inaccuracy of NS equations in the boundary layer can be partially overcome by introducing slip boundary and temperature jump conditions on the solid surface. However, as indicated in the literature, slip conditions are valid only for the local Knudsen number  $Kn \leq 0.1$ , and any attempts to increase their range, resorting to higher order slip boundary conditions, is not trivial and highly geometrical dependent.

The governing equations of the flow are viscous, compressible two-dimensional NS equations which can be written in terms of conservative variables as:

$$\frac{\partial \mathbf{U}}{\partial t} + \frac{\partial \mathbf{F}(\mathbf{U})}{\partial \mathbf{x}} = 0, \quad (70)$$

$$\mathbf{U} = (\rho, \rho \mathbf{V}, \rho e_{tot}), \quad e_{tot} = e + \mathbf{V}^2 / 2 \quad (71)$$

where  $e_{tot}$  is the total energy per unit mass.

The flux vector  $\mathbf{F}(\mathbf{U})$  may be decomposed into the convective (inviscid) and diffusive (viscous) components as following:

$$\mathbf{F} = \mathbf{F}_{inv} - \mathbf{F}_{vis} \quad (72)$$

$$\mathbf{F}_{inv} = (\rho \mathbf{V}, \rho \mathbf{V} \mathbf{V} + p \mathbf{I}, \mathbf{V}(\rho e_{tot} + p))^T \quad (73)$$

$$\mathbf{F}_{vis} = (0, \boldsymbol{\tau}, \boldsymbol{\tau} \cdot \mathbf{V} + \mathbf{q})^T \quad (74)$$

As in any compressible flow solver, viscous dissipation term  $\boldsymbol{\tau} \cdot \mathbf{V}$  is included in the energy equation. Pressure  $p$  and total energy per unit mass  $e_{tot}$  are linked by the equation of state for ideal gas:

$$p = \rho(\gamma-1) \left( e_{tot} - \frac{\mathbf{V}^2}{2} \right) \quad (75)$$

The inlet/outlet boundary conditions are standard and specify the inlet total temperature  $T_0$ , total pressure  $p_0$  and flow direction, and the static pressure  $p_e$  at the outlet. The compressibility effect of the gas is monitored via the local value of Mach number  $Ma$  and the isentropic exit Mach number  $Ma_{is}$  (i.e.,  $Ma$  that would arise from an isentropic flow with the same pressure ratio as the real one):

$$\frac{p_0}{p_e} = \left( 1 + \frac{\gamma-1}{2} Ma_{is}^2 \right)^{\gamma/(\gamma-1)} \quad (76)$$

$$\frac{T_0}{T_e} = \left( 1 + \frac{\gamma-1}{2} Ma_{is}^2 \right) \quad (77)$$

$$\rho_0 = p_0 / RT_0 \quad (78)$$

At solid wall, i.e. in continuum domain  $\Omega_{NS}$ , the Maxwell first order slip boundary condition is imposed [10, 11]:

$$u_{gas} - u_w = s_p Kn \left( \frac{\partial u_{\zeta(\mathbf{x})}}{\partial \eta(\mathbf{x})} + \frac{\partial u_{\eta(\mathbf{x})}}{\partial \zeta(\mathbf{x})} \right) \quad (79)$$

$$s_p = \frac{\sqrt{\pi}}{2} \frac{2 - \sigma_v}{\sigma_v} (1 + 0.1366 \sigma_v) \quad (80)$$

where  $\eta(\mathbf{x})$  and  $\zeta(\mathbf{x})$  are unit vectors normal and tangential to the solid wall, respectively. In computations  $s_p$  is around one (i.e., the fraction  $\sigma_v$  of incident particles scattered diffusely is set equal to one). The additional derivative along the tangential direction is essential in capturing even the qualitative behaviour of the slip flow along curved walls.

A Dirichlet temperature boundary condition is imposed at the wall. The wall temperature is fixed at the inlet total temperature value to minimize the effect of viscous dissipation. In the energy equation, the Smoluchowski temperature jump is used:

$$T_{gas} - T_w = s_T Kn \frac{\partial T}{\partial \eta(\mathbf{x})} \quad (81)$$

$$s_T = \frac{2 - \sigma_T}{\sigma_T} \frac{2\gamma}{\gamma + 1} \frac{1}{Pr} \quad (82)$$

where  $s_T$  is the temperature jump coefficient. Since the flow is considered isothermal the temperature accommodation coefficient  $\sigma_T$  equals to one. At the symmetry line the specular boundary condition is imposed.

### 3.2.2. Numerical scheme

Navier-Stokes equations are solved by employing a finite difference and finite volume method. The numerical method is described in detail in [35] and has formal second order accuracy in space and time. Thus, here it is only briefly outlined.

Adopting a curvilinear, structured mesh we may define a computational cell of volume  $\Lambda_{ij}$  with faces  $A_k$ ,  $k = 1, \dots, 4$  around each node. At each of these computational cells the flux balance offers:

$$\Lambda_{ij} \frac{\partial \mathbf{U}_{ij}}{\partial t} = \sum_{k=1}^4 \mathbf{F}(\mathbf{U}) \cdot A_k \eta(\mathbf{x})_k \quad (83)$$

Fluxes are defined via neighboring value averaging, and an artificial dissipation term  $d$  is added to prevent checker boarding and numerical instabilities. Thus, considering a face located at  $i+1/2$  we get:

$$\mathbf{F}^{inv}(\mathbf{U})_{i+1/2} = \frac{\mathbf{F}^{inv}(\mathbf{U})_i + \mathbf{F}^{inv}(\mathbf{U})_{i+1}}{2} + d_{i+1/2} \quad (84)$$

Artificial dissipation term  $d$  are given by a blend of second and fourth order differences, scaled by the maximum eigenvalue of jacobian matrix of vectors  $\mathbf{F}_{inv}$ , as suggested in (Pulliam [36]). Second order terms are switched on near discontinuities, as in Pulliam [36]. Viscous flux vectors are evaluated with second order finite differences at  $i+1/2$ . The solution is advanced in time via Crank Nicolson integration scheme, and the resulting matrices are decomposed via the spatially factored ADI scheme originally proposed by Beam and Warming (see Hirsh [37]). Following such scheme, two series of block tridiagonal algebraic systems are solved at each time step, rather than the original sparse matrix arising from the flux discretization.

### 3.3. MPI parallelization

The hybrid code is parallelized in order to improve its efficiency using MPI message passing protocol. In a message passing paradigm, several separate processes used to complete the overall computation. Since two different solvers are coupled in the hybrid solver, different algorithms are used for S-model and NS parallelization.

Nowadays, there are a lot of works devoted parallelization of kinetic equations, see e.g. [38, 39], here the following parallel strategy is applied.

The solution of kinetic equations system (52), (53) is local in the velocity node  $\Gamma = (\alpha, \beta)$ , and therefore completely parallelizable in the velocity space. For parallelization purpose distribution functions arrays for  $\varphi_{\Gamma,ij}^n$  and  $\psi_{\Gamma,ij}^n$  are stored first by space indexes  $i,j$  and then by

velocity ones  $\Gamma = (\alpha, \beta)$ , as following:  $\varphi_{\Gamma,ij}^n = (\varphi_{,ij}^n)_{\Gamma}$  and  $\psi_{\Gamma,ij}^n = (\psi_{,ij}^n)_{\Gamma}$ . At initialization stage, these huge distribution function arrays of size  $N_c \times N_{\xi}$  are subdivide to smaller ones of the size  $N_c \times N_{\xi} / N_p$  ( $N_p$  is the total number of processes chosen by user). Thus, at each time step a process solves only smaller part of system (52), (53).

In order to avoid the transfer of large array of distribution function data between processes, macro values are partially (since each processor has data of size  $(N_c \times N_{\xi} / N_p)$ , i.e. only for part of the velocity space) computed by each process using formulas (40). The real macroparameters are finally computed by summation of data coming from all processors. This is carried out using the collective command `MPI_Allreduce` [40].

The solution of Navier-Stokes equation can be parallelized as well. At each time step series of block tridiagonal algebraic systems are solved sequentially, thus the solution of each system may be considered as independent on one of the physical coordinate, e.g.,  $x$  one. This allows us naturally parallelize the code using MPI. In this scheme,  $N_p$  concurrent processes are created, having the same copy of the data involved in the calculation.  $i$ -process solves a part of system of NS equations, i.e., for space points from  $x_i$  to  $x_{i+i_{\max}/N_p}$  ( $i_{\max}$  is the maximum number of grid points in streamwise direction  $x$ ). Since there is no shared data, in order to solve the following system (for  $y$  coordinate) each process needs data held by other ones, therefore, the data must be exchanged between processes, in order to each process has a full intermediate solution. The unknown parts of data, (result of the first system solution), from other processes are gathered by each process using the collective command `MPI_Allgather` [40].

The software code was written in C++ and Fortran with the use of MPI. Computations were carried out on Multi Core system consisting of 2 quad core processors, Intel(R) Xeon(R) E5520 CPU, 2.27 (2.93) GHz, 8 MB Cache, for a maximum of 8 concurrent cores.

## 4. Validation: gas flow through the slit

### 4.1. Introduction

The gas flow through a slit is a relatively simple flow configuration representative of several real engineering applications, encountered, e.g., in vacuum equipment, micro/nano devices, spacecraft design, and metrology of gas flow. In addition, the flow through the slit is a popular numerical benchmark test for the validation of numerical methods. Despite its geometrical simplicity, in fact, the numerical study of the pressure-driven gas flow through the slit is not a trivial task due to possible local transition from continuum to rarefied regimes in the flow near the slit, requiring the use of hybrid simulation methods. Since the pressure drop ratio may vary from 1 to thousands (flow into vacuum), the molecular mean free path changes correspondingly from tens of nanometers to millimetres.

In the open literature kinetic approaches, allowing to describe all flow regimes from continuum to free-molecular, are commonly adopted to study the slit flow. In particular, numerical solutions of linearized BGK and S model kinetic equations for the slit problem have been reported in [41, 42]. Nonlinear BGK and S-model kinetic equations were implemented for the simulation of the flow through the slit into vacuum in [43] and at arbitrary pressure ratios in [44, 45], ranging from free-molecular to hydrodynamic regime. The rarefied gas flow through a slit was studied on the basis of the direct simulation Monte Carlo (DSMC) method at an arbitrary pressure ratio including flow to the vacuum over the whole range of gas rarefaction in [46]. Moreover, in [43] it was stated that nonlinear BGK and S-models provide a solution close to DSMC results, at a lower computational cost and avoiding the statistical scattering typical of DSMC solutions in the case of small flow velocities.

The direct numerical solution of the Boltzmann equation was compared with BGK results in [44] and with S-model ones in [45] for the gas rarefaction range from the free-molecular to the

hydrodynamic regime and for the reservoir pressure ratios leading to either the subsonic or supersonic outflow. It was shown that nonlinear BGK and S-model equations provide the same value of the mass flow rate as the Boltzmann equation within the relative difference of the order of 1%.

In [4] a hybrid CFD/DSMC solver was applied to predict gas flow and pressure in axisymmetric micro-thruster nozzles for the throat Knudsen number varying from 0.008 to 0.125. It was shown that CFD simulations, even when thermal and velocity slip at the walls were accounted for boundary conditions, could not properly predict gas velocities and pressures in micro-nozzles. The high efficiency of solver was demonstrated: simulations can be performed in 5–25% of the CPU time required for a full DSMC simulation whereas predicted outflow macro parameters (pressures and velocities) differed less than 1–2%. The hybrid Euler/DSMC solver has been applied for unsteady evolution of a jet from a slit subjected to a pressure differential in [5]. The approach allowed one to resolve complicated transient flow structures. In [9] an adaptive hybrid kinetic–fluid solver was implemented for pressure-driven flow through a slit for a rarefaction level ranging from transition to slip regime and pressure ratios 0.9 and 0.99.

The accuracy and computational efficiency of the proposed approach are assessed via comparison with both Navier-Stokes and pure kinetic solutions for the test case problem: gas flow through the slit at pressure ratio of 0.1, 0.5 and 0.9, plus flow into vacuum and Knudsen number from slip to transitional regime. The size of continuum and kinetic domains is here dynamically updated during the transient depending on the current  $Kn_{GL}$ . The solution is advanced in time simultaneously in both kinetic and continuum domains: the coupling is achieved by matching half fluxes at the interface of kinetic and NS domains, thus taking care of the conservation of momentum, energy and mass through the interface.

## 4.2. Statement of the problem

The planar monoatomic gas flow through a slit of height  $H$  cut in an infinitely thin partition at the plane  $x = 0$  separating two containers (see Fig. 2) is considered. The gas far from the slit is in equilibrium at pressures  $p_0$  in the inlet plenum and  $p_e$  in the outlet one, with  $p_0 > p_e$ , and the same temperature  $T_0$ . The slit is considered as infinite in the  $z$  direction. Since the main aim of the work is the assessment of the coupling procedure, only a monatomic pure gas consisting of hard sphere molecules is considered. Any extension to mixtures or polyatomic gas, although in principle possible, is thus outside the scope of the work and not yet considered or discussed here.

Two large areas of radius  $R$  before and after the slit are included in the computation, simulating upstream and downstream reservoirs. Thus, the computational domain has the shape of a circle of radius  $R$  surrounding a slit of size  $H$ . Due to the symmetry of the problem about  $y = 0$  only a half of the circle and a slit ( $-H/2 \leq y \leq 0$ ), shown in Fig. 2, will be considered. The bold line  $I_c$  in Fig. 2 is the moving interface between kinetic and NS sub-domains, and its position is updated during the computation.

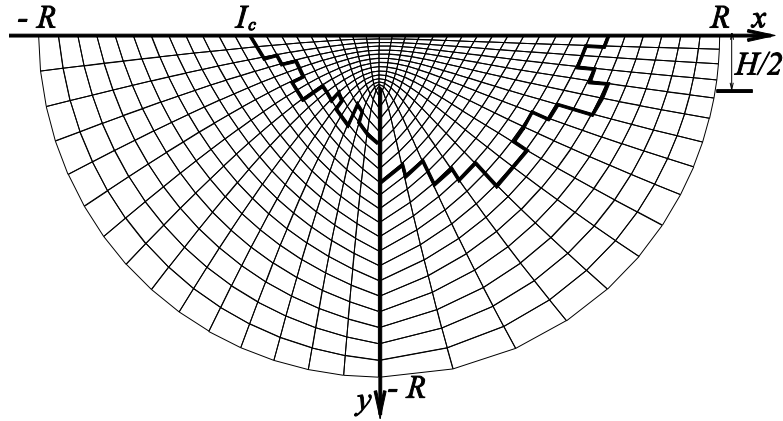


**Fig. 2.** Computational domain sketch.

The difference between upstream  $p_0$  and downstream  $p_e$  reservoirs pressures induces mass flow through the slit. The static inlet pressure  $p_i$  is the result of computation, although, due to the low inlet velocity, it almost coincides with total inlet pressure  $p_0$ . A global characteristic of the flow, namely dimensionless mass flow rate  $W$ , is introduced as:

$$W = \frac{\dot{m}}{\dot{m}_{fm}}, \quad \dot{m}_{fm} = \frac{Hp_0}{\sqrt{\pi}v_0}, \quad (85)$$

where  $\dot{m}_{fm}$  is the analytically deduced mass flow rate in the limit of free molecular regime and the mass flow rate through the slit is computed at the slit position  $x = 0$  as:

$$\dot{m} = 2 \int_{-H/2}^0 \rho(x, y) u(x, y) dy \quad . \quad (86)$$

The problem is recast in terms of non-dimensional variables using inlet reservoir equilibrium values as reference ones: e.g., density  $\rho_0$ , temperature  $T_0$ , most probable velocity  $v_0 = (2kT_0/m)^{0.5}$  ( $m$  is the particle mass), reference dynamic viscosity  $\mu_0$ , height of the slit  $H$ .

### 4.3. Parameters of modelling

Computations have been carried out at pressure ratios  $p_e/p_0 = 0.1, 0.5, 0.9$  plus flow to the vacuum ( $p_e/p_0 = 0$ ), and a rarefaction  $\delta$  from 100 (slip regime) to 1 (transition regime). The computational domain shown in Fig. 2 represents half of circle of radius  $R = 40H$  [10, 44]. The use of circular sectors as inlet and outlet reservoirs, rather than the more common square shape, allows for larger size with a relatively smaller number of grid points, while preserving a strong refinement near the slit.

A non uniform structured curvilinear grid of 320 nodes in the streamwise direction (dimensionless minimum grid spacing near the slit 0.017) and 40 nodes in the transverse direction is used for moderate and large pressure ratios  $p_e/p_0 = 0.5, 0.9$ , while a finer grid with  $400 \times 60$  nodes was used for lower ratios  $p_e/p_0 = 0.1$  and 0.

The size of uniform two-dimensional velocity grid should be selected large enough to capture all of important features of the problem: thus, the velocity space boundary satisfies the following condition  $v_{\max} \geq \max(|u|, |v|) + 3.5T_{\max}^{0.5}$ . For most of computations the number of grid points for each velocity component is 24 and velocity space is bounded by  $v_{\max} \approx 5.2$ . In case of

the high gradient flow, i.e.  $p_e/p_0 = 0.1$  and 0, the number of points is increased from 48 to 64 and  $v_{\max}$  from 7.6 to 12, respectively.

The grid independence test has been done comparing a mass flow rate value computed using a coarse grid with  $240 \times 40$  nodes. The mass flow difference between fine and coarse meshes is less than 1%. The optimal number of grid points in the velocity space was chosen checking that doubling velocity points produces a change in the mass flow rate lower than 1-1.5%.

The time step is unique for both solvers and it should satisfy the stricter stability (or accuracy) constraint  $\Delta t = \min(\Delta t_K, \Delta t_{NS})$ . The kinetic time step should be limited by the condition (65) with  $CFL = 0.4$ , while  $\Delta t_{NS}$  is arbitrary.

The solution is considered to be converged when the following criterion is fulfilled:

$$\|\mathbf{U}^{n+1} - \mathbf{U}^n\|_{L_2} < \Delta \quad (87)$$

where  $\mathbf{U}$  is the vector of macroscopic conservative variables, the  $L_2$  norm is used,  $\Delta = 10^{-7}$ .

**Table 1.** Dimensionless mass flow rate at  $p_e/p_0 = 0.5$  and  $\delta = 1$ : effect of threshold parameter  $\Xi$ .

$\Xi$	$W_h$	$W_{BGK}$
0.05	0.653	
0.1	0.653	
0.5	0.643	0.653
1	0.624	
2	0.597	

As was mentioned above the choice of threshold value  $\Xi$  decomposing computational domain into kinetic and continuum sub-domains affects the computed flow field, e.g., in [6, 7]  $\Xi = 0.05$  was suggested. In Table 1 dimensionless mass flow rates  $W_h$  obtained by hybrid solver for different switching criteria  $\Xi$  at fixed  $\delta = 1$  and  $p_e/p_0 = 0.5$  are shown. As can be seen, for large  $\Xi > 0.1$ , the mass flow rate is quite different from the kinetic value,  $W_{BGK} = 0.653$ . The mass flow rate  $W_h$  converges to the correct value when  $\Xi$  is less or equal to 0.1. However,

following [6, 7] for further slit computations we used threshold value  $\Xi = 0.05$ , in order to be on the safe side, since high gradient flow (including flow into vacuum) is considered, but even the use of the higher value  $\Xi = 0.1$  would produce a correct solution.

#### 4.4. Results and discussion

**Table 2.** Comparison of dimensionless mass flow rate computed by different methods at  $p_e/p_0$  varies from 0 to 0.9 and  $\delta$  from 100 to 1.

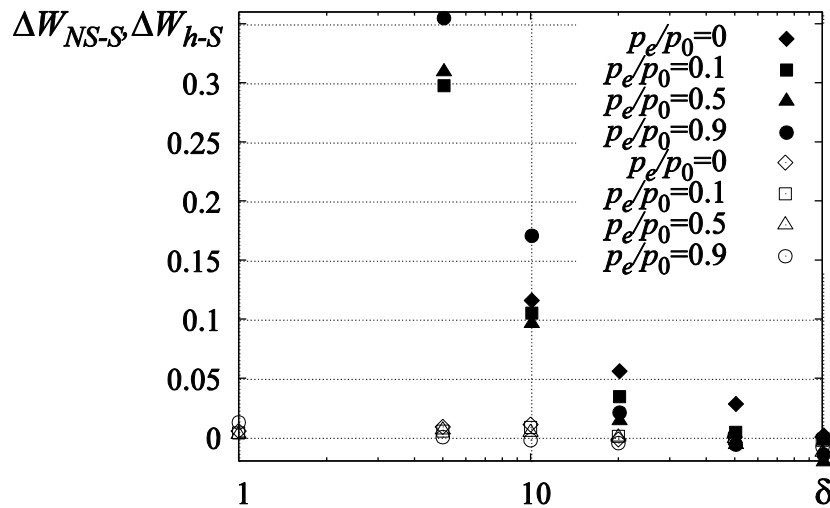
$p_e/p_0$	$\delta$	$W_h$	$W_S$	$W_{DSMC}$ , [46]	$W_{NS}$
0	100	1.581	1.581	1.568	1.577
	50	1.580	1.580	1.568	1.534
	20	1.549	1.546	1.541	1.458
	10	1.466	1.482	1.479	1.309
	5	1.373	1.385	1.381	
	1	1.148	1.154	1.148	
0.1	100	1.569	1.565	1.561	1.566
	50	1.560	1.558	1.560	1.550
	20	1.523	1.524	1.531	1.470
	10	1.450	1.462	1.467	1.307
	5	1.337	1.344	1.349	0.943
	1	1.072	1.076	1.060	
0.5	100	1.42	1.402	1.383	1.430
	50	1.396	1.394	1.384	1.401
	20	1.35	1.350	1.344	1.330
	10	1.233	1.235	1.237	1.115
	5	1.011	1.015	1.015	0.700
	1	0.655	0.657	0.640	
$W_{BGK}$ , [43]					
0.9	100	0.736	0.730	0.7293	0.74
	50	0.709	0.710	0.7097	0.7138
	20	0.596	0.593	0.591	0.580
	10	0.406	0.405	0.4058	0.3355
	5	0.267	0.267	0.2686	0.172
	1	0.1418	0.1436	0.1419	

In Table 2 dimensionless mass flow rates  $W$  computed using kinetic approaches (DSMC [46], BGK [43] and S-model equations); continuum NS equations and hybrid solver are given for the pressure ratio of 0, 0.1, 0.5 and 0.9 and rarefaction parameter  $\delta$  ranging from 1 to 100. Assuming the kinetic solution as the reference one, we may define the relative error induced by other approaches as:

$$\Delta W_{h-S} = 1 - \frac{W_h}{W_S}, \quad \Delta W_{NS-S} = 1 - \frac{W_{NS}}{W_S} \quad (88)$$

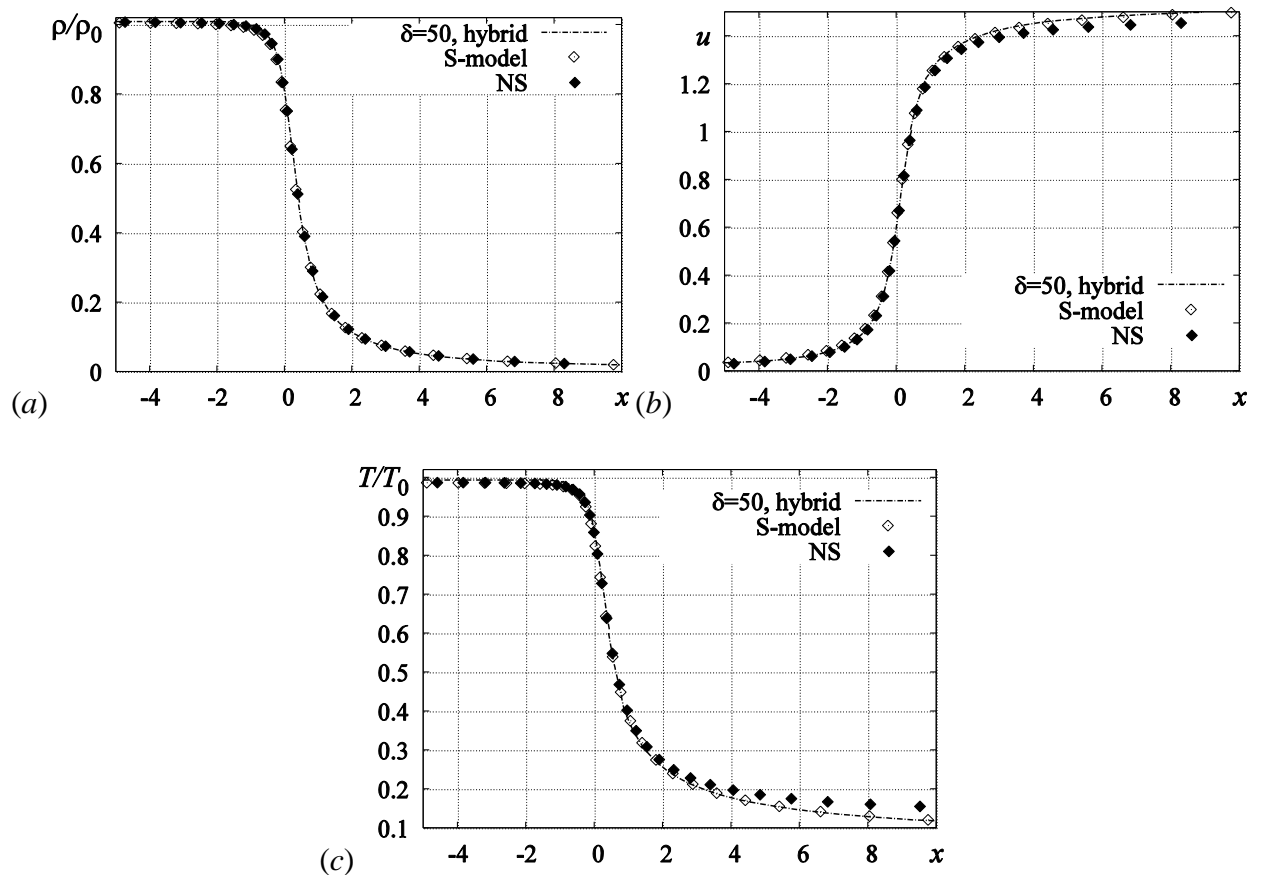
These relative differences of NS equations and hybrid method computed mass flow rates from kinetic values at different pressure ratios  $p_e/p_0$  and rarefaction parameters  $\delta$  are shown in Fig. 3.

One can see that the flow rate  $W$  given in Table 2 tends to a constant value depending only on the pressure ratio  $p_e/p_0$  in the slip regime ( $\delta > 50$ ). For the rarefaction parameter  $\delta$  from 1 to 50 and all pressure ratios  $p_e/p_0$  a significant variation of the mass flow rate  $W$  can be observed. The relative variation of the mass flow rate increases with a pressure ratio increase. In the case of outflow into vacuum ( $p_e/p_0 = 0$ ), the value of the flow rate  $W$  in the slip regime ( $\delta \approx 100$ ) is 1.34 times larger than its value in the transition regime ( $\delta = 1$ ), while for the pressure ratio  $p_e/p_0 = 0.9$  the flow rate increase is 5 times.

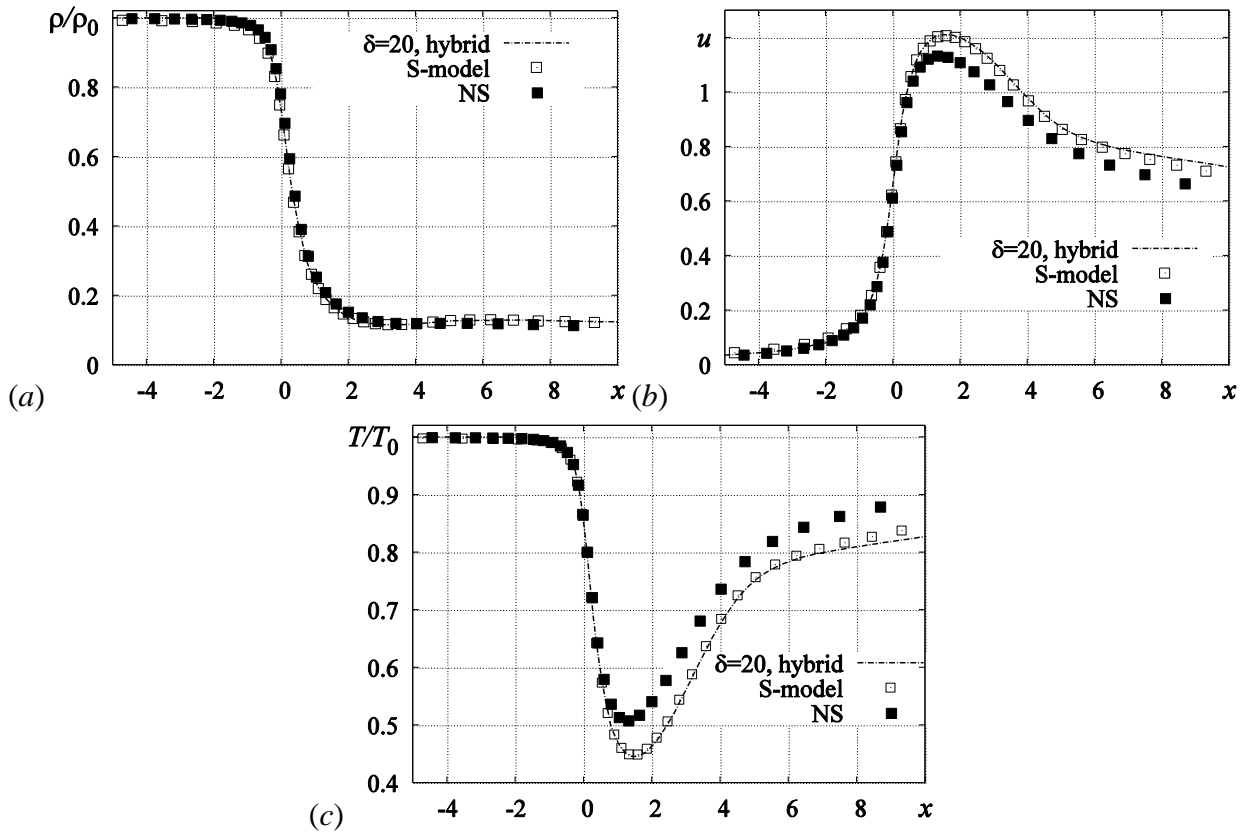


**Fig. 3.**  $\Delta W_{NS-S}$  (solid symbol) and  $\Delta W_{h-S}$  (empty symbol) via  $\delta$  at different  $p_e/p_0$ .

For high pressure ratios ( $p_e/p_0 = 0.5$  and  $0.9$ ) and rarefaction in the slip regime ( $\delta \geq 20$ ) mass flow rates obtained by hybrid, kinetic and NS solvers are close to each other: maximum difference between results is less than 2%. When gradients of macroparameters become higher the local Knudsen number can drastically increase: thus, at the same rarefaction parameter  $\delta$ , we can have higher local Knudsen for lower pressure ratio (close to vacuum); e.g., for pressure ratio  $p_e/p_0 = 0.1$  and  $\delta = 20$  the difference between NS and kinetic results is 3.6%; for flow into vacuum the difference is already around 3% at  $\delta = 50$  and 6% at  $\delta = 20$ . For smaller  $\delta$  the difference between NS and kinetic mass flow strongly increases up to 31% ( $p_e/p_0 = 0.1$  and  $0.5$ ) and slightly higher around 35% (at  $p_e/p_0 = 0.9$ ) for  $\delta = 5$ . On the other hand, the hybrid code always successfully produces mass flow rates close to kinetic data (difference within 1%).

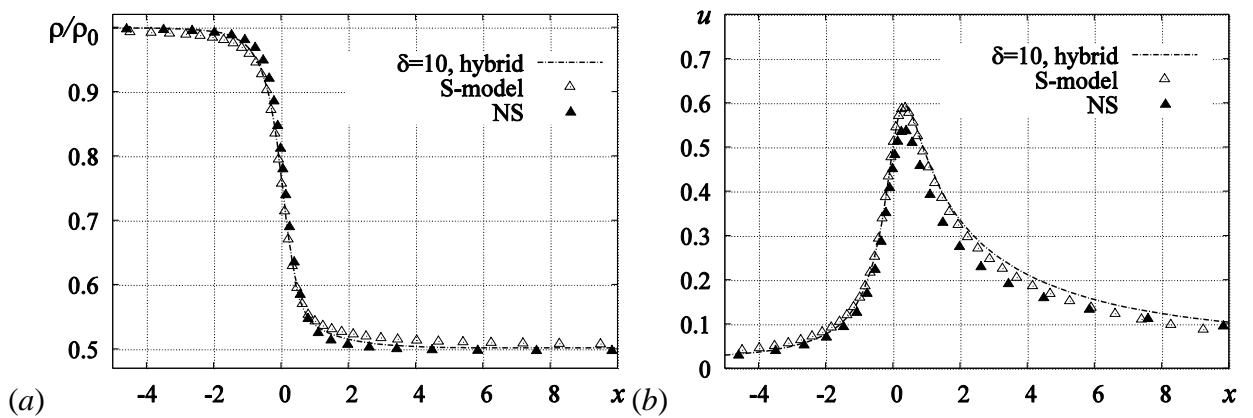


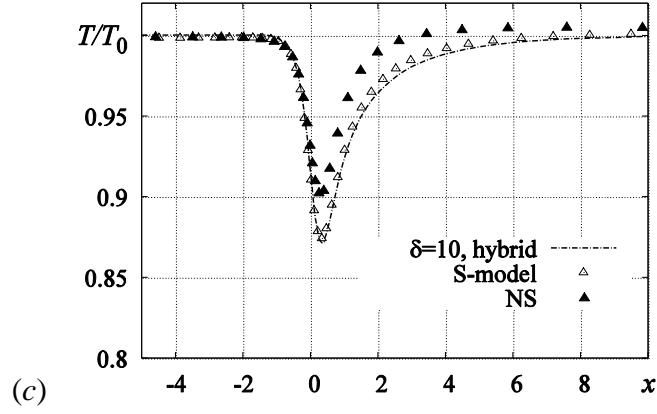
**Fig. 4.** (a): density  $\rho/\rho_0$ ; (b): axial velocity  $u$ ; (c): temperature  $T/T_0$  along the symmetry axis  $y = 0$ ,  $\delta = 50$ ,  $p_e/p_0 = 0$ .



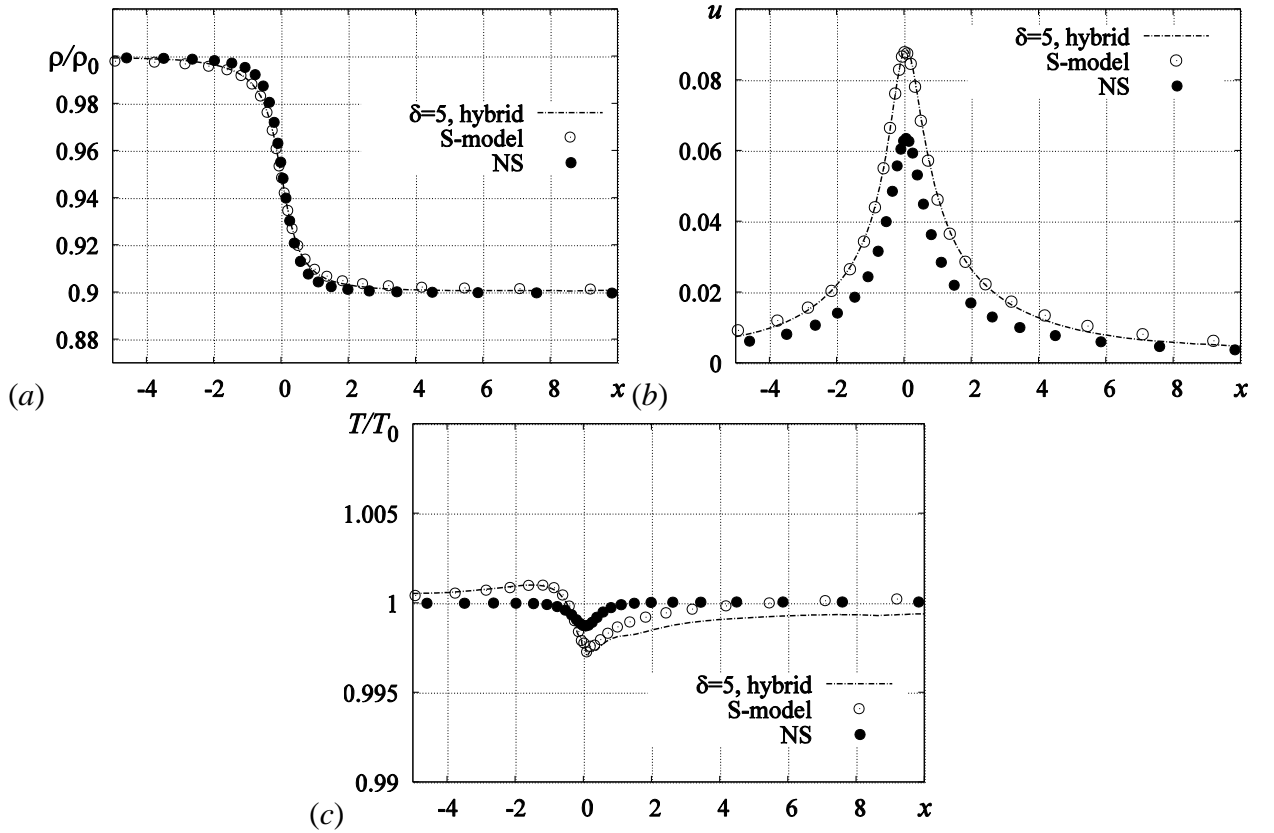
**Fig. 5.** (a): density  $\rho/\rho_0$ ; (b): axial velocity  $u$ ; (c): temperature  $T/T_0$  along the symmetry axis  $y = 0$ ,  $\delta = 20$ ,  $p_e/p_0 = 0.1$ .

Profiles of dimensionless density, temperature, normalized by inlet values, and velocity along the symmetry axis  $y = 0$  are shown in Figures 4-7 for  $p_e/p_0 = 0$  and  $\delta = 50$ ;  $p_e/p_0 = 0.1$  and  $\delta = 20$ ;  $p_e/p_0 = 0.5$  and  $\delta = 10$ ;  $p_e/p_0 = 0.9$  and  $\delta = 5$ . The combination of  $p_e/p_0$  and  $\delta$  for each case was chosen in order to demonstrate noticeable difference between NS and S-model solutions.





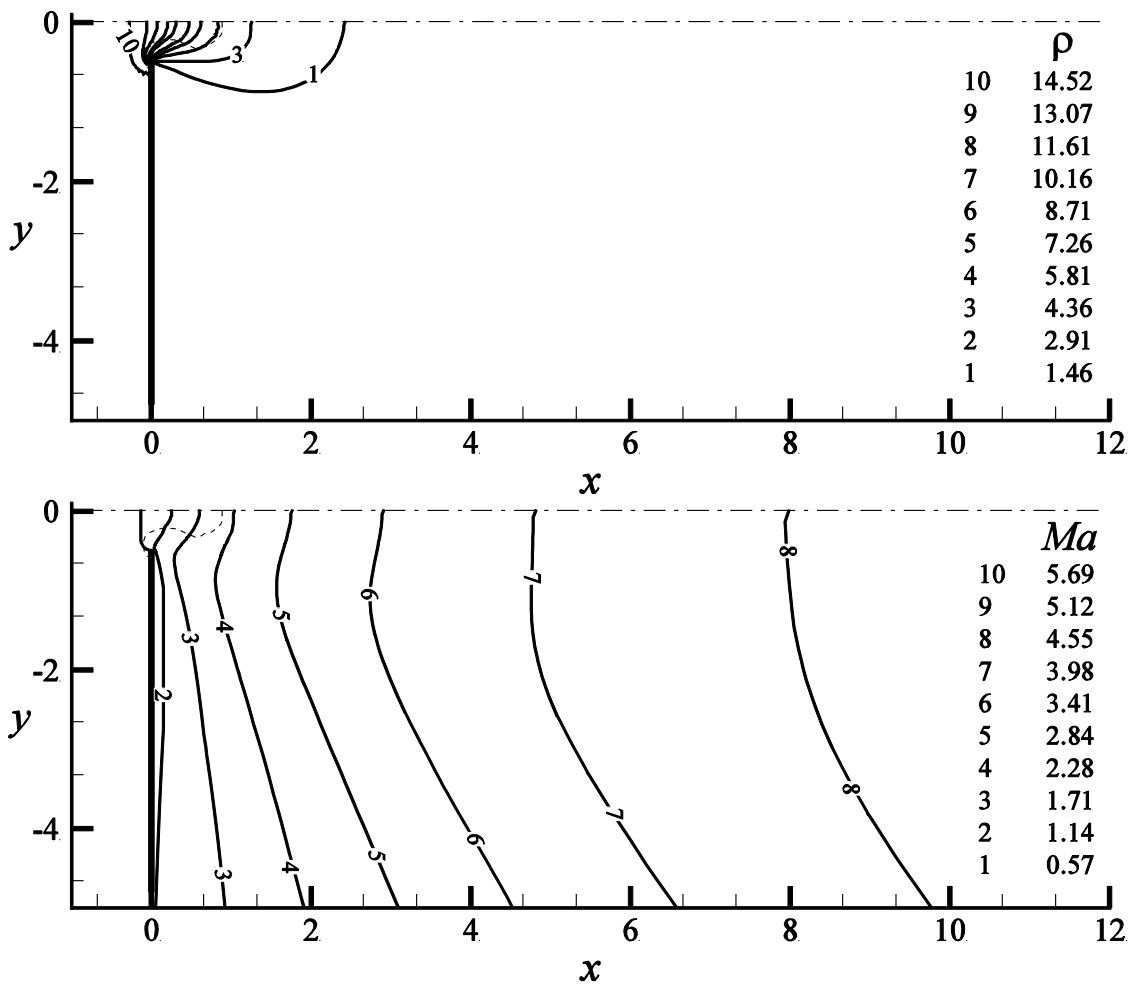
**Fig. 6.** (a): density  $\rho/\rho_0$ ; (b): axial velocity  $u$ ; (c): temperature  $T/T_0$  along the symmetry axis  $y = 0$ ,  $\delta = 10$ ,  $p_e/p_0 = 0.5$ .



**Fig. 7.** (a): density  $\rho/\rho_0$ ; (b): axial velocity  $u$ ; (c): temperature  $T/T_0$  along the symmetry axis  $y = 0$ ,  $\delta = 5$ ,  $p_e/p_0 = 0.9$ .

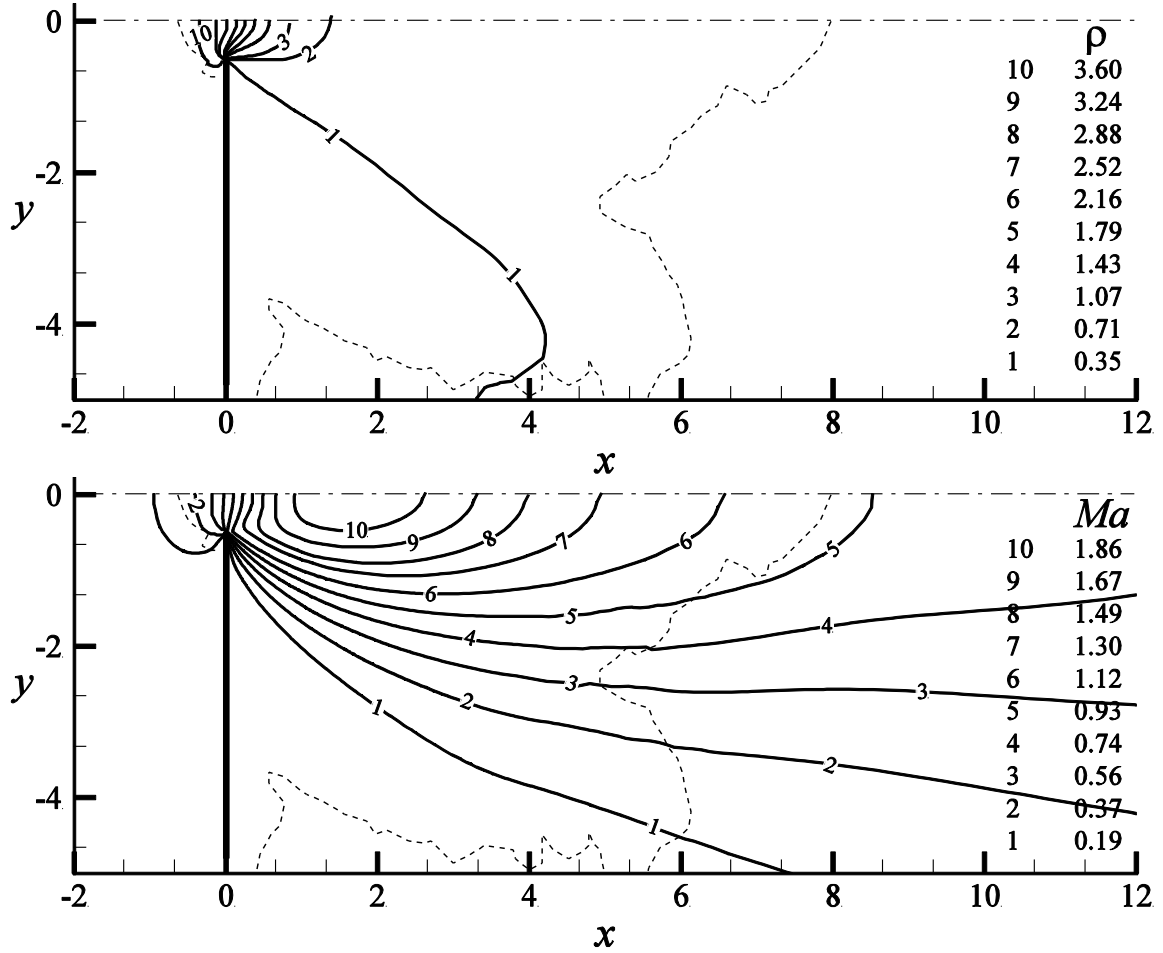
Coupled solutions are compared with both pure kinetic S -model and NS results. Upstream of the slit, for all cases we have a strong acceleration of the flow, and the corresponding decrease in density and temperature (thus, in pressure, not shown in the pictures). Downstream of the slit, we have different flow regimes, depending on the pressure ratio. As will be confirmed by Mach number maps, at vacuum condition we have a monotone supersonic expansion, while at the

highest ratio  $p_e/p_0 = 0.9$  we have a subsonic flow everywhere and a nearly symmetric behaviour upstream and downstream of the slit. At intermediate pressure ratios, downstream of the slit we have first a supersonic expansion/acceleration followed by a subsonic pressure recovery/deceleration. Coupled solutions are satisfyingly close to the kinetic ones for all values of pressure ratio  $p_e/p_0$  and rarefaction parameter  $\delta$ . On the other hand, NS results, under any set of condition, from slip to transition regime, consistently underestimate downstream velocities, and overestimate temperature levels. This seems due to an overestimation of the friction effect on the flow. At higher rarefaction NS results show even significant discrepancy with kinetic ones ahead of the slit, and as has been shown there is a difference also in mass flow rate.



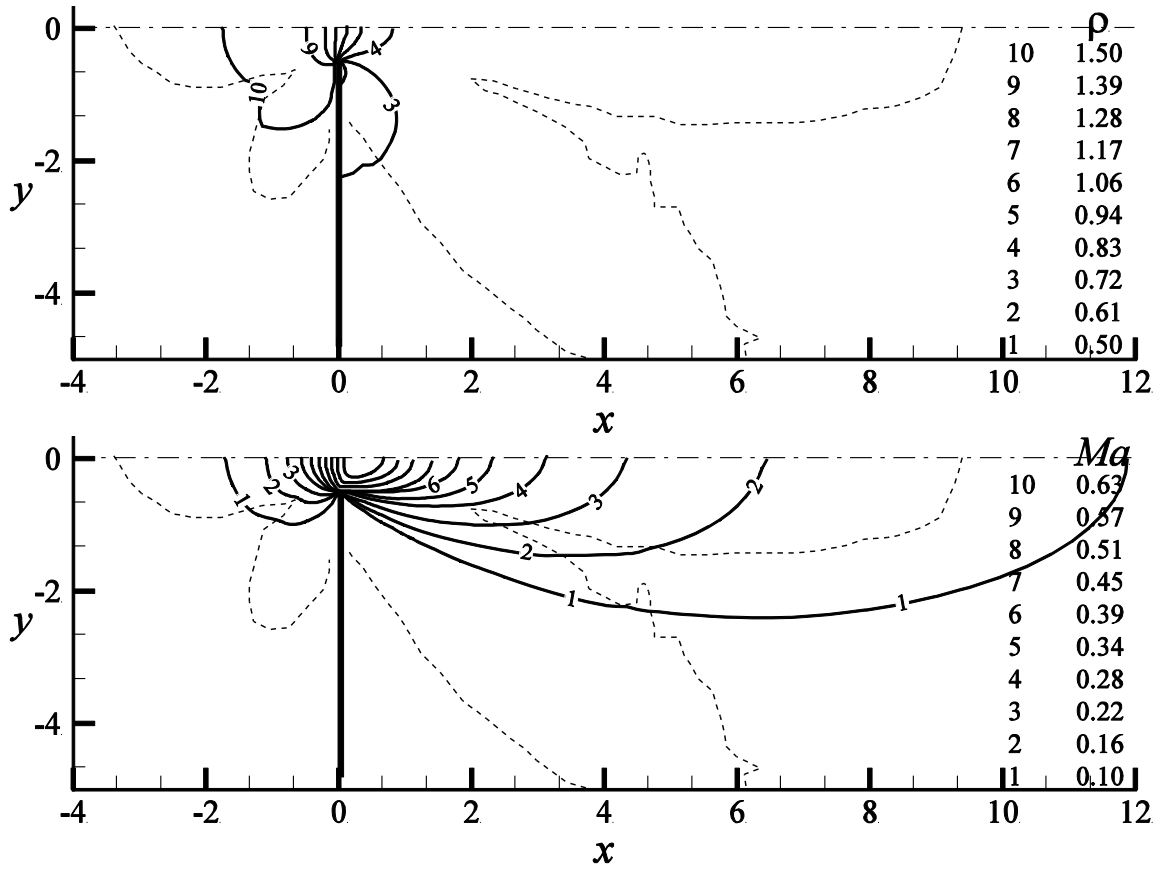
**Fig. 8.** Dimensionless density (top) and Mach number (bottom) contours (solid line) near the slit at  $\delta = 50$  and  $p_e/p_0 = 0$ ; dashed line shows kinetic region at convergence.

Contour lines of density and Mach number (solid line) near the slit region for different rarefaction are presented in Figures 8-11, together with the extension of the kinetic region at convergence (dashed line).



**Fig. 9.** Dimensionless density (top) and Mach number (bottom) contours (solid line) near the slit at  $\delta = 20$  and  $p_e/p_0 = 0.1$ ; dashed line shows kinetic region at convergence.

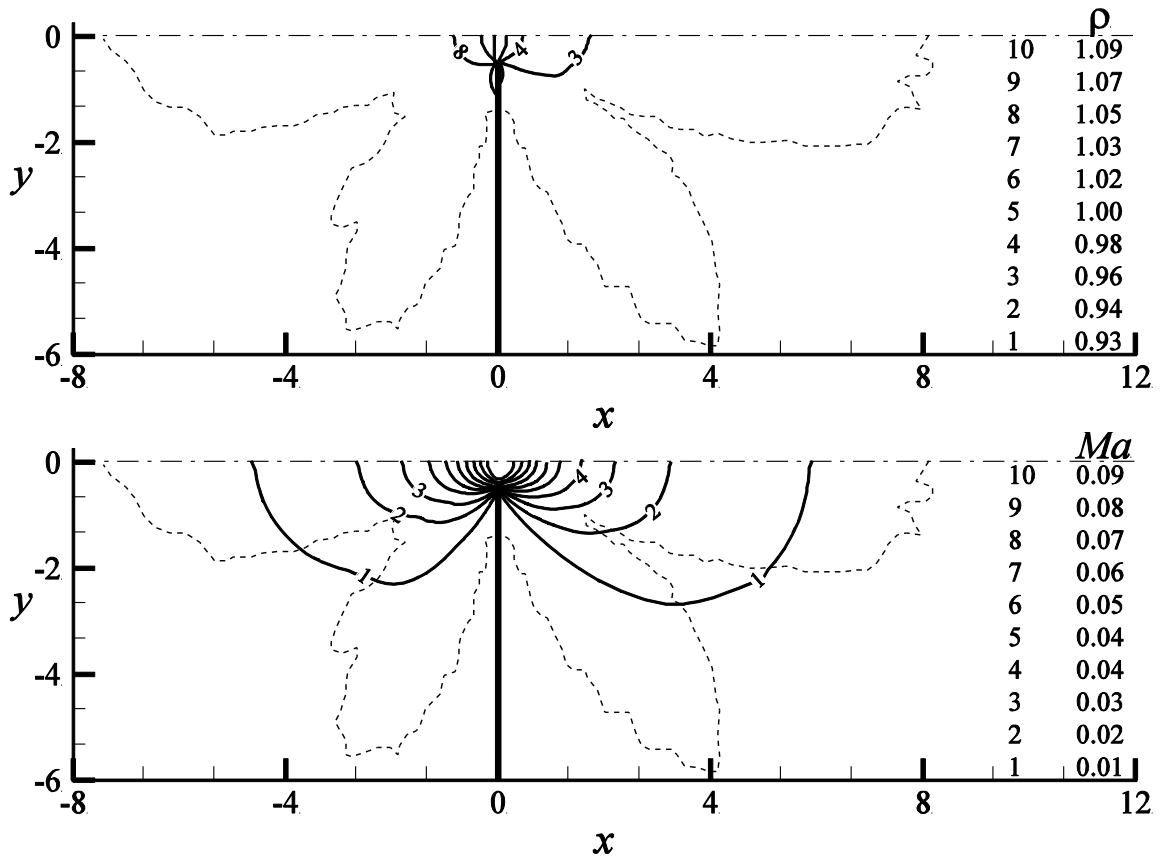
For small rarefaction  $\delta = 50$  (Fig. 8), flow into vacuum, the local Knudsen number near the coupling boundary varies from 0.035 to 0.078. The local Knudsen number, despite the low value of  $\delta$ , increases downstream, due to the supersonic expansion, and reaches the maximum value, far from the slit, around of 60. For rarefaction  $\delta = 10$  and  $p_e/p_0 = 0.5$ , Fig. 10, the local Knudsen number near the coupling boundary varies from 0.067 to 0.4, while the maximum local Knudsen number occurs near the slit and is equal to 1.53.



**Fig. 10.** Dimensionless density (top) and Mach number (bottom) contours (solid line) near the slit at  $\delta = 10$  and  $p_e/p_0 = 0.5$ ; dashed line shows kinetic region at convergence.

For the smaller rarefaction parameter value,  $\delta = 5$ , and  $p_e/p_0 = 0.9$ , shown in Fig. 11, the local Knudsen near the boundary is higher, varying from 0.195 to 0.178, and its maximum value is 0.21 near the slit. Nevertheless, despite of high value of local Knudsen near the coupling boundary in cases  $p_e/p_0 = 0.5$  and 0.9 the coupling between kinetic and NS solutions shows a smooth transition along the contour lines crossing the domains interface, especially for the Mach number contour. Moreover, as can be seen in Figs. 4-7 NS equations do not give appropriate solution especially for velocity and temperature.

CPU time per time step of hybrid code  $t_h$  is the sum of the time required for the solution of the S-model equation in  $N_K$  kinetic points ( $N_K$  is estimated from converged hybrid solution), of NS equations and the coupling procedures. Since the sum of CPU times relative to NS solution and coupling computation is quite small in comparison to the kinetic solution requirements, time  $t_h$  is essentially dictated by the number of  $N_K$  kinetic points should be solved during computation.



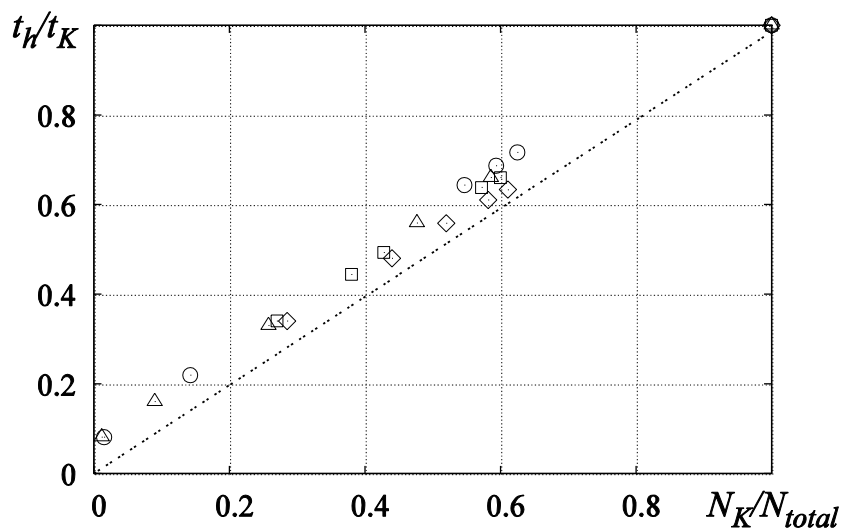
**Fig. 11.** Dimensionless density (top) and Mach number (bottom) contours (solid line) near the slit at  $\delta = 5$  and  $p_e/p_0 = 0.9$ ; dashed line shows kinetic region at convergence.

Figure 12 presents the CPU time per step of hybrid code  $t_h$  normalized to CPU time per step of pure kinetic S-model code  $t_K$  as a function of the ratio of kinetic points  $N_K$  to the total number of grid points  $N_{total}$ . It can be seen that if the number of kinetic points  $N_K$  with respect to total number of computational points  $N_{total}$  is small,  $t_h$  is 10-15 times smaller than CPU time needed for the full kinetic solution  $t_K$ . When the number  $N_K$  increases CPU hybrid time  $t_h$  tends to the kinetic time  $t_K$ . Obviously, the highest CPU time gains (up to 85%) occurs at low rarefaction, when the kinetic region is small, and thus, even the pure NS solution could give a reasonably good accuracy. For example, pure kinetic computation at  $p_e/p_0 = 0.5$  and  $\delta = 50$  on physical mesh of  $320 \times 40$  and velocity mesh of  $24 \times 24$  costs 0.745 s, while hybrid time step  $t_h$  is only 0.120 s (number of kinetic points  $N_K = 1150$ ) and the NS step is  $t_{NS} = 0.029$  s. Nonetheless, the hybrid code offers a CPU time gain of at least 30-40% under any condition, even those where Navier–Stokes solution would be completely inadequate. In case flow into vacuum  $p_e/p_0 = 0$  and

high rarefaction level  $\delta = 5$  (mesh of  $400 \times 60$  nodes in physical space,  $64 \times 64$  in velocity space are used) pure kinetic time step  $t_K$  required 10 s, while  $t_h$  only 6.3 s ( $N_K = 14600$ ). The Navier – Stokes time step  $t_{NS}$  in this case is almost negligible 0.08 s.

Furthermore, Fig. 12 also reports the speed up per time step achieved close to convergence, when the kinetic region size is stable. The total CPU advantage over the whole computation, with the dynamic coupling, is thus appreciably greater, since at the beginning of the computation the kinetic area is typically much smaller than at converged state. It should be noticed that for comparison reason the size of inlet/outlet reservoirs around slit is the same for all solvers. Further acceleration of hybrid solver can be reached by decreasing the size of reservoirs, since for the continuum solver it is easier to specify inlet/outlet boundary conditions at sections closer to the slit. This accelerates convergence of NS solver in NS region which is important for slow flow caused by high pressure ratio ( $p_e/p_0 \geq 0.5$ ).

Points for all pressure ratios are aligned along a single line, with the only exception of the case  $p_e/p_0 = 0$  (flow into vacuum), where the hybrid code offers an even better advantage. This is due to the need for a larger grid in velocity space ( $64 \times 64$ ) in the kinetic solution, and the corresponding increase in CPU time; the computation of NS equation and coupling part becomes thus almost negligible in comparison with a kinetic part.



**Fig. 12.** Relative CPU time for hybrid simulations:  $\diamond$  -  $p_e/p_0 = 0$ ;  $\square$  -  $p_e/p_0 = 0.1$ ;  $\Delta$  -  $p_e/p_0 = 0.5$ ;  $\circ$  -  $p_e/p_0 = 0.9$ .

Moreover, using dynamic coupling results with the same level of accuracy can be obtained with lower number of kinetic points. As an example, in [10] using the static coupling, a ratio of kinetic points to the total number of points in computational domain up to 0.2 ( $p_e/p_0 = 0.5$  and  $\delta = 100$ ) was necessary, while for dynamic coupling comparable results were achieved with a significant lower ratio (0.01, in converged state).

It should be mentioned that parallelization in the velocity space allow us to uniformly distribute kinetic points between processors. Each processor works with the same number of kinetic points in physical space, allowing for good process balance and parallelization efficiency. Now the speed up of hybrid code is 7.45 running on 8 processors estimated for the case of  $\delta = 50$  and  $p_e/p_0 = 0$ .

## 4.5. Conclusions

A hybrid algorithm based on the direct numerical solution of the S-model kinetic equation coupled with a Navier-Stokes solution was applied for the modeling gas flow through a slit for arbitrary pressure ratios, including the extrema of flow into vacuum and subsonic flow, within a range of Knudsen number from the slip flow to transition regime. It was shown that the hybrid code gives results close to full kinetic results for flow regimes, where the Navier-Stokes solution completely fails. The CPU time savings, with respect to the full S -model solution, are significant, although, as expected, strongly depend on the size of the kinetic region. It should be noticed that the dynamic coupling is more effective than static one, allowing to capture and describe properly kinetic regions even when they appear, during the convergence transient, in areas not easy to predict a-priori. This allows for satisfying results even with the smaller number of kinetic points.

## 5. Near wall modelling

### 5.1. Introduction

The numerical simulation of the gas flow near the wall offers additional challenges to numerical methods due to an appearance a wall – gas interaction. Moreover, at microscale the rarefaction effect becomes significant in the near-wall region. It is well known that the flow near a solid surface can be subdivided into a thin boundary layer, of the order of a few mean free path (so thin to be negligible for a macro configuration), which is a rarefied regime area and the internal core flow, which is continuum one. The rarefied domain is naturally described by kinetic equation which is time and memory consuming, due to the discretization in both physical and velocity space. On the other hand, the continuum domain is well described by the fluid Navier-Stokes (NS) equations coupled with slip boundary and temperature jump conditions on the solid surface. However, as indicated in the literature, the first order slip condition is valid only for local Knudsen number  $Kn$  lower than 0.1, and any attempt to increase their range, resorting to higher order slip boundary conditions, is not trivial and highly geometrical dependent.

In the previous section it was shown that the hybrid solver successfully reproduce results for the gas flow through the slit, but for this kind of flow the wall boundary effect is almost negligible [29, 30]. However, near-wall modeling, such as, for example, the gas flow through the channel, is dominated by the wall boundary effect. Thus, in order to have reliable apparatus applicable for the wide range of practical interest problems it is important to validate developed hybrid solver for the near wall modeling as well.

It is well known that in MEMS fabrication due to the small scale it is nearly impossible to create an actual smooth surface. On the other hand, a surface roughness may have a significant impact on microchannel performances, both in terms of pressure drop and heat transfer. Therefore, several experimental and numerical studies have been devoted, in the recent past, to the estimation of roughness effect in MEMS.

Earlier experimental results for microchannels showed a significant scattering, and a roughness effect was often suggested as a possible explanation even for discrepancies in continuum, incompressible flow. Mala and Li [47] have observed that for rough microchannels (relative roughness height from 0.7 to 3.5%) the pressure drop was higher than that predicted by the classical theory, and increased with Reynolds number increase. Wu and Little [48, 49] measured huge increases in friction factors for both laminar and turbulent flows in miniaturized channels etched in silicon and glass and attributed their anomalous results to the large relative (and asymmetric) roughness of test channels. Choi et al. [50] measured friction factors of nitrogen flow in microtubes of diameter ranging from 3 to 81  $\mu\text{m}$  and found it to be consistently smaller than those predicted by the macro scale correlation in macro tubes.

More recent papers have demonstrated that roughness effect in a laminar, incompressible flow can be described by means of standard macroscale equations and correlations [51], taking into account proper scaling effects and via a proper definition of the hydraulic diameter. Artificial saw tooth roughness effects have been investigated in [52]. Results, obtained in the laminar regime, showed that experiments fit the constant Poiseuille number rule for smooth tubes, provided that the reference length was defined with respect to the constrained diameter measured at the top of ridges. A further discussion on the definition of hydraulic diameter, on the basis of numerical simulations for different rough shapes in incompressible flow, was given in [53].

However, for gas microflows, in particular when rarefaction effects appear, there are still open problems. Furthermore, at such small scales it is quite difficult to experimentally pick out the actual effect of roughness, which is often masked by several uncertainty sources. For example, Turner et al. [54] remarked that any roughness effect was within experimental error bar, and Lorenzini et al. [55] notice no significant roughness effect at low rarefaction levels, while compressibility effect was more notable. Nonetheless, Demsis et al. [56] analysis of experimental data strongly suggested that roughness can affect Poiseuille number in a

microchannel rarefied flow, although an experimental uncertainty did not allow a definitive answer yet; furthermore, Tang et al. [57] have found that roughness matters if higher than 1%.

The numerical modeling, on the other hand, offers an appealing alternative to experiment, allowing a detailed description of surface imperfections, where the roughness effect can be easily separated from other microscale effects. The roughness problem has been first addressed, both via direct numerical analysis and simplified modeling, mainly in the incompressible, no-slip flow regime. Numerical simulations of the pressure driven flow in the presence of different, regular or random roughness shapes were carried out in [57-60]. In [61] the use of an equivalent porous layer in the rough region along the wall was proposed. This concept was extended to the heat transfer problem in [62]. Numerical computations have been compared with such simplified models in [59].

Results for rarefied flows have been obtained in [63, 64] using DSMC method. Knudsen numbers in the range from 0.02 to 0.12 were considered, in the presence of very large roughness geometries, from 5% up to 12%. In both papers, the low Mach number level prevented any compressibility effect. In [65] the coupled effect of rarefaction and roughness, neglecting compressibility, has been considered via the Lattice Boltzmann equation.

The interaction with compressibility was taken into account in [66], in which the influence of roughness in the slip flow regime with the second order slip boundary conditions for the exit Mach number up to 0.5 has been studied. The roughness was simulated as rectangular elements on two parallel plates and it was shown that the effect of wall roughness was reduced with Knudsen number increase. The prediction of roughness effect on a pressure drop for gaseous flow, in the presence of compressibility up to choked flow conditions and/or rarefaction effects, has been analyzed in [67-69] using NS equations coupled with a standard first-order slip boundary condition. It should be mentioned that the surface texture is also affected heat transfer performances [70]. Few more references summarized in [71] confirm that a proper assessment of roughness effect is necessary for accurate heat transfer analysis.

Kinetic approach based on the solution of S-model equation for analysis a 2D compressible gas flow through a rough microchannel was used in [72]. The effect of roughness modeled as a series of triangular obstructions was considered for wide ranges of Mach (up to choked flow) and Knudsen numbers (from slip to transition regime). It was found that the surface roughness has a significant influence on a friction factor. The compressible gas flow was also sensitive to the height of the wall roughness element, but the compressibility effect is stronger than roughness one. For a highly rarefied gas flow rarefaction enhances roughness effect despite the fact that Po number decreases with  $Kn$  number increase.

Furthermore, the use of NS equations for the simulation of roughness effect may be critical due to the fact that a Knudsen number based on the hydraulic diameter is chosen as a measure of the rarefaction effect in standard smooth microchannels. At the same time, the roughness scale is much smaller, typically a few per cent, of the hydraulic diameter. Thus, the choice of most appropriate length scale, i.e. the hydraulic diameter, for the description of the roughness effect is not obvious. In principle, the applicability of the continuum numerical approach based on the solution of NS equations should be limited to flows, where the roughness size is much smaller than the mean free path of the gas. This condition may not be fulfilled in actual application of practical interest; thus, even if the use of appropriate slip boundary conditions allows to partially overcome this limitation, a correct description of the gas-roughness interaction should require an expensive kinetic numerical approach, at least near the rough surface.

Here, the hybrid solver is applied to the simulation of the rarefied gas flow through the channel of finite length caused by an arbitrary pressure ratio. The effect of applying different breakdown criteria on the flow field is considered. Hybrid results are compared with pure kinetic and NS solutions, for different pressure ratios and a Knudsen number in the slip regime. Obtained results are discussed in terms of both accuracy and computational efficiency.

Further, the hybrid solver was used to study the actual engineering problem: effect of the surface roughness on the gaseous flow in MEMS. Moreover, the reliability of the first order slip

boundary condition for the simulation of flows along rough fine-textured surface geometries is estimated. Although the analysis here is limited to the effect on pressure drop and Poiseuille number, an assessment of the validity of slip flow condition for fine textured geometries is also an essential prerequisite for reliable heat transfer computations.

## 5.2. Statement of the problem

The two-dimensional pressure-driven monatomic gas flow through a planar microchannel of width  $H$  and length  $l = 10H$  connecting two reservoirs of size  $L_x \times L_y$  is considered. The gas in reservoirs far from the channel is in equilibrium at constant pressures  $p_0$  and  $p_e$ , ( $p_0 > p_e$ ), and temperature  $T_0$ . The temperature of the walls  $T_w$  is equal to the temperature in reservoirs  $T_0$ . Since the flow is symmetric about  $y = 0$  only a half of the domain, shown in Fig. 13 is simulated.

For sake of computational efficiency only a small channel part of length  $L_r = 3.15 H$  placed near the channel exit is modelled as a rough one, while the rest of the channel and reservoirs walls are smooth, see Fig. 13a. Thus, at low pressure ratio (low  $Ma$ ), the inlet smooth region allows for fully developed flow approaching the rough region. The wall roughness, shown in Fig. 13b, is modelled as a series of triangular obstructions with a sharp angle of 45 degrees. The height of a single peak is  $h = \varepsilon H$  and the distance between peaks is  $s = 5h$ . Several relative roughness values  $\varepsilon$  have been considered: 1.25%, 2.5% and 5%. Hence, the rough region of  $3.15H$  long includes 12 roughness ridges for  $\varepsilon = 5\%$ , and 24 ridges for  $\varepsilon = 2.5\%$  and 48 ridges for  $\varepsilon = 1.25\%$ . It should be noticed that the interface  $I_c$  between kinetic and NS sub-domains is dynamically updated during the computation.

The gas flows due to a pressure ratio  $p_e/p_0$  between upstream and downstream reservoirs. The static inlet pressure  $p_i$  is the result of computation, although, due to the low inlet velocities, it almost coincides with inlet total pressure  $p_0$ . The gas flow is also determined by the rarefaction parameter  $\delta$  (or Knudsen number  $Kn$ ).

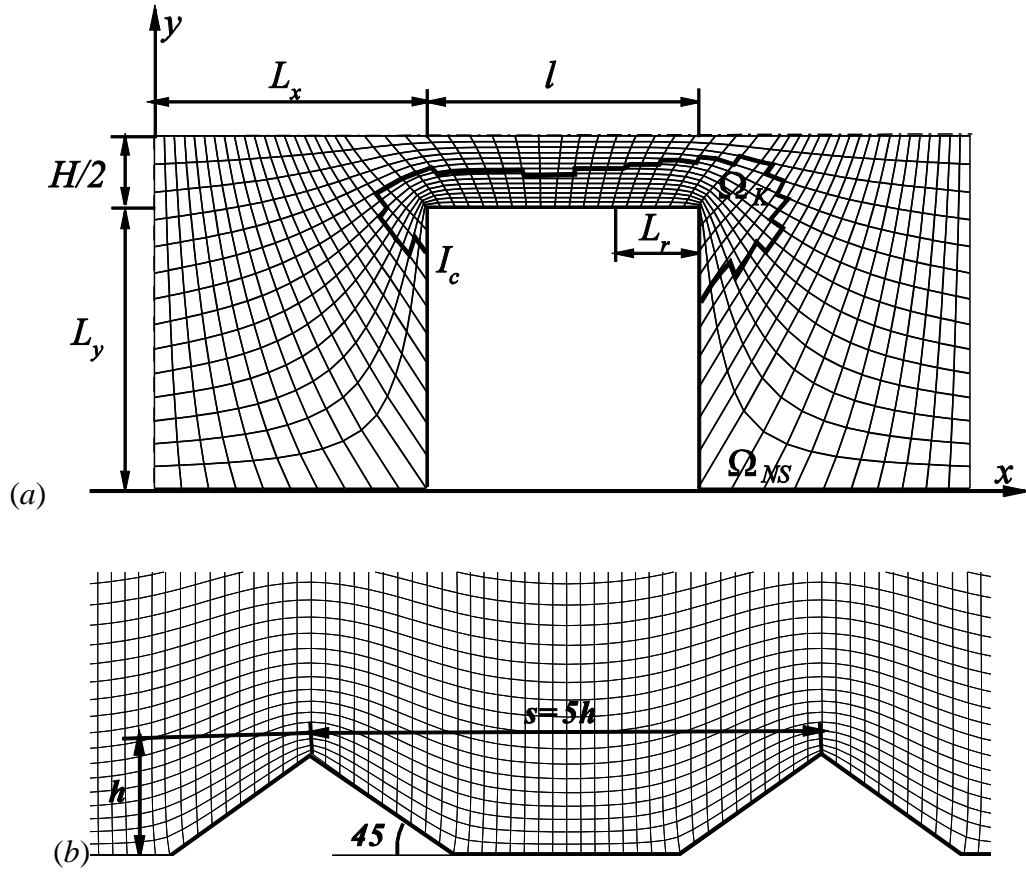


**Fig. 13.** Sketch of computational domain and rough elements details.

The channel global and local performance in terms of the Poiseuille number  $Po$  and dimensionless mass flow rate  $W$  defined as eq. (85) will be presented. The mass flow rate through the channel is constant and computed at channel mid-section  $x = 1/2L$  using formula (86). The friction factor  $f_r$  is defined as an average value either over a portion of rough channel section or over a single geometrically periodic roughness element of length  $s$ . In both cases,  $f_r$  is computed as:

$$f_r = 2 \frac{\Delta \bar{p}}{\Delta L} \frac{D_h}{\bar{\rho}_{av} \bar{u}_{av}^2} = 2 \frac{\Delta \bar{p}}{\Delta L} \frac{D_h \bar{\rho}_{av}}{\bar{m}_{av}^2} \quad (89)$$

where  $D_h$  is the hydraulic diameter,  $D_h = 2H$ , overbar means averaged values over cross section,  $\Delta$  and  $av$  are the difference and the averaged between inlet and outlet values. The Poiseuille number  $Po$  is then written in terms of the local  $Re$  as:

$$Po = f_r \cdot Re = 2 \frac{\Delta \bar{p}}{\Delta L} \frac{D_h^2}{\bar{\mu}_{av} \bar{u}_{av}} = 2 \frac{\Delta \bar{p}}{\Delta L} \frac{\bar{\rho}_{av} D_h^2}{\bar{\mu}_{av} \bar{m}_{av}} \quad (90)$$

$$Re = \frac{\bar{\rho}_{av} \bar{u}_{av} D_h}{\bar{\mu}_{av}} = \frac{\bar{m}_{av} D_h}{\bar{\mu}_{av}} \quad (91)$$

Due to the conservation of mass flow rate,  $Re$  will change only slightly along the channel, because of the  $\mu$  variation with temperature.

Unless otherwise stated,  $Po$  is computed between the inlet and outlet section of a rough sector  $L_r$  of length  $L^* = 2.25 H$ , (i.e., skipping small regions both at the inlet and exit of a rough sector in order to avoid entrance and exit effects), i.e. including 9, 18 and 42 rough modules, for relative roughness height  $\varepsilon = 5\%$ ,  $\varepsilon = 2.5\%$  and  $\varepsilon = 1.25\%$ , respectively.  $Po$  number for smooth channel ( $\varepsilon = 0$ ) is computed over the same section  $L^* = 2.25 H$ .

For incompressible flow through a smooth channel with the first order slip boundary condition there is an analytical expression for the Poiseuille number:

$$Po_s = \frac{96}{1 + 6 \cdot s_p \cdot Kn} \quad (92)$$

For either compressible or rough surface flows no analytical solution is available. However, a few correlations have been proposed recently in the literature. In particular, an expression for rough surfaces, based on results obtained by Lattice Boltzmann computations, was proposed in [65]:

$$Po_\varepsilon = 0.9 Po_s \times (1 + 0.8 \times 2\varepsilon + 24 \times (2\varepsilon)^2) \quad (93)$$

It should be noticed that Lattice Boltzmann results computed for roughness modelled as rectangular obstacles and hydraulic diameter was computed as  $D'_h = 2H' - \varepsilon'$ , where  $H'$  is height of half channel and relative roughness height is  $\varepsilon' = h/H'$ .

Asako et al. [69] suggested a local  $Po$  correlation for a developing compressible flow:

$$Po_{comp} = 96 - 4.55 \times Ma + 274.8 \times Ma^2 \quad (94)$$

The problem is recast in terms of non-dimensional variables using inlet reservoir equilibrium values as reference ones: density  $\rho_0$ , temperature  $T_0$ , most probable velocity  $v_0 = (2kT_0/m)^{0.5}$  ( $m$  is the particle mass), reference dynamic viscosity  $\mu_0$  and height of the channel  $H$ .

## 5.2. Parameters of modelling

Series of computations have been carried out at pressure ratios  $p_e/p_0 = 0.1, 0.5, 0.33$  and  $0.9$  and a rarefaction parameter  $\delta$  from  $100$  to  $10$ . The computational domain shown in Fig. 13a represents bottom half of inlet and outlet square shape reservoirs connected by the channel of length  $10$ . For pure kinetic computations the size of reservoirs should be large enough, thus it is chosen equal to  $L_x \times L_y = 30 \times 15$  [45]. Using hybrid solver allows to essentially decrease the size of reservoirs in comparison with a pure kinetic consideration, up to  $L_x \times L_y = 5 \times 3$ , thus significantly decrease computational time due to quicker convergence of NS solver.

In the physical space for smooth channel computations, a non uniform structured single block curvilinear grid of  $360$  nodes in the streamwise direction with a dimensionless minimum grid spacing  $0.02$  and  $40$  nodes in the transverse direction (dimensionless minimum grid spacing  $0.008$  near the wall) is used. Grid independence test has been done using a coarse grid with  $240 \times 30$  nodes. The mass flow difference between finer and coarse meshes is less than  $1\%$ .

In order to accurately model rough geometry  $712$  nodes in the streamwise direction (dimensionless minimum grid spacing is  $0.004$ ) and  $40, 45$  and  $50$  nodes in the transverse direction have been used for  $\varepsilon = 5\%, 2.5\%$  and  $1.25\%$ , respectively. Minimum grid spacing close to the wall is around  $0.003$ . Decreasing the minimum grid spacing near the wall up to  $0.001$  introduces maximum differences for the Poiseuille number and the mass flow rate less than  $0.8\%$  and  $0.2\%$ , respectively, for all (NS, kinetic and hybrid) solvers.

The size of uniform two-dimensional velocity grid should be selected large enough to capture all of the important features of the problem: thus, the velocity space boundary should

satisfy the following condition:  $v_{\max} \geq \max(|u|, |v|) + 3.5T_{\max}^{0.5}$ . For most of computations the number of grid points for each velocity component is 24 and velocity space is bounded by  $v_{\max} \approx 5$ . In case of very high gradient flow, i.e.  $p_e/p_0 = 0.1$ , the number of points is increased up to 40 and velocity space boundary  $v_{\max}$  up to 7.2. The optimal number of grid points in the velocity space was chosen checking that doubling velocity points produces a change in mass flow rate lower than 1-1.5%.

The time step is unique for both solvers and it should satisfy the stricter stability (or accuracy) constraint  $\Delta t = \min(\Delta t_K, \Delta t_{NS})$ . The explicit kinetic time step should be limited by the *CFL* condition with  $CFL = 0.4$ , while  $\Delta t_{NS}$  is arbitrary. The solution is considered to be converged when the criterion  $\|\mathbf{U}^{n+1} - \mathbf{U}^n\|_{L_2} < \Delta$  is fulfilled with  $L_2$  norm and  $\Delta = 10^{-7}$ .

### 5.3. Breakdown criteria comparison

As was shown in [12] for the flow through the slit breakdown criterion based on the gradient length Knudsen number  $Kn_{GL}$ , equation (16), with threshold value  $\Xi \leq 0.1$  guaranteed the difference between hybrid and kinetic solutions less than 1% (see Table 1). Here, we estimate the effectiveness of modified  $Kn_{GL}$  (using gradient of velocity magnitude  $|\mathbf{V}|$ ) and two more complex criteria  $B_{qt}$  (eq. (20)) and  $\|f_1(\mathbf{C})\|$  (eq. (21)) applying them to the near wall modelling and comparing hybrid solutions with the full Boltzmann computations [45]. It should be noticed that in low-speed regions of the flow, the velocity magnitude gradient in  $Kn_{GL}/N|*$  (see eq. (18)) is normalized using the velocity magnitude  $|\mathbf{V}|*$ , where  $|\mathbf{V}|* = |\mathbf{V}|$  if  $|\mathbf{V}| \geq v_{\min}$  and  $|\mathbf{V}|* = v_{\min}$  if  $|\mathbf{V}| < v_{\min}$ , in order to avoid singularities in the region where the flow velocity approaches to zero. Here,  $v_{\min}$  is taken equal to 5% of isoentropic velocity  $u_{is}$ , where  $u_{is} = Ma_{is}(0.5\gamma T_0)^{0.5}$ .

The Poiseuille number  $Po$ , defined by equation (90), is estimated as an averaged value over a channel section of  $\Delta L \approx 9$  (i.e., skipping small regions  $\Delta l \approx 0.5$  both at the inlet and exit of channel to avoid entrance and exit effects).

**Table 3.** Comparison of different criteria for a hybrid solver

	Criterion	$N_K$	$W_h$	$W_{BE}$ , [45]	$Po$	$Po_{kin}$
	$Kn_{GL}(\Xi = 0.1)$	5640	0.1840		52.3	
$p_e/p_0 = 0.5$	$B_{q\tau}(\Xi = 0.015)$	5640	0.1844	0.184	52.2	51.3
$\delta = 10$	$\ f_1\ (\Xi = 0.05)$	5700	0.1843		52.16	
	$Kn_{GL}(\Xi = 0.1)$	3030	0.515		92.47	
$p_e/p_0 = 0.5$	$B_{q\tau}(\Xi = 0.015)$	6800	0.515	0.51	92.4	91.6
$\delta = 50$	$\ f_1\ (\Xi = 0.05)$	5300	0.511		92.38	
	$Kn_{GL}(\Xi = 0.1)$	7050	0.277		47.26	
$p_e/p_0 = 0.1$	$B_{q\tau}(\Xi = 0.015)$	8160	0.280	0.280	46.95	46.2
$\delta = 10$	$\ f_1\ (\Xi = 0.05)$	7050	0.280		47.16	
	$Kn_{GL}(\Xi = 0.1)$	4270	0.604		103	
$p_e/p_0 = 0.1$	$B_{q\tau}(\Xi = 0.015)$	7770	0.605	0.604	102.8	102.5
$\delta = 50$	$\ f_1\ (\Xi = 0.05)$	8268	0.6045		102.8	

In Table 3 mass flow rate  $W_h$  and global Poiseuille number  $Po$  using different criterion at pressure ratio  $p_e/p_0 = 0.1$  and  $0.5$  and rarefaction level  $\delta = 10$  and  $50$  are presented. At  $p_e/p_0 = 0.5$  and  $\delta = 10$  for each criterion threshold value  $\Xi$  was chosen such as to provide a hybrid solution close to a kinetic one while using the same number of kinetic points  $N_K$ . For further computations chosen threshold value  $\Xi$  is kept for each criterion, i.e.:  $\Xi = 0.1$  for  $Kn_{GL}$ ,  $\Xi = 0.015$  for  $B_{q\tau}$  and  $\Xi = 0.05$  for  $\|f_1(\mathbf{C})\|$ . For both pressure ratios the maximum deviation of hybrid computed results from kinetic ones is around 1% for mass flow rate  $W$  and 2% for  $Po$  number. At the same time the difference between hybrid solutions computed with different

criteria is less than 1%. It should be noticed that for a low rarefaction level ( $\delta = 50$ ) the use of more complicated criteria  $\|f_1(\mathbf{C})\|$  and  $B_{q\tau}$  generates larger number of kinetic points in comparison with criterion  $Kn_{GL}$ , although the obtained accuracy is of the same order. Fig. 14, shows the kinetic region boundary and the coloured map of local gradient length Knudsen number for  $p_e/p_0 = 0.5$ . At  $\delta = 10$  or  $Kn \approx 0.1$  (see Fig. 14a), all criteria create almost identical kinetic regions. On the other hand, for lower rarefied flow,  $\delta = 50$  (Fig. 14b) criterion  $\|f_1(\mathbf{C})\|$  and  $B_{q\tau}$  unexpectedly create significantly larger kinetic region: 6800 points for  $\|f_1(\mathbf{C})\|$ , 5300 for  $B_{q\tau}$  in comparison with 3030 points for  $Kn_{GL}$ . Thus, the use of gradient length Knudsen number with threshold value  $\Xi = 0.1$  as breakdown parameter allows to produce hybrid results close to kinetic ones, while creating the smallest kinetic sub-domain. Therefore, for further near-wall computations modified  $Kn_{GL}$  with  $\Xi = 0.1$  will be used.

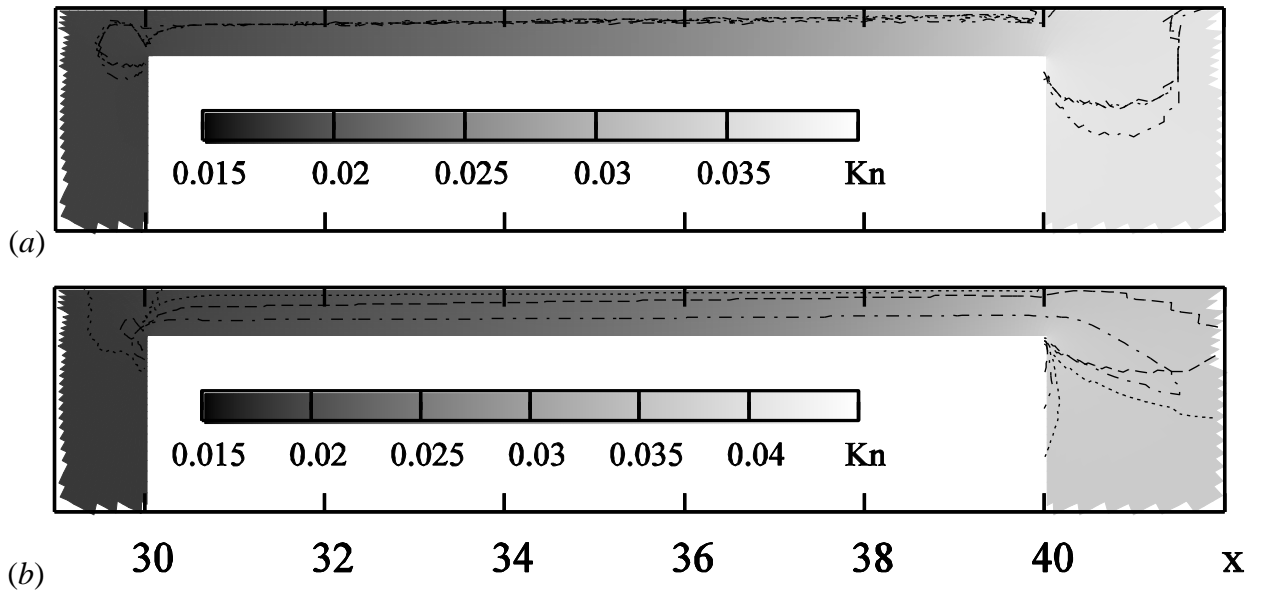


**Fig. 14.** Domain decomposition:  $Kn_{GL}$  (dashed dotted),  $B_{q\tau}$  (dashed),  $\|f_1\|$  (dotted) for  $p_e/p_0 = 0.5$ ,  $\delta = 10$  (a);  $\delta = 50$  (b).

## 5.4. Hybrid results discussion

### 5.4.1. Smooth channel

In Table 4 dimensionless mass flow rates  $W$  and averaged over the channel section of  $\Delta L \approx 9$  Poiseuille numbers  $Po$  (see eq. (87)) computed using kinetic approach (S-model equation), continuum NS equations and hybrid solver are given for the pressure ratio of 0.1, 0.33, 0.5 and 0.9 and rarefaction parameter  $\delta$  ranging from 10 to 100. It should be noticed that S-model results for mass flow rate are in a good agreement (the maximum difference within 2%) with pure kinetic Boltzmann and BGK results [45].

Assuming the kinetic solution based on the S-model equation as the reference one, we can estimate the relative difference between the pure kinetic and hybrid method and NS equations as:

$$\Delta(W, Po) = 1 - \frac{(W, Po)}{(W, Po)_s}, \quad (95)$$

in terms of global mass flow rate  $W$  and Poiseuille number  $Po$ .

These relative differences (from S-model results):  $\Delta W_{NS}$ ,  $\Delta Po_{NS}$ ,  $\Delta W_h$  and  $\Delta Po_h$  in percent at considered pressure ratios  $p_e/p_0$  and rarefaction parameter are shown in Fig. 15. In the slip regime ( $\delta \geq 50$ ) mass flow rates and  $Po$  obtained by hybrid, kinetic and NS solvers are close to each other: maximum difference between results is less than 2%. Starting from  $\delta = 20$  the difference becomes noticeable and larger than 5%. Further, when rarefaction increases  $\delta > 20$  the difference increases and reaches 10-14% at  $\delta = 10$ .

When gradients of macroparameters become higher the local Knudsen number increases, thus, at the same given rarefaction parameter  $\delta$ , we can have higher local Knudsen (higher rarefaction level) for higher pressure ratio. For example, for  $\delta = 10$  the difference between NS and kinetic results is around 10% for pressure ratio  $p_e/p_0 = 0.5$ , but increases to 12% and 14% at  $p_e/p_0 = 0.33$  and  $p_e/p_0 = 0.1$ , respectively. On the other hand, the hybrid solver successfully

reproduces mass flow rate  $W$  and  $Po$  number close to kinetic data (difference within 1% and 2%, respectively).

**Table 4.** Comparison of mass flow rate  $W$  and Poiseuille number  $Po$  computed by different methods at  $p_e/p_0$  varies from 0.1 to 0.9 and  $\delta$  from 100 to 10.

$p_e/p_0$	$\delta$	$W_h$	$Po_h$	$W_S$	$Po_s$	$W_{NS}$	$Po_{NS}$
0.1	100	0.81	137.6	0.81	137.82	0.81	136.58
	50	0.604	102.3	0.604	102.31	0.603	103.7
	40	0.540	93.68	0.543	93.09	0.536	94.96
	30	0.470	82.9	0.472	82.34	0.457	84.8
	20	0.383	68.67	0.383	68.17	0.359	71.89
	15	0.333	59.5	0.333	58.81	0.302	63.6
	10	0.280	47.15	0.282	46.2	0.239	52.5
0.33	100	0.788	129.3	0.783	129.14	0.790	129.48
	50	0.573	97.43	0.570	96.76	0.574	98.36
	40	0.507	89.64	0.505	88.9	0.5	90.9
	30	0.426	80.48	0.427	79.82	0.419	82.44
	20	0.332	68.88	0.335	68.2	0.319	71.86
	15	0.285	61	0.285	60.1	0.263	64.69
	10	0.23	50	0.232	49	0.203	54.64
0.5	100	0.72	116.2	0.718	116.2	0.724	116.2
	50	0.502	92.47	0.50	91.6	0.503	93
	40	0.44	87.07	0.439	86.3	0.441	88
	30	0.362	79.4	0.361	78.9	0.358	81.2
	20	0.278	69.6	0.277	69.04	0.266	72.44
	15	0.232	62.67	0.231	61.76	0.217	65.93
	10	0.184	52.3	0.185	51.3	0.166	56.52
0.9	100	0.257	92.6	0.254	92	0.257	92.6
	50	0.143	86	0.141	85.92	0.143	86.65
	40	0.116	83.1	0.115	82.95	0.116	84
	30	0.091	79.4	0.091	78.95	0.091	80.89
	20	0.065	72.68	0.067	71.88	0.065	74.81
	15	0.053	66.9	0.055	66.1	0.052	69.34
	10	0.039	57.2	0.043	56.5	0.04	61.2

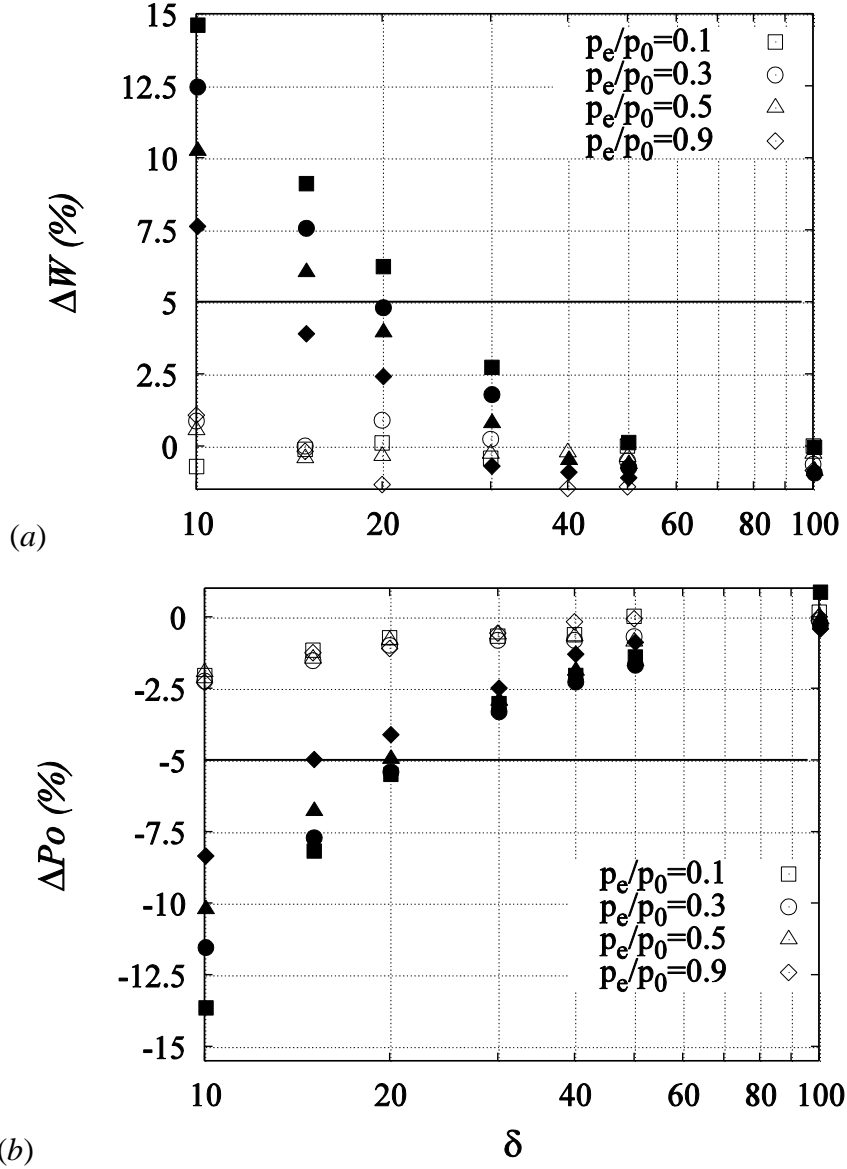


**Fig. 15.**  $\Delta(W, P_o)_{NS}$  (solid symbols) and  $\Delta(W, P_o)_h$  (empty symbols) via  $\delta$  at different  $p_e/p_0$ .

Profiles of dimensionless density, temperature, normalized by inlet values, and velocity along the symmetry axis  $y = 0$  are shown in Fig. 16 for  $p_e/p_0 = 0.1$  and  $\delta = 20$ ; in Fig. 17 for  $p_e/p_0 = 0.33$  and  $\delta = 15$ ; in Fig. 18 for  $p_e/p_0 = 0.5$  and  $\delta = 10$ . The combination of  $p_e/p_0$  and  $\delta$  for each case was chosen in order to demonstrate noticeable difference between NS and hybrid solutions.

Density (or pressure) variations are qualitatively similar in all cases. Before and after the channel the density tends to upstream and downstream conditions, while decreasing in the channel (see Figs. 16-18 a).

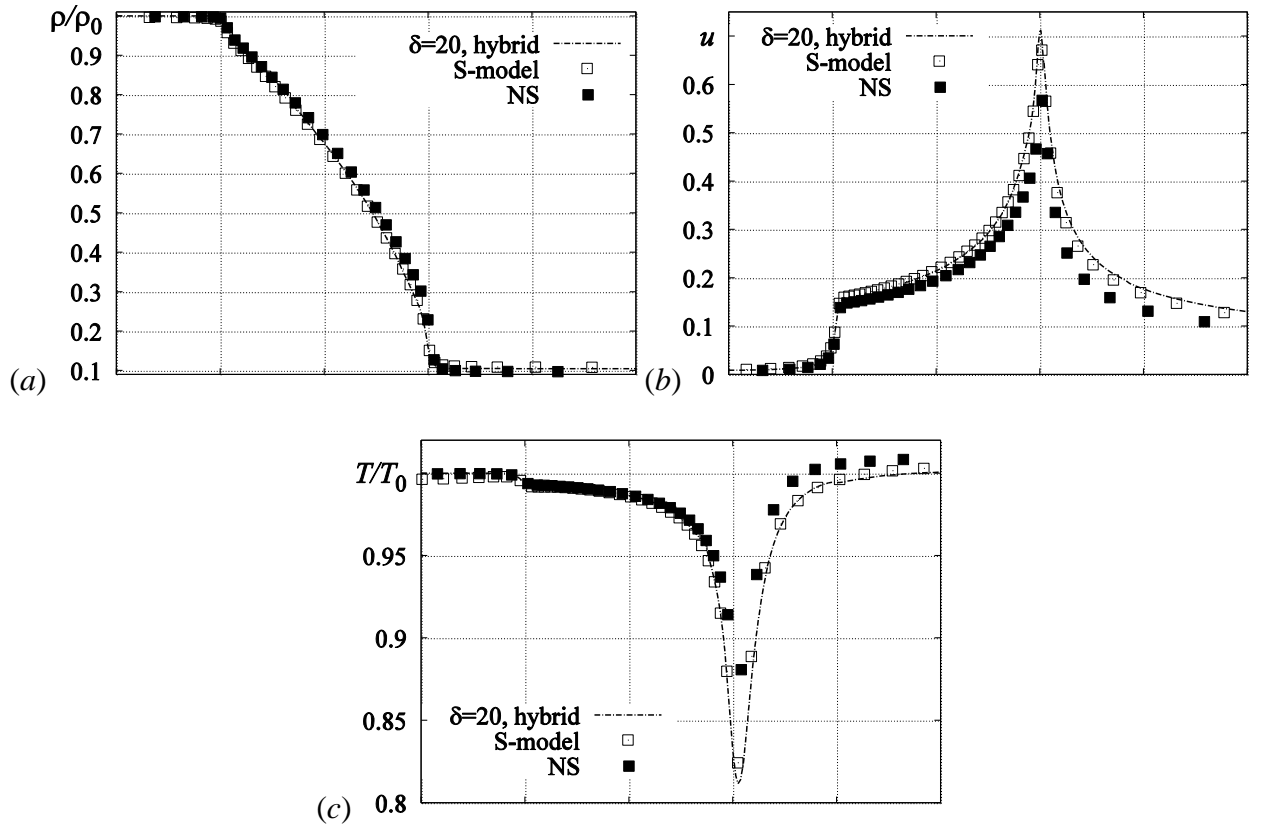


**Fig. 16.** (a): density  $\rho/\rho_0$ ; (b): axial velocity  $u$ ; (c): temperature  $T/T_0$  along the symmetry line

$$y = 0, p_e/p_0 = 0.1, \delta = 20.$$

At high pressure ratio the density profile is nonlinear. As can be seen in Figs. 16-18 *b* the axial velocity tends to zero in large reservoirs, while growing along the channel reaches the maximum value near the channel exit. Accordingly, the temperature decreases through the channel, while in the low velocity reservoirs it approaches to the reference temperature (see Figs. 16-18 *c*). The maximum variations of macroparameters appear for the lowest pressure ratio  $p_e/p_0 = 0.1$  (Fig. 16). The hybrid solutions are close enough to the kinetic ones for all values of rarefaction and pressure ratios, while NS equations do not give appropriate solution especially for velocity and temperature.

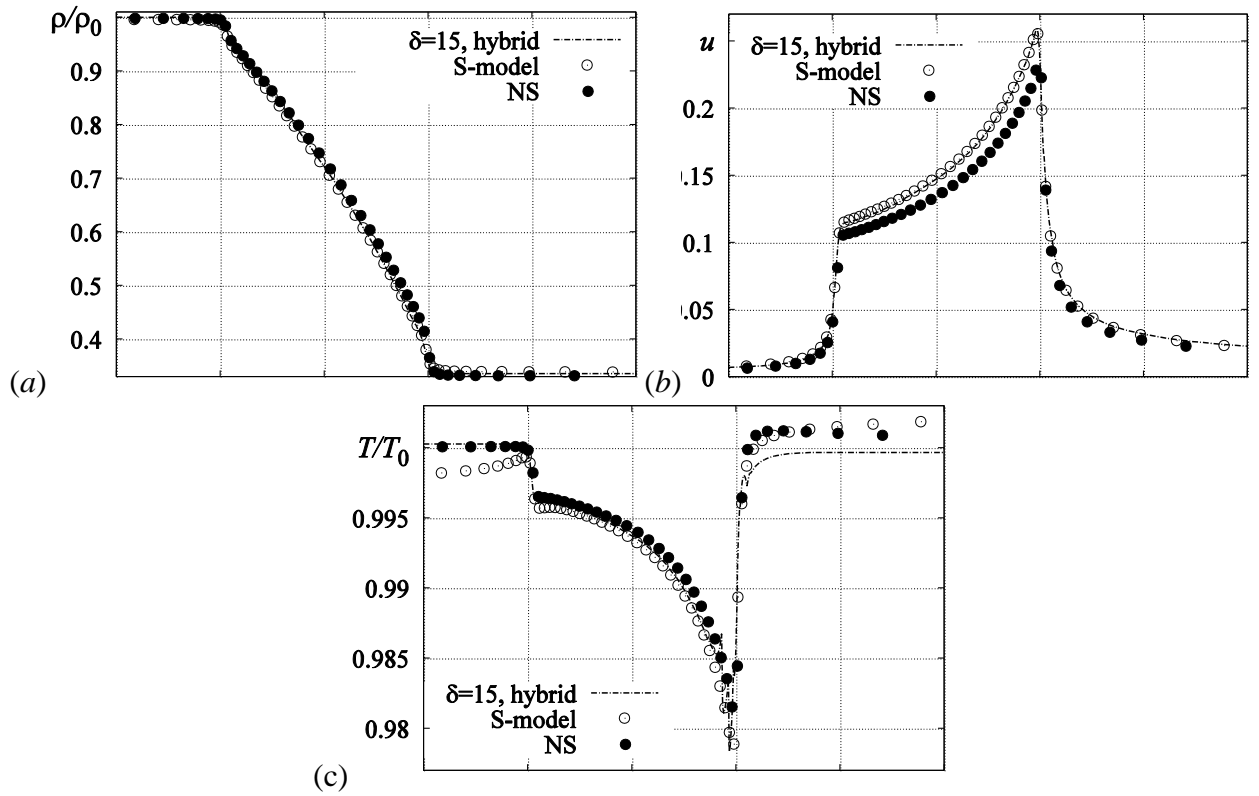


**Fig. 17.** (a): density  $\rho/\rho_0$ ; (b): axial velocity  $u$ ; (c): temperature  $T/T_0$  along the symmetry line  $y = 0$ ,  $p_e/p_0 = 0.33$ ,  $\delta = 15$ .

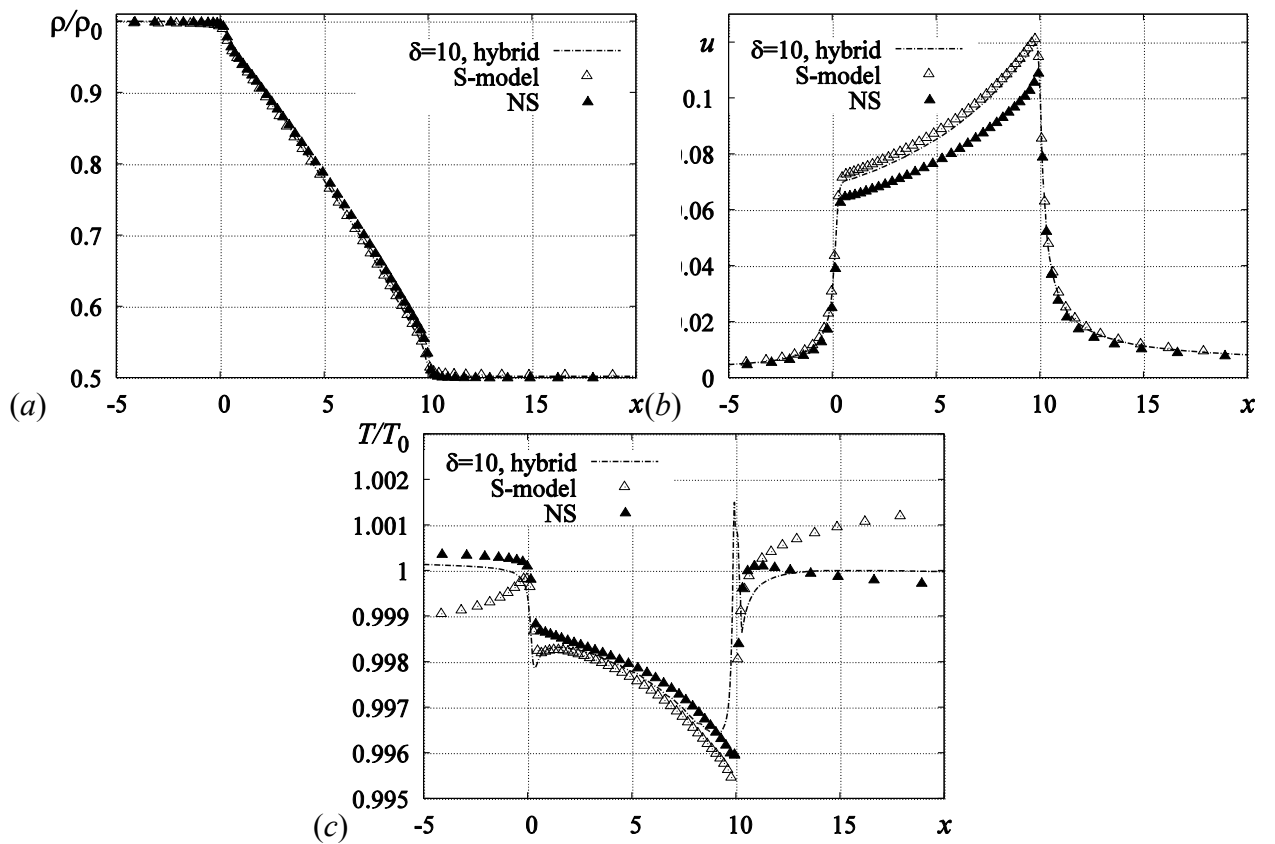


**Fig. 18.** (a): density  $\rho/\rho_0$ ; (b): axial velocity  $u$ ; (c): temperature  $T/T_0$  along the symmetry line  $y = 0$ ,  $p_e/p_0 = 0.5$ ,  $\delta = 10$ .

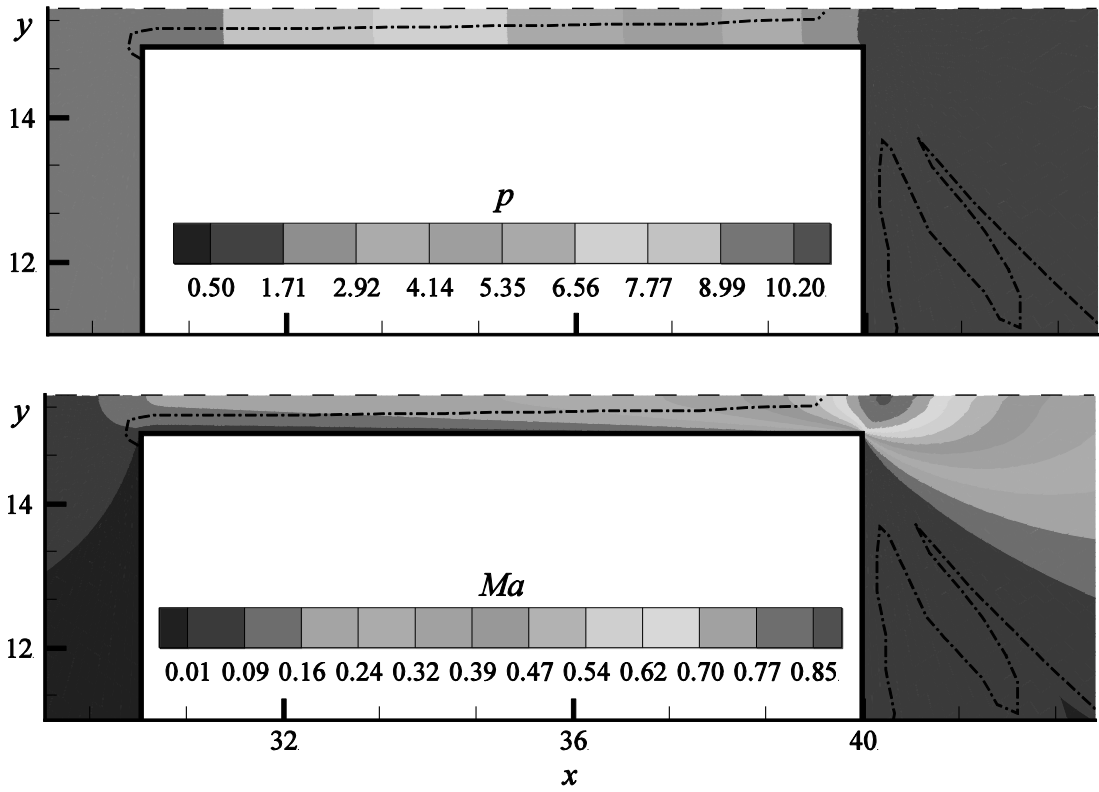


Fig. 19. Dimensionless pressure (top) and Mach number (bottom) contours at  $\delta = 20$  and  $p_e/p_0 = 0.1$ ; dashed dotted line shows interface  $I_c$  at convergence.

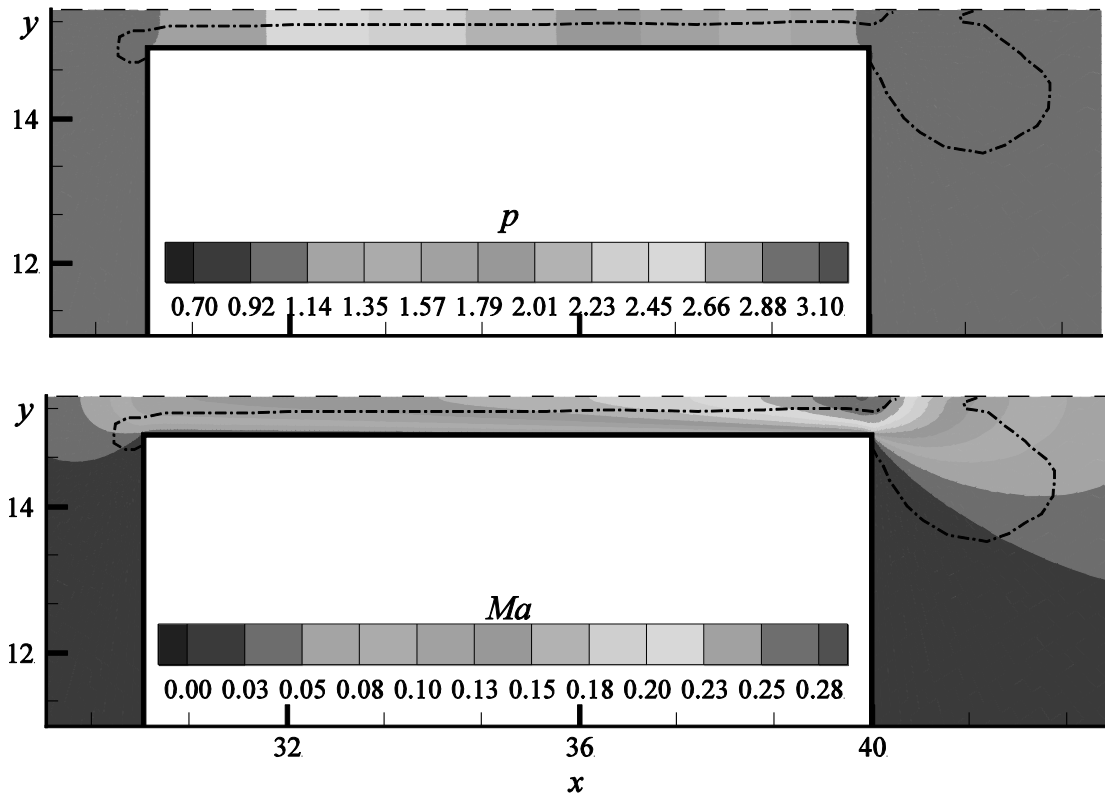
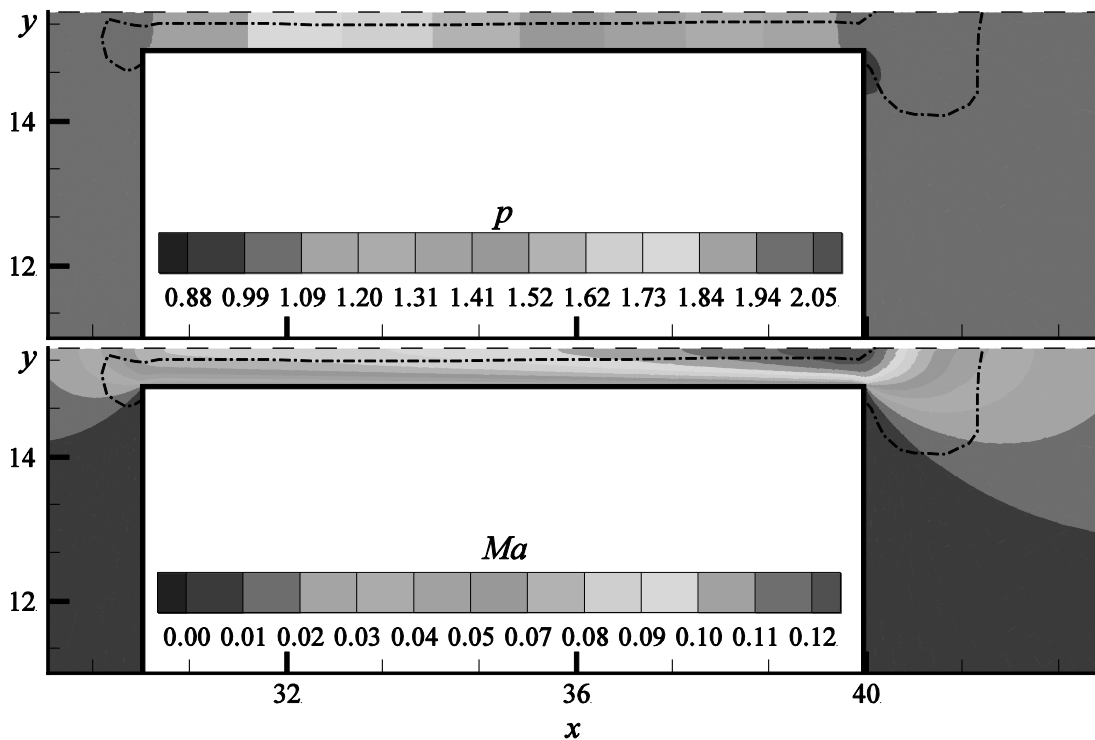


Fig. 20. Dimensionless pressure (top) and Mach number (bottom) contours at  $\delta = 15$  and  $p_e/p_0 = 0.33$ ; dashed dotted line shows interface  $I_c$  at convergence.

Contour lines of pressure and Mach number along the channel for different rarefaction are presented in Figs. 19-21, together with the extension of the kinetic region at convergence. It is also interesting to note the local  $Kn$  levels along the interface  $I_c$ . For low rarefaction  $\delta = 20$  (Fig. 19), but lowest pressure ratio 0.1, the local  $Kn$  near the coupling boundary  $I_c$  (dashed dotted line) varies from 0.045 at the inlet of the channel to 0.14. Under the same condition maximum local  $Kn$  is 0.5 at the exit of the channel. For higher rarefaction  $\delta = 15$  and  $p_e/p_0 = 0.33$ , Fig. 20, the local Knudsen number near the coupling boundary varies from 0.06 to 0.16, while the maximum local  $Kn$  occurs at the exit is equal to 0.2.



**Fig. 21.** Dimensionless pressure (top) and Mach number (bottom) contours at  $\delta = 10$  and  $p_e/p_0 = 0.5$ ; dashed dotted line shows interface  $I_c$  at convergence.

For the smaller rarefaction parameter value,  $\delta = 10$ , and higher  $p_e/p_0 = 0.5$ , shown in Fig. 21, the local Knudsen near the boundary is slightly higher, varying from 0.092 to 0.17, and its maximum value is 0.19 near the exit. Thus, as might be expected, for all of these configurations the interface is always located roughly at the same level of  $Kn$ , despite large variation of  $Kn$  in the core flow region. The coupling between kinetic and NS solutions shows a

smooth transition along the contour lines crossing the domains interface for both Mach number and pressure contours.

As was written in previous section the CPU time per time step of hybrid code  $t_h$  is the sum of the time required for the solution of the S-model equation in  $N_K$  kinetic points ( $N_K$  is estimated from converged hybrid solution), of NS equations and the coupling procedures. Since the sum of CPU times relative to NS solution and coupling computation is quite small in comparison to the kinetic solution requirements, time  $t_h$  is essentially dictated by the number of  $N_K$  kinetic points to be solved during computation. Figure 22 shows a hybrid code speedup compared to the pure kinetic S-model code as a function of rarefaction parameter. The hybrid code offers a CPU time speedup ranging from 2, at a rarefaction level, where NS solution would be completely inadequate, up to 5 in the slip flow regime. For example, pure kinetic computation at  $p_e/p_0 = 0.1$  and  $\delta = 20$  on physical mesh of  $360 \times 40$  and velocity mesh of  $40 \times 40$  requires 2.51 s, while hybrid time step  $t_h$  is 1.3 s (number of kinetic points  $N_K = 7050$ ) and the NS step is  $t_{NS} = 0.14$  s. The total CPU advantage over the whole computation, with the dynamic coupling, is however appreciably greater, since at the beginning of the computation the kinetic area is typically much smaller than at converged state. It can be seen in Fig. 22 that with a decrease in  $\delta$  the speedup decreases, since the number of kinetic points in  $\Omega_K$  increases.

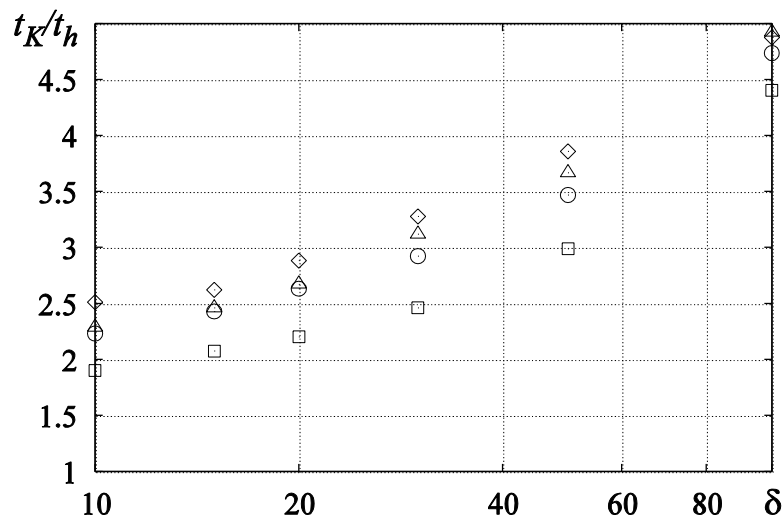


**Fig. 22.** Speedup for hybrid simulations:  $\square$  -  $p_e/p_0 = 0.1$ ;  $\circ$  -  $p_e/p_0 = 0.33$ ;  $\Delta$  -  $p_e/p_0 = 0.5$ ;  $\diamond$  -  $p_e/p_0 = 0.9$ .

Furthermore, additional advantage of the hybrid solver is reached by decreasing the size of inlet/outlet reservoirs in comparison with requirement for the pure kinetic solver. This allows quicker convergence in the inlet/outlet reservoirs for NS solver.

#### 5.4.2. Flow over a rough surface

As shown in the previous section the best choice of breakdown parameter for the near-wall modelling is the modified gradient length Knudsen number  $Kn_{GL}(x, y)$  (eq. (16)). Moreover, the hybrid solver produced reliable results with acceptable level of accuracy if the kinetic solution was activated for physical space points satisfied the condition  $Kn_{GL}(x, y) \geq 0.1$ .

**Table 5.** Comparison of dimensionless global mass flow rate  $W$  computed by different methods at  $p_e/p_0$  varies from 0.33 to 0.9 and  $\delta$  from 100 to 10.

$\varepsilon$		5%		2.5%		1.25%		smooth	
$p_e/p_0$	$\delta$	$W_{NS}$	$W_h$	$W_{NS}$	$W_h$	$W_{NS}$	$W_h$	$W_{NS}$	$W_h$
0.33	100	0.752	0.764	0.770	0.783	0.781	0.792	0.797	0.801
	50	0.524	0.546	0.538	0.560	0.544	0.568	0.568	0.575
	40	0.456	0.480	0.465	0.492	0.473	0.500	0.498	0.505
	30	0.368	0.398	0.378	0.409	0.385	0.416	0.412	0.422
	20	0.272	0.302	0.277	0.312	0.283	0.319	0.313	0.324
0.5	100	0.700	0.708	0.718	0.725	0.725	0.734	0.740	0.743
	50	0.467	0.484	0.480	0.497	0.486	0.504	0.504	0.509
	40	0.400	0.420	0.407	0.430	0.416	0.436	0.434	0.438
	30	0.319	0.340	0.328	0.350	0.332	0.354	0.412	0.420
	20	0.228	0.252	0.236	0.260	0.239	0.265	0.261	0.268
	10	0.131	0.160	0.132	0.161	0.137	0.167	0.163	0.180
0.9	100	0.241	0.243	0.248	0.250	0.252	0.253	0.257	0.257
	50	0.130	0.132	0.135	0.137	0.137	0.139	0.143	0.143
	40	0.1067	0.1096	0.110	0.113	0.111	0.114	0.116	0.117
	30	0.0824	0.0854	0.0849	0.0881	0.086	0.0895	0.091	0.092
	20	0.0577	0.0614	0.0594	0.0636	0.060	0.065	0.0652	0.0675
	10	0.0322	0.0369	0.0332	0.0386	0.0337	0.0395	0.0390	0.0421

It should be noticed that a global Poiseuille number  $Po$  is computed over the rough section, skipping small regions both at the inlet and exit of section in order to avoid entrance and exit effects. Hence, the actual length of a rough sector using in computations of global Poiseuille number is  $L^* = 2.25$  (see Fig. 13) and includes 9, 18 and 42 rough modules, for  $\varepsilon = 5\%$ ,  $\varepsilon = 2.5\%$  and  $\varepsilon = 1.25\%$ , respectively. For the smooth channel flow global  $Po$  number is estimated over the same section of length  $L^* = 2.25$ .

**Table 6.** Comparison of global Poiseuille number  $Po$  computed by different methods at  $p_e/p_0$  varies from 0.33 to 0.9 and  $\delta$  from 100 to 10.

$p_e/p_0$	$\delta$	$\varepsilon = 5\%$		$\varepsilon = 2.5\%$		$\varepsilon = 1.25\%$		smooth	
		$Po_{NS}$	$Po_h$	$Po_{NS}$	$Po_h$	$Po_{NS}$	$Po_h$	$Po_{NS}$	$Po_h$
0.33	100	207	199.67	188.13	180	176.5	168.62	158.4	158.4
	50	144.87	129.81	132.68	118.74	126.4	111.73	105.63	104.44
	40	130.57	113.42	121.54	104	114.73	97.3	93.6	91.95
	30	120.06	97.43	110.96	89.2	104.8	83.48	80.98	78.27
	20	109.14	80.50	102.15	73.7	96.76	68.72	67	62.9
0.5	100	167.78	161.8	150.7	145.04	141.64	135.78	128	128
	50	128.55	116.5	117.67	106.5	111.78	99.45	95.95	93.94
	40	120.15	105.93	110.19	96.83	104.96	90.7	88.3	86.17
	30	113.67	95.55	104.37	87.36	99.7	81.68	79.88	77
	20	107.82	83.0	99.35	75.69	95.31	70.6	69.38	65.97
10	102.18	61.73	95.22	56.34	91.62	52.52	52	47.63	
0.9	100	115.64	113.2	104.49	102.35	98.42	95.84	92.3	92
	50	112.48	106.39	101.76	95.42	95.76	90.71	86.65	85.98
	40	109.93	102.16	100.44	92.9	95.15	87.89	84	83.1
	30	108.57	98.03	99.24	89.66	94.96	84.3	80.89	79.4
	20	106.73	90.77	97.76	83.55	93.65	78.8	74.81	72.68
10	103.7	72.6	95.61	65.5	92.42	62.5	61.2	57.2	

In Table 5 and 6 dimensionless global mass flow rate  $W$  and Poiseuille number  $Po$ , respectively, computed using continuum NS equations and hybrid solver are given for the pressure ratio of 0.33, 0.5 and 0.9 and rarefaction parameter  $\delta$  ranging from 10 to 100 and relative roughness  $\varepsilon = 5\%$ ,  $\varepsilon = 2.5\%$ ,  $\varepsilon = 1.25\%$  and  $\varepsilon = 0$  (smooth channel).

According Table 5 and 6 for fixed pressure ratio a mass flow rate and Poiseuille number reach their maximum values at weakly rarefied flow ( $\delta = 100$ ) and minimum at highly rarefied one ( $\delta = 10$  or 20). Opposite tendency can be observed for Poiseuille number and mass flow rate with variation of relative roughness height: Po number decreases when relative roughness height tends to 0, due to decrease of friction effect of the wall, while mass flow rate increases. The increase of rarefaction ( $\delta$  decrease), on the other hand, decreases the values of Po number and mass flow rates. The competition between roughness, rarefaction and compressibility effect will be discussed in details lately.

### *Comparison of hybrid solution with other methods*

In order to neglect compressibility effect and keep only rarefaction one a series of computations have been carried out at high pressure ratio  $p_e/p_0 = 0.9$  and rarefaction parameter  $\delta$  from 100 to 10. Measuring pressures at the entrance  $p'_i$  and at the exit  $p'_e$  of the rough section  $L^* = 2.25$  we have even higher pressure ratio  $p'_e/p'_i = 0.96$ . Such high pressure ratio allows to investigate a nearly incompressible flow condition while varying the rarefaction level. Additional local rarefaction parameter, exit Knudsen number  $Kn_e$ , based on the exit of rough section mean free path and channel height  $H$  can be computed as:

$$Kn_e = \frac{\lambda_e}{H} = \frac{32}{5} \sqrt{\frac{\gamma}{2\pi}} \frac{Ma_e}{Re_e} \quad (96)$$

and varies from 0.01 to 0.1 (slip regime).

In Fig. 23 comparison of hybrid and NS computed global Poiseuille number with pure kinetic S-model results from [72] for highest relative roughness height  $\varepsilon = 5\%$  and smooth channel is shown. It should be noticed that S-model Poiseuille numbers were recomputed according to the non dimensionalization defined in the present work, which introduces around 6.53% difference from the results presented in [72]. As can be seen, hybrid and kinetic computed Po numbers are in a good agreement for both rough and smooth channels and decrease with

Knudsen number increase (rarefaction effect). Thus, the hybrid solver can be considered as a reliable solver for further computations. At the same time NS solver significantly overestimates  $Po$  for rough wall channel flow, while for smooth channel produces data in a good agreement with both pure kinetic and hybrid solvers.

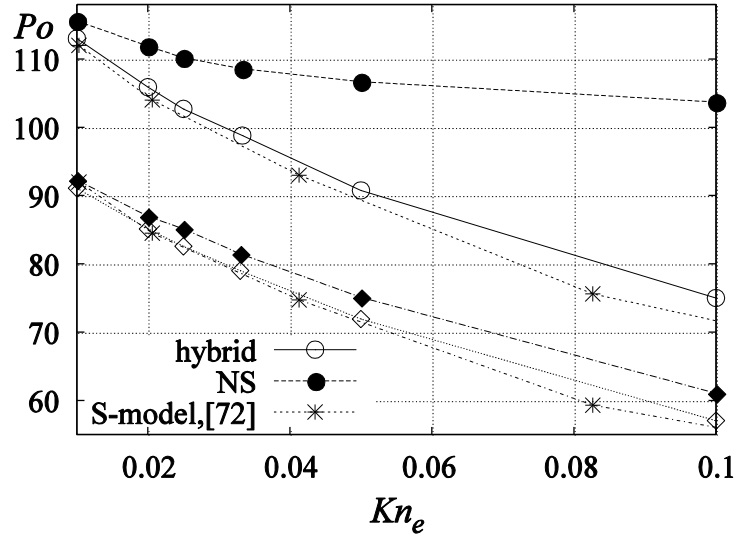


**Fig. 23.** Global Poiseuille number  $Po$  via exit Knudsen number  $Kn_e$  for relative roughness  $\varepsilon = 5\%$  (circles) and smooth  $\varepsilon = 0$  (diamonds):  $p_e/p_0 = 0.9$

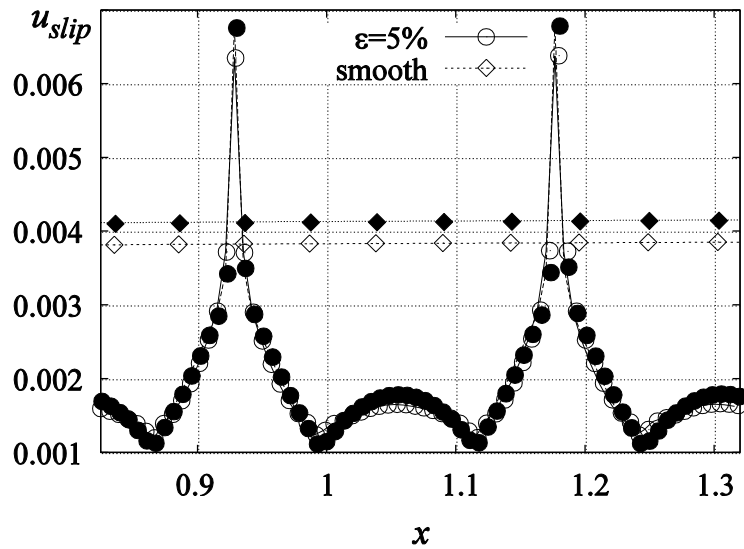


**Fig. 24.** Slip velocity  $u_{slip}$  for relative roughness  $\varepsilon = 5\%$  and smooth  $\varepsilon = 0$ : NS, solid symbols; hybrid, empty symbols;

Moreover, as can be seen in Fig. 23, a rough surface Poiseuille number is significantly larger than for smooth one. Indeed, looking at slip velocities distribution over rough and smooth

surface, presented in Fig. 24, it can be seen that a slip velocity reaches its maximum around the rough peak and forms minimum “velocity plateau” in the region between peaks, while smooth surface slip velocity in the same region is constant and is larger than the average rough surface channel slip velocity.

In order to quantitatively estimate the applicability of NS solver coupled with the slip boundary condition for near incompressible flow regime the relative difference between NS and hybrid solutions in terms of global mass flow rate  $W$  and Poiseuille number  $Po$  is computed as following:

$$\Delta(W, Po)_{h-NS} = 1 - \frac{(W, Po)_{NS}}{(W, Po)_h}, \quad (97)$$

The relative differences  $\Delta W_{h-NS}$  and  $\Delta Po_{h-NS}$  in percent are shown in Fig. 25 for relative roughness height  $\varepsilon$  of zero (smooth channel), 1.25%, 2.5% and 5%. In case the flow through the rough surface channel we have a larger difference between NS and hybrid solutions in terms of Poiseuille number than in mass flow rate, probably, due to the additional dependence of Poiseuille number on not only density and velocity, but also viscosity (see eq. (90)). It should be noticed that for the flow through the smooth channel even for a highly rarefied condition ( $Kn_e = 0.1$ ) the relative difference between NS and hybrid solutions does not exceed 5-7% for both mass flow rate  $W$  and Poiseuille number  $Po$ . On the other hand, when the surface roughness is taken into consideration the Poiseuille number difference between NS and hybrid solutions  $\Delta Po_{h-NS}$  already exceeds 5% for a relatively low rarefaction,  $Kn_e \approx 0.02$  ( $\delta = 50$ ), and reaches around 48% for highest  $Kn_e = 0.1$  ( $\delta = 10$ ). For mass flow rate difference  $\Delta W_{h-NS}$  the critical  $Kn_e$  when the difference becomes larger than 5% is higher, around 0.04, while the maximum  $\Delta W_{h-NS}$  is smaller and equal to 14.5% for  $Kn_e = 0.1$ . It should be noticed that both mass flow rate and Po number differences show only weak dependence on the value of relative roughness  $\varepsilon$ , but a strong dependence on the rarefaction level, i.e. Knudsen number (or  $\delta$ ). In particular, for a relatively low rarefaction level,  $Kn_e = 0.02$  ( $\delta = 50$ ) the mass flow difference  $\Delta W_{h-NS}$  is around

2% and  $\Delta P_{O_{h-NS}}$  varies from 4.7% to 8% when the relative roughness  $\varepsilon$  decreases from 5% to 1.25%. On the other hand, for higher rarefaction,  $Kn_e = 0.1$  ( $\delta = 10$ ), at the same values of roughness the mass flow difference  $\Delta W_{h-NS}$  increases to 12.5% and 14.5%, and  $Po$  number difference  $\Delta P_{O_{h-NS}}$  from 45.5% to 48%.

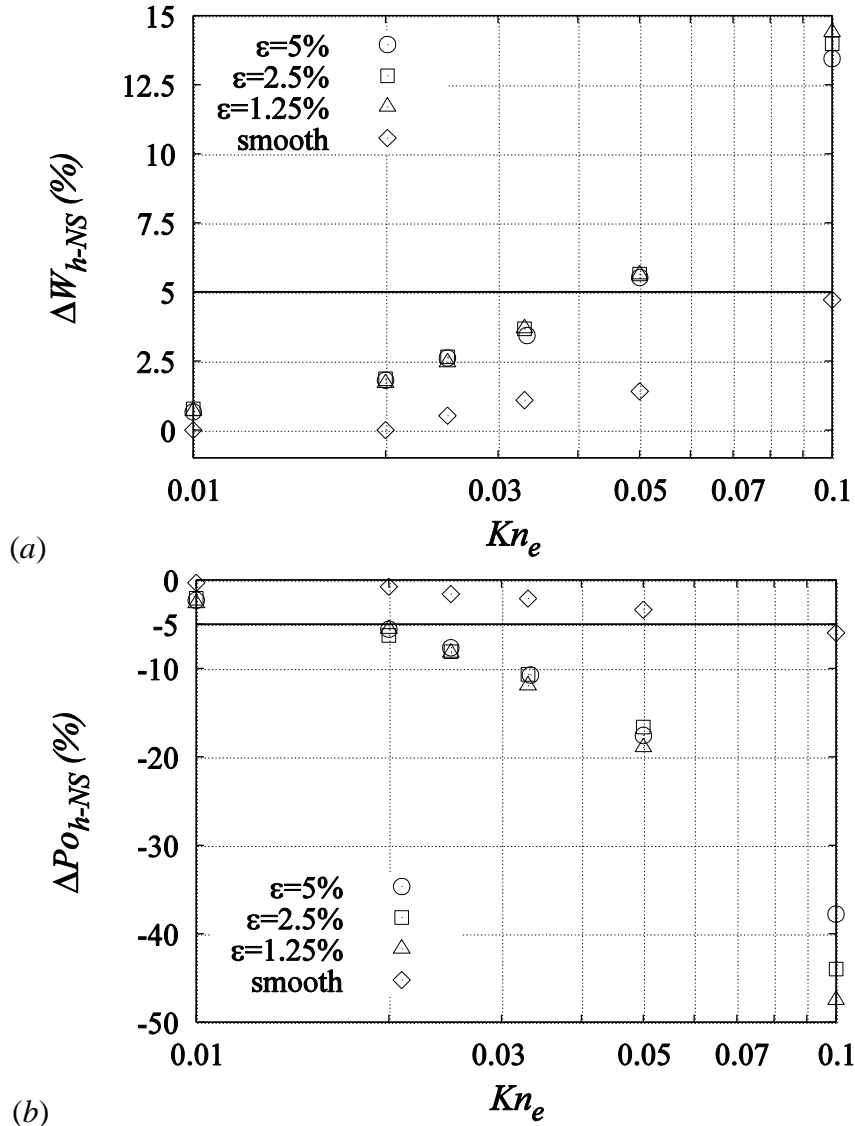


**Fig. 25.**  $\Delta(W, Po)_{h-NS}$  via exit Knudsen number  $Kn_e$  at  $p_e/p_0 = 0.9$ .

Thus, it can be concluded that the widely used first-order slip boundary condition can not properly describe the flow behaviour in the vicinity of rough surface even when a flow, in general, could be considered as weakly rarefied one in terms of the Knudsen based on the height of the channel (or the hydraulic diameter, which has the same order of magnitude). In fact, NS equations coupled with slip condition produces reasonably good results for smooth surface flow

up to exit  $Kn = 0.1$ , but their accuracy for rough channel is already questionable above exit  $Kn = 0.02-0.03$ .

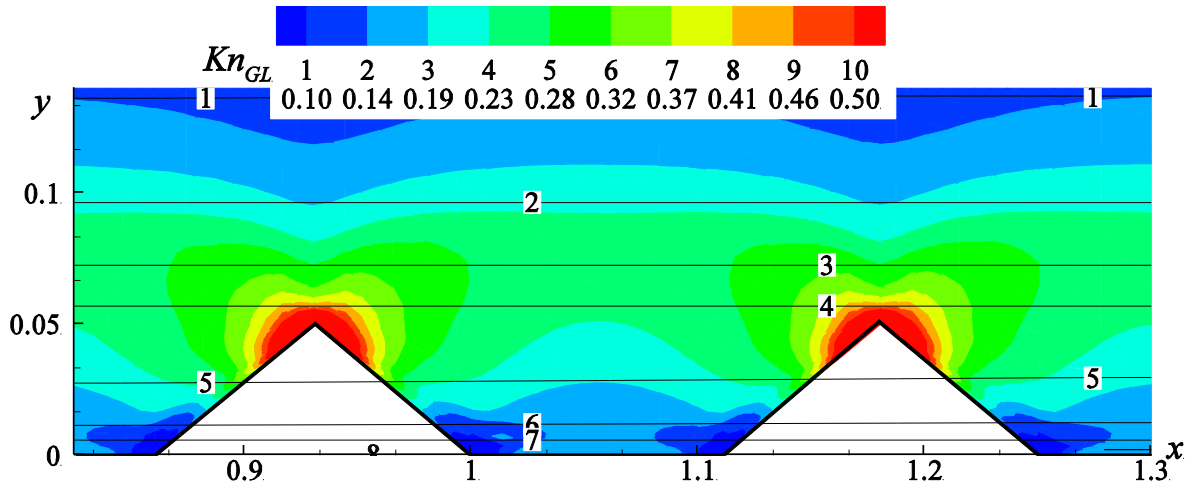


**Fig. 26.**  $Kn_{GL}$  for  $\varepsilon = 5\%$  (flood) and  $\varepsilon = 0\%$  (black contour lines),  $Kn_e = 0.02$  ( $\delta = 50$ ).

To clarify such inconsistency let us consider the flow details in terms of local gradient Knudsen number  $Kn_{GL}$  map in the vicinity of rough region shown in Fig. 26. A highly rarefied local regions appears near the top of the rough surface elements, with higher values in comparison with smooth surface  $Kn_{GL}$  ones (black contour lines). When a small peak size is of the order of the local mean free path molecules may just skip peaks and the global effect of the rough wall in comparison with the smooth one is reduced. Moreover, as indicated in [11, 59] for the smooth surface channel this is consistent with the low values of the  $H$  based Knudsen number, falling within the slip flow regime, while the details of the flow (i.e., local Knudsen number) around the smaller scale roughness elements may exceed these limits.

### *Comparison of hybrid solution with literature results*

It is interesting to compare hybrid solution with literature available results. In Fig. 27 the distribution of global rough Poiseuille number  $Po_\varepsilon$  as a function of the local exit Knudsen number  $Kn_e$  is presented for different relative roughness heights  $\varepsilon$  and compared with analytical expression for the Poiseuille number eq. (92) and a correlation based on Lattice Boltzmann

results [65], eq. (93) with  $\varepsilon = 5\%$ . It can be seen that smooth surface channel Po number demonstrates good agreement with an analytic expression eq. (92) up to  $Kn_e = 0.05$ , while Po number for rough surface channel with  $\varepsilon = 5\%$  slightly deviates from correlation eq. (93), probably due to the different obstacle geometry using in [65].

As expected, the increase of the height of wall roughness elements results in an increase of Poiseuille number in comparison with the smooth one due to increase of wall friction effect. On the other hand, the increase of rarefaction significantly affects the Poiseuille number. Although the Poiseuille number for each Knudsen number increases as the relative roughness  $\varepsilon$  increases, the value of Poiseuille number is larger at lower Knudsen number and decreases as  $Kn_e$  increases (see also Table 5).

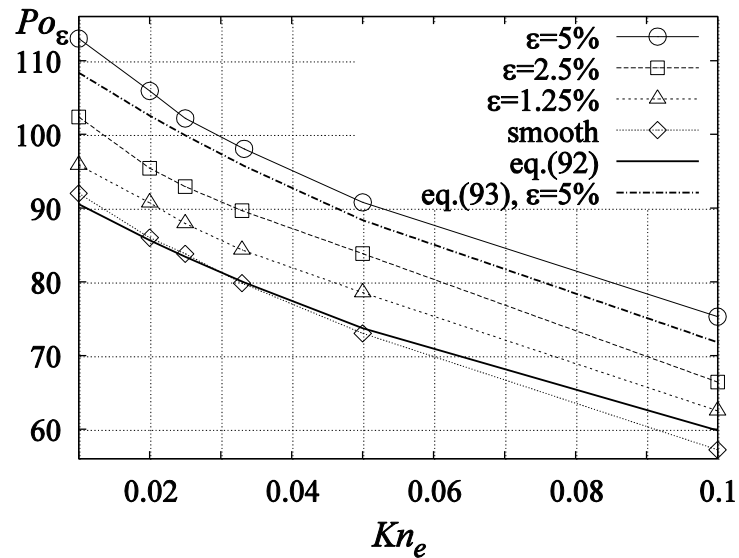


**Fig. 27.**  $Po_{\varepsilon}$  via exit Knudsen number  $Kn_e$  for different relative roughness  $\varepsilon$ .

In particular, for  $\varepsilon = 5\%$  the highest  $Po_{\varepsilon} = 112$  is for lowest  $Kn_e = 0.01$  and the lowest  $Po_{\varepsilon} = 72$  for highest  $Kn_e = 0.1$ . When the rarefaction increases the local mean free path of particles in the gas flow increases resulting in decrease of interactions between particles and hence, reduction of global  $Po$  number for both rough and smooth channel flows (see Fig. 27). The same decrease of  $Po_{\varepsilon}$  with Knudsen number increase has also been observed in [59, 63, 64, 72].

### *Roughness rarefaction competition*

Furthermore, it is interesting to estimate the competition of rarefaction and roughness effects via a deviation of rough surface Poiseuille number  $Po_\varepsilon$  (or mass flow rate  $W_\varepsilon$ ) from smooth one  $Po_s$  (or  $W_s$ ), which can be computed as following:

$$\Delta(W, Po)_{\varepsilon-s} = \frac{(W, Po)_\varepsilon}{(W, Po)_s} - 1 \quad (98)$$

In Fig. 28 deviations  $\Delta W_{\varepsilon-s}$  and  $\Delta Po_{\varepsilon-s}$  as a function of relative roughness height  $\varepsilon$  for different level of rarefaction is presented. For fixed rarefaction level ( $Kn$  number) when relative roughness  $\varepsilon$  decreases Poiseuille number  $Po_\varepsilon$  decreases, while a mass flow rate  $W_\varepsilon$  increases, and both tend to the smooth channel values. In particular, for  $Kn_e = 0.01$  the deviation  $\Delta Po_{\varepsilon-s}$  grows from 4.2% for  $\varepsilon = 1.25\%$  up to 23% for maximal relative wall roughness  $\varepsilon = 5\%$ , while for highest  $Kn_e = 0.1$  ranges from 9.3% to 29%, respectively. Thus, for fixed rarefaction level considered here the roughness of surface significantly increases  $Po$  number with respect to the smooth one. On the other hand, the hybrid computed mass flow rate deviations  $\Delta W_{\varepsilon-s}$  are significantly smaller: from 0.5% for  $\varepsilon = 1.25\%$  up to 4.2% for  $\varepsilon = 5\%$  when  $Kn_e = 0.01$  and from 6% to 11.6% when  $Kn_e = 0.1$ . This is due to the additional dependence of Poiseuille number (see eq. (90)) on viscosity.

It should be noticed that for the considered range of Knudsen number (slip regime) the deviation between rough and smooth surface Poiseuille number  $\Delta Po_{\varepsilon-s}$  is weakly dependent on Knudsen number in hybrid computations, despite the significant deviation between rough and smooth values that is reported by the continuum solution. Thus, even in these apparently low rarefied regimes, the continuum computation offers qualitatively misleading results.

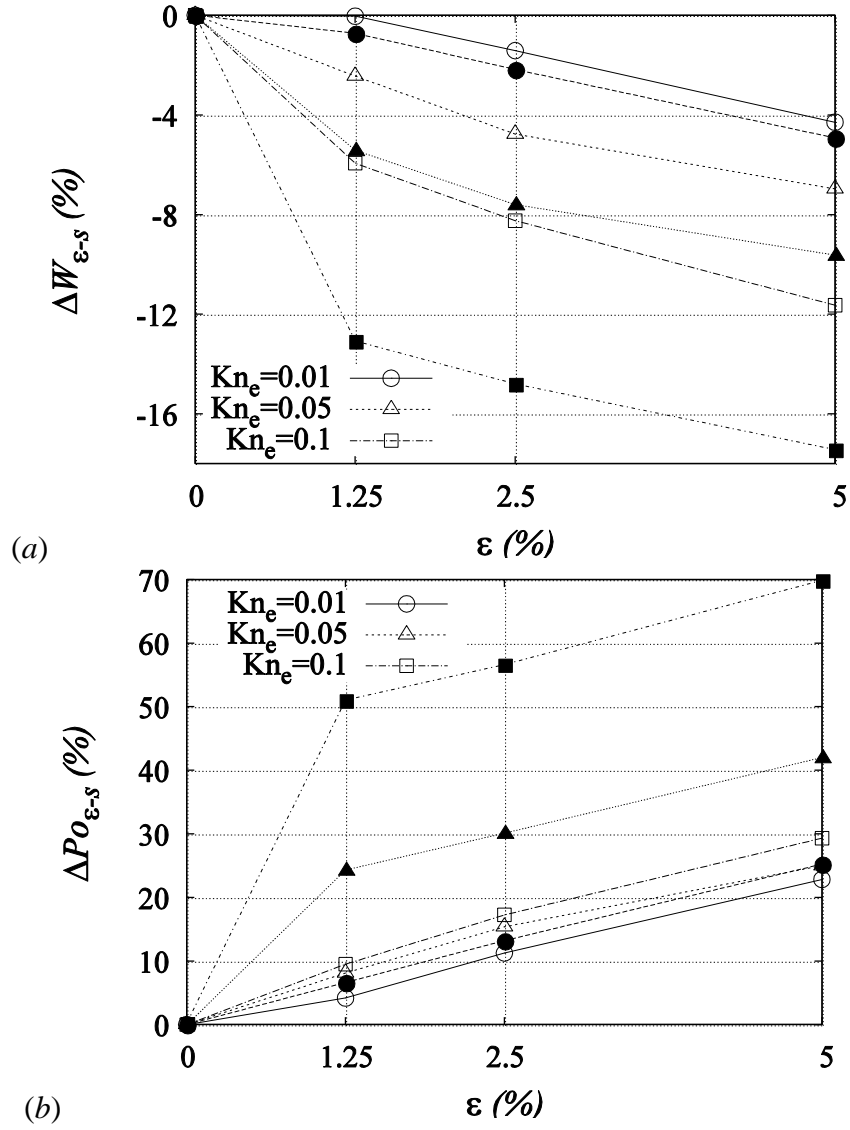


**Fig. 28.**  $\Delta W_{\varepsilon-s}$  and  $\Delta Po_{\varepsilon-s}$  via relative roughness  $\varepsilon$  at  $p_e/p_0 = 0.9$ : NS, solid symbols; hybrid, empty symbols.

Moreover, as can be seen in Fig. 28a, NS solver overestimates mass flow rate deviation  $\Delta W_{\varepsilon-s}$  as well, especially for high Knudsen number, although this overestimation is not so dramatical as for Poiseuille number: maximum  $\Delta W_{\varepsilon-s}$  for  $\varepsilon = 5\%$  and  $Kn_e = 0.1$  equals 17.4% while Poiseuille number deviation  $\Delta Po_{\varepsilon-s}$  is 70%.

In order to have a full picture and observe a larger rarefaction effect on the flow over a rough surface, the S-model results from [72] in terms of Poiseuille number deviation  $\Delta Po_{\varepsilon-s}$  for  $Kn_e$  up to 0.83 are shown in Fig. 29 along with hybrid and NS computed Po number deviations. As can be seen the deviation  $\Delta Po_{\varepsilon-s}$  of rough surface channel Poiseuille number (for  $\varepsilon = 5\%$ )

from smooth one increases with Knudsen number increase and reaches 42% for  $Kn_e = 0.83$ . Thus, the rarefaction enhances roughness effect; it can be more noticeable in transition regime for  $Kn > 0.1$ . Indeed, for highly rarefied region molecules interactions with a wall start playing more important role than collisions between molecules; therefore the gas flow becomes very sensitive to imperfection of the wall and hence a deviation of rough surface Po number from smooth value ( $\Delta Po_{\varepsilon-s}$ ) increases, while the Poiseuille number value (for both smooth and rough surface) decreases with  $Kn$  number increase.

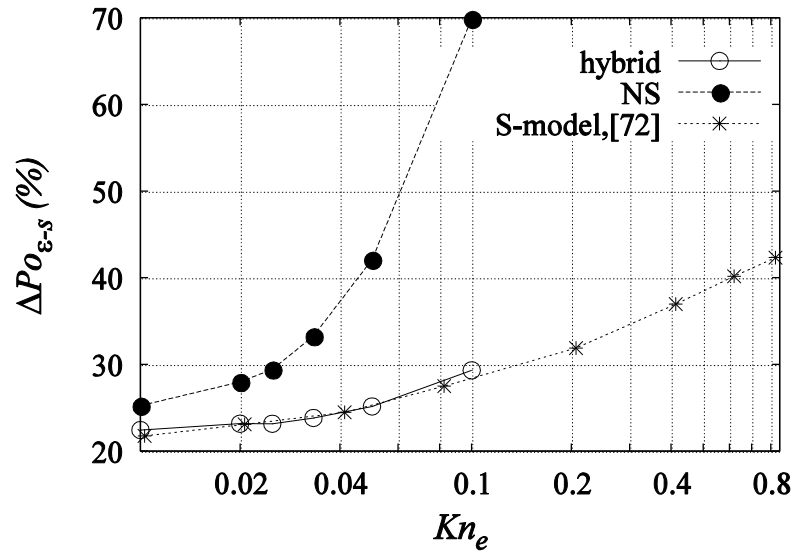


**Fig. 29.**  $\Delta Po_{s-\varepsilon}$  via exit Knudsen number  $Kn_e$  for  $\varepsilon = 5\%$ : NS, solid symbols; hybrid, empty symbols; S-model [72], stars

Moreover, as can be seen in Figs. 28 and 29, NS solver essentially overestimates the roughness effect in comparison with hybrid results already starting from exit  $Kn_e = 0.02$ , while in this case local Knudsen in the vicinity of rough peaks is 25 times higher (see Fig. 26). In particular, for  $Kn_e = 0.1$  ( $\delta = 10$ ) NS computed deviation  $\Delta Po_{\varepsilon-s}$  increases up to 70%, while for weakly rarefied gas  $Kn_e = 0.01$  ( $\delta = 100$ ) it is around 25% and close to the hybrid solver computed deviation.

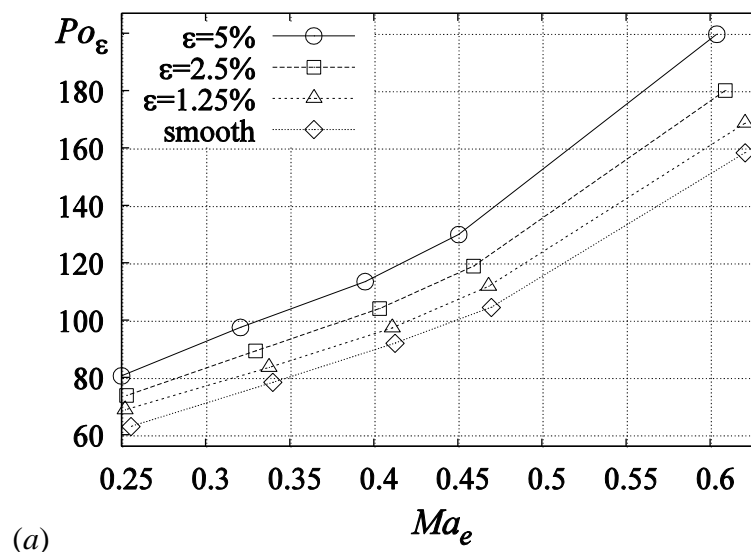
Further investigation of the different roughness geometries on flow field for highly rarefied flow is of great interest, but at this moment out of the scope of the present work. A similar behaviour was observed in computation of Cao et al. [64], considering the results for relative

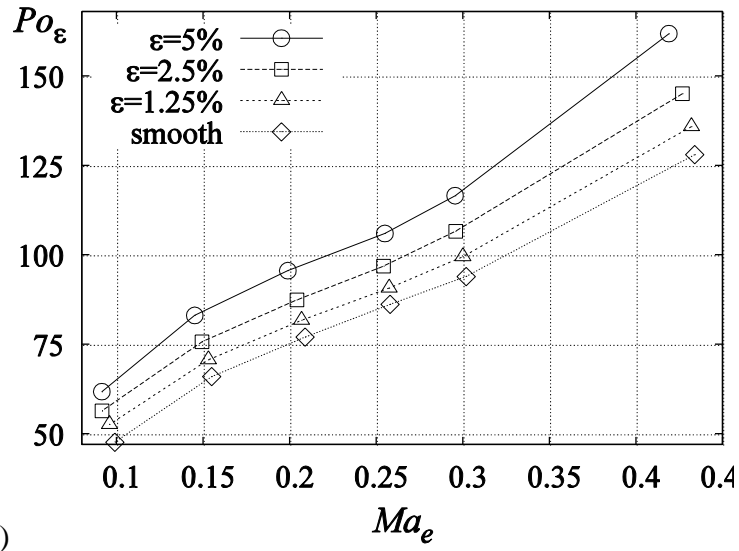
roughness height  $\varepsilon = 4.1\%$ , the Poiseuille number increase with respect to the smooth case at  $Kn = 0.6$  was much higher than that at  $Kn = 0.2$ .

It should be noticed that in the case of highly rarefied flow all channel is within Knudsen layer, i.e. the kinetic domain size for a hybrid solver becomes too larger, thus making an application of hybrid solver is not so interesting (in terms of computational efficiency) in comparison with pure kinetic one.

### *Compressibility effect*

The compressibility effect may play an important role in micro flows, thus it is interesting to take it into account in this analysis. Figures 28 shows the hybrid computed Poiseuille number  $Po_\varepsilon$  averaged over a whole rough sector of length  $L^* = 2.25$  as a function of exit averaged cross section Mach number  $Ma_e$  (computed at the end of rough sector  $L^*$ ) at pressure ratios  $p_e/p_0 = 0.33$  and 0.5, respectively. As can be seen Poiseuille number  $Po_\varepsilon$  growth with  $Ma_e$  increase from nearly incompressible flow ( $Ma_e = 0.1$ ) up to choked flow ( $Ma_e = 0.62$ ). The maximum variation of  $Po_\varepsilon$  due to the roughness effect, i.e. increase of relative roughness height, is around 27% (for  $Ma_e \approx 0.61$ ) while the variation of  $Po_\varepsilon$  due to increase of  $Ma_e$  (from 0.25 to 0.61) is almost 2.5 times.

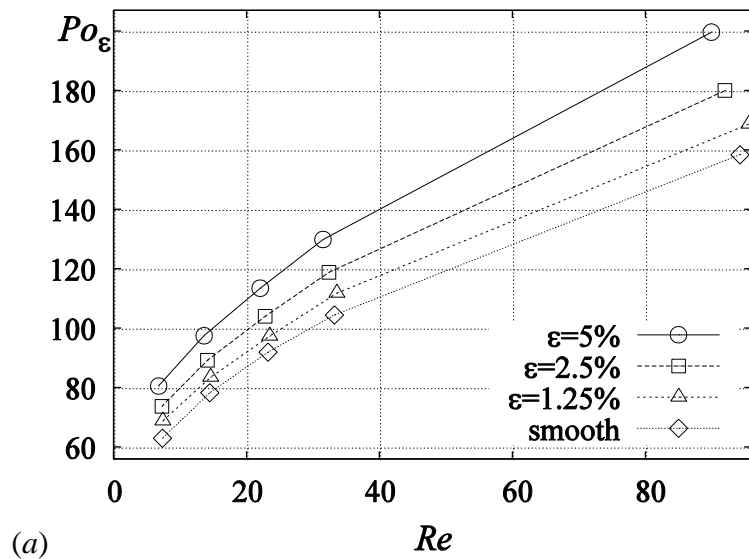




**Fig. 30.** Averaged Poiseuille number  $Po_\epsilon$  via averaged  $Re$ : (a)  $p_e/p_0 = 0.33$ , (b)  $p_e/p_0 = 0.5$ .

This clearly suggests that compressibility effect plays a dominant role for a considered geometry. It should be noticed that the change of slope of  $Po_\epsilon$  plot can be observed at low values of Mach number (see Fig. 30b), probably, due to an increase of the rarefaction effect on a gas flow.

In addition, Fig. 31 shows the hybrid  $Po_\epsilon$  averaged over a whole rough sector  $L^*$  as a function of Reynolds number  $Re$  averaged over the same sector at pressure ratios  $p_e/p_0 = 0.33$  and 0.5, respectively. Poiseuille number increases with  $Re$ ; due to eq. (90), this also means, considering the relationship between  $Re$  and  $Kn$  (eq. (96)), an increase in Poiseuille number related to a decrease in Knudsen number.



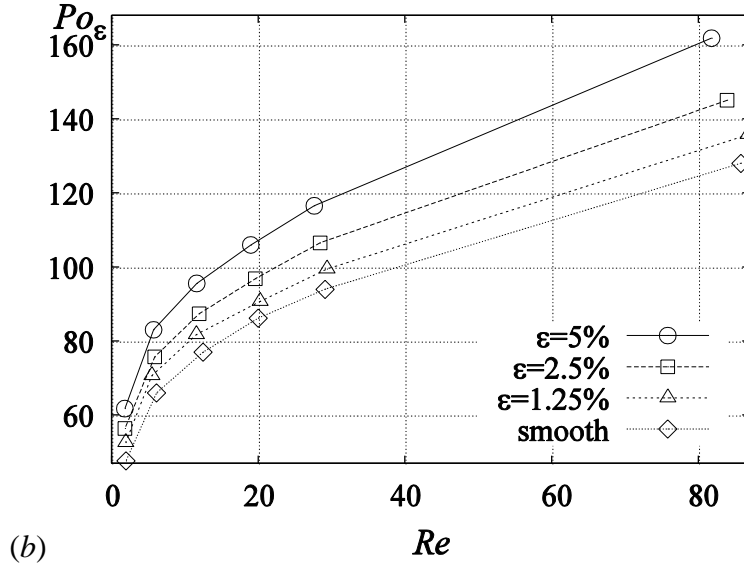
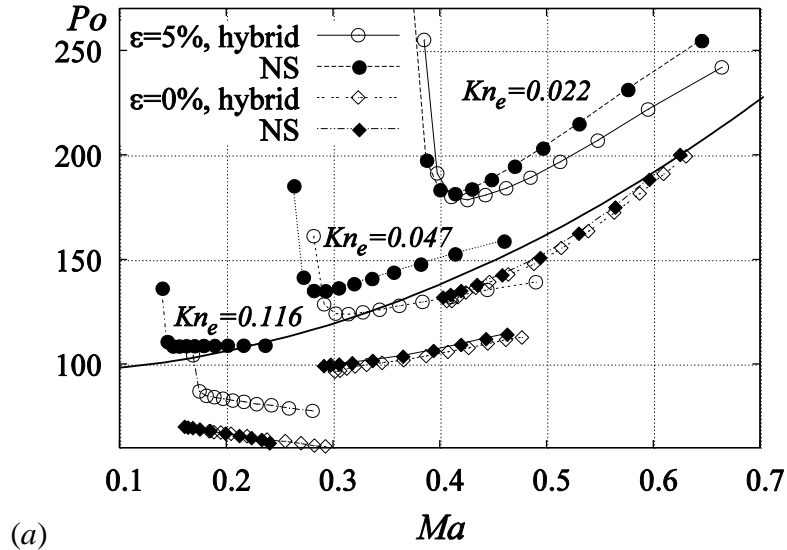


**Fig. 31.** Averaged Poiseuille number  $Po_\epsilon$  via averaged  $Re$ : (a)  $p_e/p_0 = 0.33$ , (b)  $p_e/p_0 = 0.5$ .

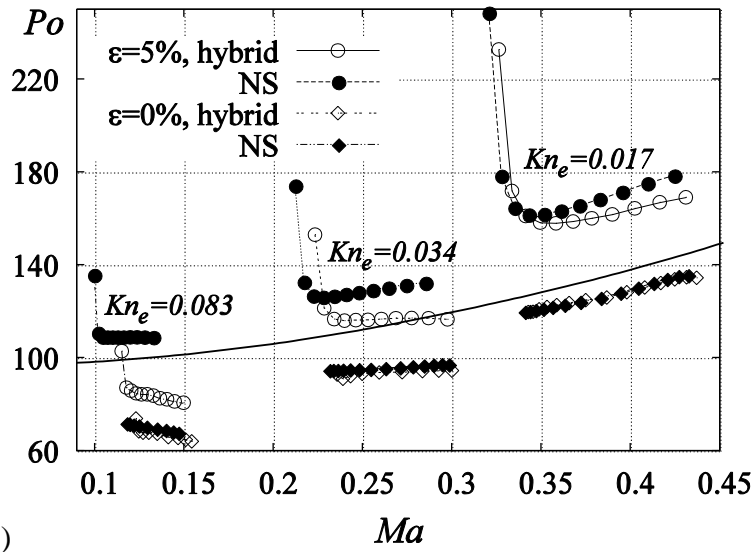
For a lower pressure ratio (i.e. higher actual  $Ma$ ), but comparable width of  $Re$  range, averaged Poiseuille number plot shows a much steeper slope. This also confirms that compressibility is a dominant factor.

For deeper understanding of the compressibility effect it is worth to analyse the behaviour of local Poiseuille number. In Fig. 32, the Poiseuille number averaged over each rough element for relative roughness  $\epsilon = 5\%$  and pressure ratios  $p_e/p_0 = 0.33$  and  $0.5$ , compared with smooth surface channel  $Po$ , is plotted as a function of the cross section averaged Mach number. The local  $Po$  is computed using formula (90) applied between the inlet and outlet sections of each rough module. Since the Mach number increases along the channel, we have the lowest  $Ma$  corresponds to the inlet of the rough sector, while the highest  $Ma$  is located at its exit. At the rough sector inlet the developing flow yields a quick decrease in Poiseuille number. As soon as this transition is completed (i.e., the minimum in the Poiseuille number  $Po$  curve),  $Po$  becomes a monotone function of  $Ma$ .

As can be seen in Fig. 32 the computed data lie in a relatively narrow band, especially for relatively low Knudsen numbers, thus confirming that Mach number is the dominant parameter, as suggested in [59, 63, 64] as well. Similar behaviour of local Poiseuille number vs. Mach number was also observed in [72] using a pure kinetic S-model solver.



(a)



(b)

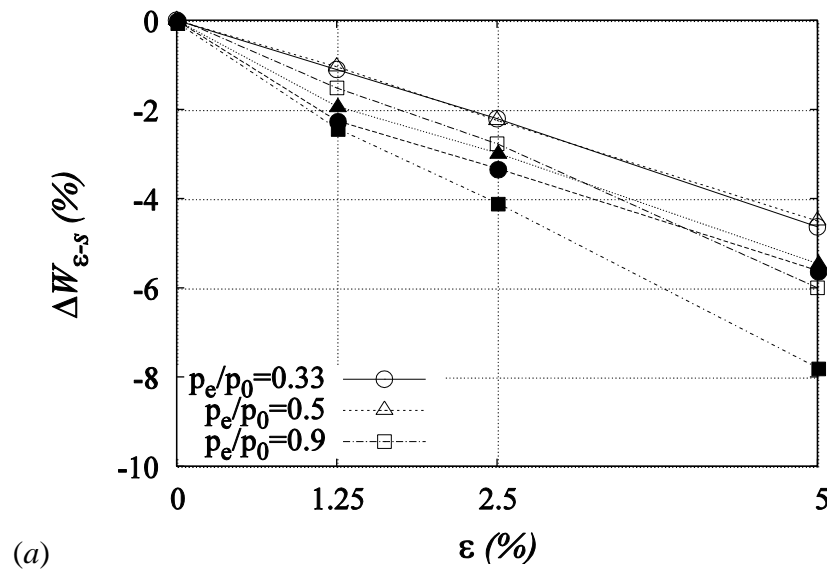
**Fig. 32.** Averaged over each rough element Poiseuille number  $Po$  via cross section averaged Mach number  $Ma$  at  $p_e/p_0 = 0.33$  (a) and  $0.5$  (b) for  $\varepsilon = 0$  and  $\varepsilon = 5\%$ : NS, solid symbols; hybrid, empty symbols

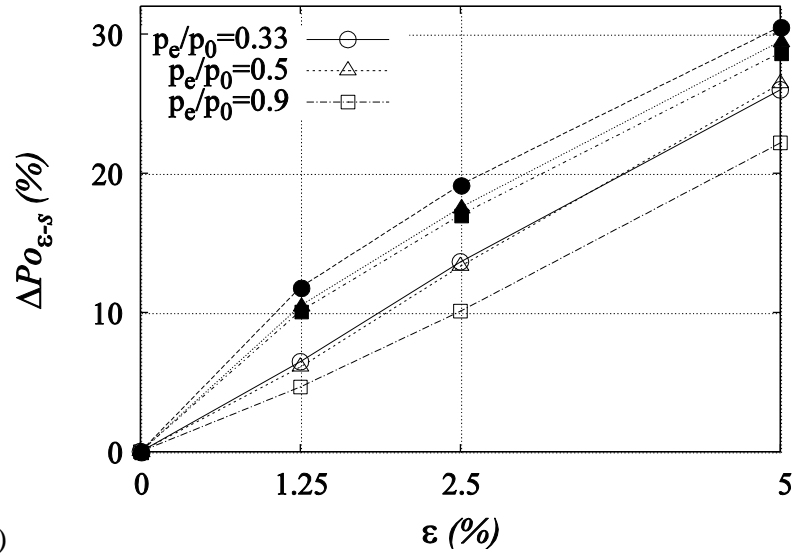
Furthermore, the comparison with a correlation equation (94) for smooth channel of Asako et al. [44] shows good agreement for  $Ma$  in the range from 0.3 to 0.63 and low values of  $Kn_e$ . When Knudsen number increases the difference becomes larger and local  $Po$  are lower than that obtained from the Asako's expression. This is due to the rarefaction effect, which is not included in the Asako's model [44], since, as was shown in Fig. 27, the rarefaction alleviates the friction effect of the wall on the gas flow.

As was demonstrated previously in Figs. 30 the impact of compressibility, especially at low pressure ratios is much more significant than the variation due to the roughness effect. The plots of local Poiseuille number  $Po$  vs.  $Ma$  shown in Fig. 32 confirm this observation: in particular, local  $Po$  at  $Ma \approx 0.66$  is two times higher than at  $Ma \approx 0.3$ , while the increase of  $Po$  value between rough (with  $\varepsilon = 5\%$ ) and smooth surface channels at the same  $Ma \approx 0.3$  is at most 25%.

It should mention that the difference between hybrid and NS solutions grows with Knudsen number. As demonstrated in Fig. 32, for low values of  $Kn$ ,  $Kn_e = 0.017$  and  $0.022$ , hybrid and NS computed local Poiseuille numbers for both smooth and rough channels are close to each other. For higher  $Kn$  values,  $Kn_e = 0.034$  and  $0.047$ , there is appreciable difference between NS and hybrid plots of rough surface  $Po$  number, while  $Po$  plots for smooth surface channel for both NS and hybrid solvers almost coincide.

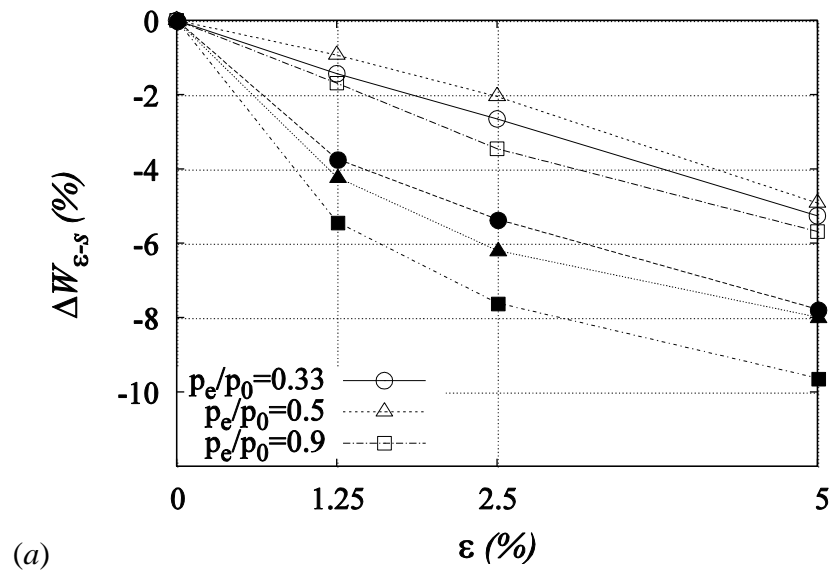
Thus, for weakly rarefied flow, and for the same value of local  $Ma$  both hybrid and NS solutions offer the same value of  $Po$ , for both smooth and rough channels. On the other hand, for higher rarefaction NS solver overestimates the roughness effect.

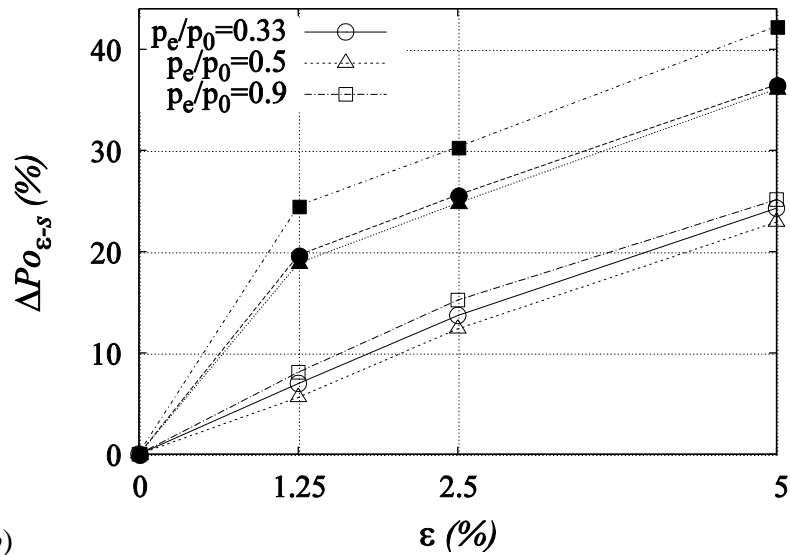




**Fig. 33.**  $\Delta W_{\epsilon-s}$  and  $\Delta P_{o_{\epsilon-s}}$  via relative roughness  $\epsilon$  at  $Kn_e = 0.017-0.0217$ : NS, solid symbols; hybrid, empty symbols

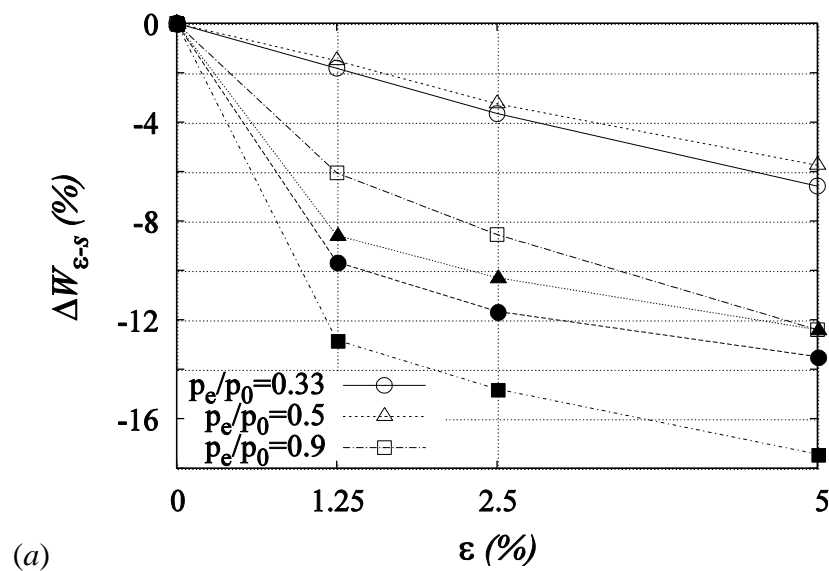
To quantitatively estimate the coupling effect of compressibility and roughness a deviation for global mass flow rate and Poiseuille number  $\Delta(W, Po)_{\epsilon-s}$  (see eq. (98)) in percent for different pressure ratios and few rarefaction level are shown in Figs. 33-35. As expected, the maximum deviation for both mass flow rate and Poiseuille number occurs for largest relative roughness height  $\epsilon = 5\%$ . Starting from smooth channel values the increase of roughness height  $\epsilon$  results in a decrease of mass flow rate and an increase of the Poiseuille number, due to an increase of friction effect of the wall on the gas flow.





**Fig. 34.**  $\Delta W_{\epsilon-s}$  and  $\Delta P_{O_{\epsilon-s}}$  via relative roughness  $\epsilon$  at  $Kn_e = 0.047-0.05$ : NS, solid symbols; hybrid, empty symbols.

As was mentioned before, when the roughness height growth the Poiseuille number variation is much more significant than the variation in the mass flow rate. In particular, for  $Kn_e \approx 0.02$  (see Fig. 33) maximum mass flow rate deviation  $\Delta W_{\epsilon-s}$  is 6% while Poiseuille number deviation  $\Delta P_{O_{\epsilon-s}}$  is 26%. Further, with Knudsen number increase (see Figs. 34 and 35) maximum deviations increase up to 12.4% for mass flow rate and around 30% for Poiseuille number.



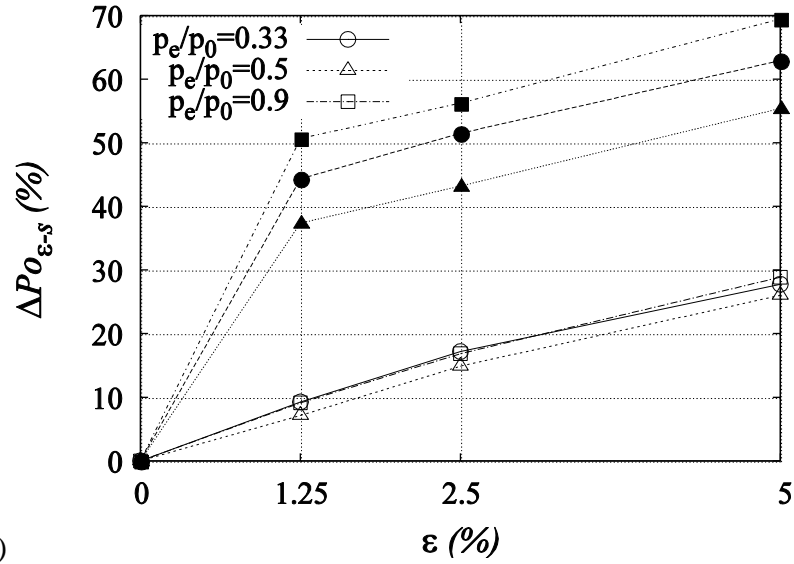


**Fig. 35.**  $\Delta W_{\varepsilon-s}$  and  $\Delta P_{O_{\varepsilon-s}}$  via relative roughness  $\varepsilon$  at  $Kn_e = 0.083-0.11$ : NS, solid symbols; hybrid, empty symbols.

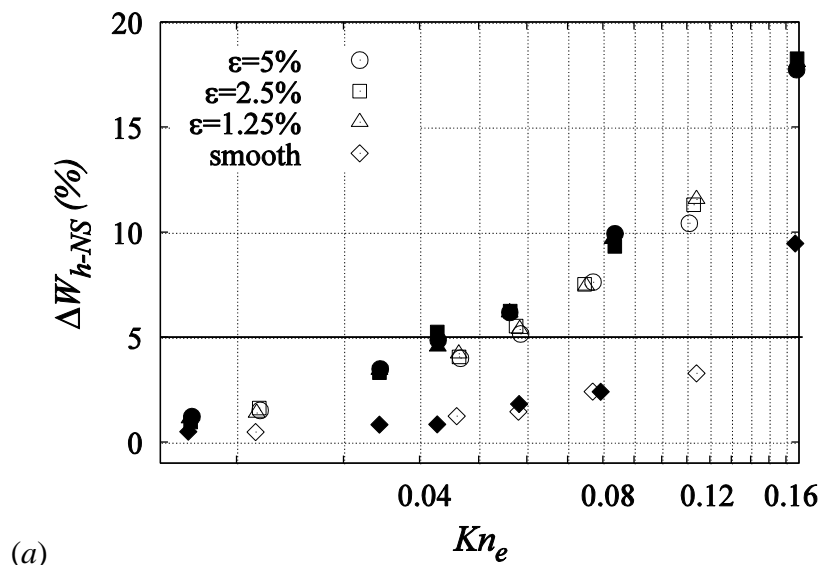
As can be seen in Figs. 33-35 the compressibility effect alleviates the friction effect of the rough wall on the flow in terms of the mass flow rate. For low pressure ratios  $p_e/p_0 = 0.33$  and  $0.5$  a deviation due to increase of relative roughness height for mass flow rate  $\Delta W_{\varepsilon-s}$  is smaller than for nearly incompressible flow ( $p_e/p_0 = 0.9$ ). In particular, for lowest pressure ratio  $p_e/p_0 = 0.33$  the minimum deviation  $\Delta W_{\varepsilon-s}$  is 4.5% (see Fig. 33) and further increases up to 6.6% when rarefaction level increase (Fig. 35). For nearly incompressible flow ( $p_e/p_0 = 0.9$ )  $\Delta W_{\varepsilon-s}$  is higher and equals 6% even for low  $Kn$  and increase up to 12.3% when  $Kn$  number increases (Fig. 35). Thus, the compressibility effect acts in opposite to the rarefaction effect direction (see Fig. 28) reducing a friction effect of the rough wall, thus, resulting in the less increase of mass flow rate deviation from smooth surface values when  $Kn$  number increase.

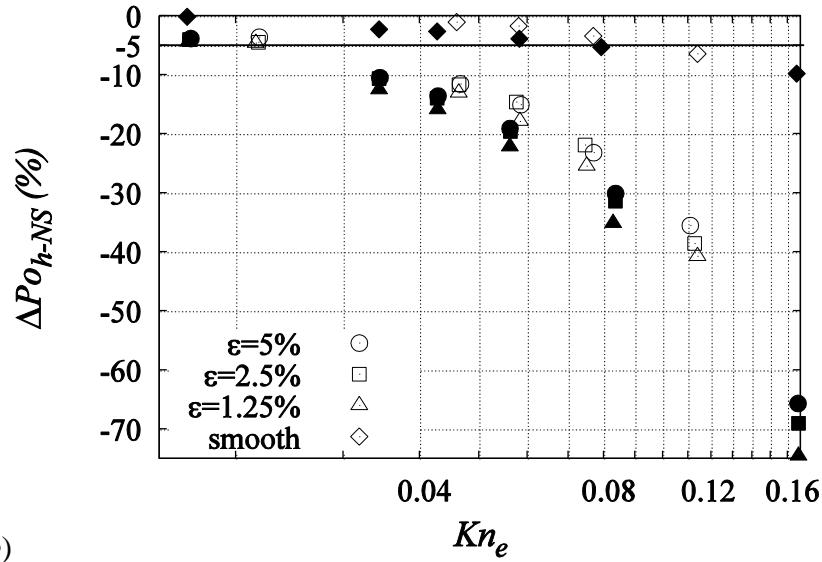
As was shown before the Poiseuille number variation in compressible flow is much more sensitive to Mach number increase than the roughness variation. Indeed, the maximum deviation  $\Delta P_{O_{\varepsilon-s}}$  (for  $\varepsilon = 5\%$ ) from smooth channel  $P_o$  weakly depends on the pressure ratio value, except a lowest rarefied flow case (see Fig. 33), when a maximum deviation  $\Delta P_{O_{\varepsilon-s}}$  is around 26% for  $p_e/p_0 = 0.33$  and  $0.5$  and around 22% for  $p_e/p_0 = 0.9$ . When Knudsen number increases (see Figs. 34 and 35) the maximum deviation  $\Delta P_{O_{\varepsilon-s}}$  growth up to 27-30% and is of the same order

for all considered pressure ratios. Thus, for the considered range of Knudsen number and pressure ratios a roughness effect on the flow in terms of Poiseuille number weakly depends on  $p_e/p_0$ . This confirms previous conclusion (see Fig. 30-32), that for compressible flow the effect of compressibility (increase of  $Po$  with  $Ma$ ) is more visible than the roughness effect. It should be noticed that as in the case for mass flow rate the compressibility effect reduces rarefaction effect on  $Po$  number deviation. Indeed, for incompressible flow  $p_e/p_0 = 0.9$  maximum  $\Delta Po_{\varepsilon-s}$  varies from 22% for local exit  $Kn_e = 0.02$  to 30% for  $Kn_e = 0.1$ , while for lowest pressure ratio  $p_e/p_0 = 0.33$   $\Delta Po_{\varepsilon-s}$  varies from 26% for  $Kn_e = 0.0217$  to 27.8% for  $Kn_e = 0.11$ .

As expected, NS solver overestimates Poiseuille number and underestimates mass flow rate when relative roughness height  $\varepsilon$  growth. Even for relatively low  $Kn_e$  equals 0.0217 and  $p_e/p_0 = 0.33$  NS solver offers deviation from smooth surface channel data around 6% for mass flow rate and 32% for  $Po$  number.

Figure 36 quantitatively demonstrates the difference between hybrid and NS solvers as function of local exit Knudsen number. It can be seen that a deviation of NS solution from hybrid one exceeds 5% for mass flow rate at  $Kn_e = 0.05$  and significantly earlier for Poiseuille number at  $Kn_e = 0.016$ . It should be noticed that in case channel with a smooth surface deviations for both mass flow rate and  $Po$  number are less than 5% up to Knudsen number around 0.1, i.e. in the region where first order slip boundary condition is commonly used.





(b) **Fig. 36.**  $\Delta(W, Po)_{h-NS}$  via exit Knudsen number  $Kn_e$ :  $p_e/p_0 = 0.33$ , empty symbols;  $p_e/p_0 = 0.5$ , solid symbols.

## 5.5. Conclusion

A hybrid solver based on the direct numerical solution of the S-kinetic equation coupled to a Navier-Stokes model was applied for the near wall modelling. It was found that the breakdown criterion based on the modified gradient length Knudsen number is more suitable for the boundary value problems.

For the smooth channel flow it was shown that hybrid code gives results close to full kinetic solutions for flow regimes where the Navier-Stokes solution fails. The obtained speed up, with respect to full S -model solutions, is between 2 and 5, although strongly depends on the size of the kinetic region.

Investigation of the roughness effect under Mach numbers from nearly incompressible to choked flow conditions  $0.001 \leq Ma \leq 0.62$  and exit Knudsen number ranging from 0.01 to 0.166 using hybrid solver has been done. It was found that rarefaction enhance roughness effect, especially in transitions regime. The compressibility is more dominant effect in comparison with the roughness one. Moreover, if a surface roughness is taken in to consideration even for relatively low values of the Knudsen number ( $Kn = 0.02$ ) based on the channel height, the accuracy of the NS solution provided with first order slip boundary conditions is questionable,

probably, due to the smaller scale effects related to the roughness peaks, while for a smooth surface the NS solution is reliable for  $Kn$  up to 0.05 (deviation from kinetic solution not exceed 5%).

Thus, the use of a hybrid solver, coupling a kinetic solution in the near wall region around the roughness peaks with a “cheaper” Navier - Stokes solution for the core flow, allows for a decrease of the computational expenses in comparison with pure kinetic solutions, while preserving a correct description of the gas-rough solid surface interaction.

## Conclusions

In the present work a sustainable multiscale solver based on the coupling solvers for the S-model kinetic equation and Navier-Stokes equations, allowing flexible changing the size of continuum and kinetic domains (depending on the flow regime) was elaborated. The code is accelerated by parallelization using MPI (Message Passing Interface) for computation on multiprocessors systems, thus making it tractable for complex two -dimensional flow problems. The present solver has been validated by applying to a well known problem: gas flow through the slit for a wide range of pressure ratios (including flow into vacuum) and Knudsen numbers. For the considered problem the hybrid solution was proved to be reliable even for regimes where Navier-Stokes solution completely fails.

The good efficiency of hybrid solver (CPU time reduction from 10 to 1.4 times) was demonstrated in comparison with pure kinetic solutions, although it strongly depends on the size of the kinetic region. It should be noticed that the use of the full Boltzmann equation instead its S-model would obviously provide even higher computational efficiency due to higher dimension of velocity space for the Boltzmann equation.

Furthermore, the hybrid solver has been applied for a classical engineering problem: compressible gas flow through the channel with a rough surface. Hybrid results demonstrated good agreement with open literature data. In particular, it was observed, the increase of Poiseuille number with relative roughness size increase and decrease of Poiseuille number with Knudsen number increase. Moreover, the compressibility is more dominant effect in comparison with the roughness one.

The reliability of first order slip boundary conditions for the simulation of flows along of fine-textured geometries was estimated. It was found that if surface roughness is taken in to consideration even for relatively low values of the Knudsen number ( $Kn = 0.02$ ) based on the channel height, the accuracy of the NS solution coupled with the first order slip boundary

conditions is questionable, probably, due to the smaller scale effects related to the roughness peaks, while for smooth surface the NS solution is reliable for  $Kn$  up to 0.05 (deviation from kinetic solution not exceed 5%).

It can be concluded that the elaborated hybrid solver is very promising tool for different engineering problems starting from MEMS to aerospace applications, since it provides solution with accuracy close to a pure kinetic one while computational expenses in terms of time and memory requirements are significantly lower. It should be noticed that an optimization (increase of efficiency) of hybrid solver is in author's opinion still open issue. Moreover, although the present work is devoted to MEMS application, it will be interesting to apply developed solver to other problems, e.g. hypersonic compressible flow.

## References

- [1] P. Le Tallec, F Mallinger, Coupling Boltzmann and Navier-Stokes equations by half fluxes J. Comput. Phys. 136 (1997) 51-67.
- [2] H. A. Carlson, R. Roveda, I. D. Boyd, G. V. Candler, A Hybrid CFD-DSMC Method of Modeling Continuum-Rarefied Flows, AIAA (2004) 2004-1180.
- [3] H. S. Wijesinghe, R. Hornung, A. L. Garsia, H. N. Hadjiconstantinou, Three-dimensional Hybrid Continuum-Atomistic Simulations for Multiscale Hydrodynamics J. Fluids Eng. 126 (2004) 768–777.
- [4] F. La Torre, S. Kenjereš, J-L Moerel, C.R. Kleijn, Hybrid simulations of rarefied supersonic gas flows in micro-nozzles. Comput.&Fluids 49 (2011) 312–322
- [5] R. Roveda, D.B. Goldstein, P.L. Varghese, Hybrid Euler/direct simulation Monte Carlo calculation of unsteady slit flow, J. Spacecraft Rockets 37 (6) (2000), 753-760.
- [6] T.E. Schwartzenuber, I. D. Boyd, A hybrid particle-continuum method applied to shock waves. J. Comput. Phys. 215 (2006) 402–416
- [7] I.D. Boyd, Predicting Breakdown of the Continuum Equations Under Rarefied Flow Conditions. AIP Conference Proceedings 663 (2003) 899–906.
- [8] V.I. Kolobov, R.R. Arslanbekov, V.V. Aristov, A.A. Frolova, S.A. Zabelok Unified solver for rarefied and continuum flows with adaptive mesh and algorithm refinement J. Comput. Phys. 223 (2007) 589–608.
- [9] V.V. Aristov, A.A. Frolova, S.A. Zabelok, R.R. Arslanbekov, V.I. Kolobov. Comparative study for rarefied gas flow into vacuum through a short circular pipe. Vacuum 86(11) (2012) 1717–24.
- [10] O. Rovenskaya, G.Croce (2013): Coupling Kinetic and Continuum Equations for Micro Scale Flow Computations, Heat Transfer Engineering, 34:2-3, 192-203 DOI:10.1080/01457632.2013.703542

- [11] O. Rovenskaya, G. Croce Numerical Investigation of Microflow Over Rough Surfaces: Coupling Approach J. Heat Transfer Vol. 135, 10 (2013) 101005 DOI: 10.1115/1.4024500
- [12] O. Rovenskaya, G. Croce 2014 Application a hybrid solver to gas flow through a slit at arbitrary pressure ratio Volume 109, November 2014, Pages 266–274, DOI: 10.1016/j.vacuum.2014.04.018
- [13] N. Crouseilles, P. Degond, M. Lemou, A hybrid kinetic-fluid model for solving the gas dynamics Boltzmann-BGK equation, J. Comput. Phys. 199 (2004) 776-806.
- [14] A.E. Beylich, Solving the kinetic equation for all Knudsen numbers. Phys. Fluids 12 (2000) 444–465.
- [15] A.M. Bishaev and V.A. Rykov. Solution of steady kinetic problems at moderate and small Knudsen numbers. USSR Comput. Math. Math. Phys., 15(1):172-182, 1975.
- [16] A.M. Bishaev and V.A. Rykov. Recondensation of a monatomic gas at low Knudsen numbers. USSR Comput. Math. Math. Phys., 18(3):18219, 1978.
- [17] J.Y. Yang and J.C. Huang. Rarefied flow computations using nonlinear model Boltzmann equations. J. Comput. Phys., 120(2):323-339, 1995.
- [18] L. Mieussens. Discrete-velocity models and numerical schemes for the Boltzmann BGK equation in plane and axisymmetric geometries. J. Comput. Phys., 162(2):429-466, 2000.
- [19] Yu.A. Anikin, O.I. Dodulad, Yu.Yu. Kloss, D.V. Martynov, P.V. Shuvalov, and F.G. Tcheremissine. Development of applied software for analysis of gas flows in vacuum devices. Vacuum, Special Issue "Vacuum Gas Dynamics: Theory, experiments and practical applications", 86(11):1770-1777, 2012.
- [20] V.A. Titarev. Implicit high-order method for calculating rarefied gas flow in a planar microchannel. J. Comput. Phys., 231(1):109-134, 2012.
- [21] V.A. Titarev. Efficient deterministic modelling of three-dimensional rarefied gas flows. Commun. Comput. Phys., 12(1):161-192, 2012.

- [22] C. Cercignani, Rarefied gas dynamics: From basic concepts to actual calculations, Cambridge University Press, Cambridge, 2000.
- [23] S. Chapman, T.G. Cowling, The mathematical theory of nonuniform gases, Univ. Press, Cambridge, 1990.
- [24] Garcia A.L., Alder B. J. 1998 Generation of the Chapman–Enskog Distribution J. of Comput. Phys. 140, 66–70 (1998)
- [25] Tiwari S, Klar A, Hardt S 2009, A particle-particle hybrid method for kinetic and continuum equations J. of Comput. Phys. 228 7109-7124
- [26] E.M. Shakhov, Generalization of the Krook kinetic relaxation equation. Fluid Dyn. 3 (1968) 95-96.
- [27] Bhatnagar PL, Gross EP, Krook MA. A model for collision processes in gases Physical Review 1954; 94: 511–525.
- [28] Filbet F, Jin S. A class of asymptotic preserving schemes for kinetic equations and related problems with stiff sources. Journal of Computational Physics 2010; 229: 7625-7648.
- [29] Puppo G, Pieraccini S. Implicit-explicit schemes for BGK kinetic equations. Journal of Scientific Computing 2007; 32: 1-28.
- [30] V.P. Kolgan. Application of the minimum-derivative principle in the construction of finite-difference schemes for numerical analysis of discontinuous solutions in gas dynamics. Transactions of the Central Aerohydrodynamics Institute, 3(6):68-77, 1972. in Russian.
- [31] V.P. Kolgan. Application of the principle of minimizing the derivative to the construction of finite-difference schemes for computing discontinuous solutions of gas dynamics. J. Comput. Phys., 230(7):2384{2390, 2011.
- [32] V.P. Kolgan. Finite-difference schemes for computation of three dimensional solutions of gas dynamics and calculation of a ow over a body under an angle of attack. Transactions of the Central Aerohydrodynamics Institute, 6(2):1-6, 1975. in Russian.

- [33] K. Qu, C. Shu, Y.T. Chew Lattice Boltzmann and Finite Volume Simulation of Inviscid Compressible Flows with Curved Boundary *Adv. Appl. Math. Mech.*, 5 (2010), pp. 573-586
- [34] G.D. Van Albada, B. Van Leer, W. W. Roberts, A comparative study of computational methods in cosmic gas dynamics, *Astron. Astrophys.*, 108 (1982), 76–84.
- [35] Croce, G., 1995, “Viscous 3D Cascade Flow Analysis Using an RNG Algebraic Turbulence Mode,” ASME Paper No. 95-CTP-78
- [36] T.H. Pulliam Artificial dissipation models for the Euler equations. , *J. AIAA* 24 (1986) 1931-1940.
- [37] Hirsh, C., Numerical computation of internal and external flows. John Wiley& Sons Ltd, Chichester, 1990.
- [38] V.A. Titarev, M. Dumbser, and S.V. Utyuzhnikov. Construction and comparison of parallel implicit kinetic solvers in three spatial dimensions. *J. Comput. Phys.*, 256:17-33, 2014.
- [39] V.V. Aristov and S.A. Zabelok. A deterministic method for solving the Boltzmann equation with parallel computations. *Comput. Math. Math. Phys.*, 42(3):406-418, 2002.
- [40] W. Kendall Beginning MPI (An Introduction in C) [Kindle Edition]
- [41] F. Sharipov, Rarefied gas flow through a slit: influence of the gas-surface interaction. *Phys Fluids* 1996;8(1):262–8..
- [42] F. Sharipov, Non-isothermal rarefied gas flow through a slit. *Phys Fluids* 9(6) (1997) 1804–10.
- [43] I. Graur, A.P. Polikarpov, F. Sharipov, Numerical modelling of rarefied gas flow through a slit into vacuum based on the kinetic equation. *Comput. & Fluids* 49(1) (2011) 87–92.
- [44] O. Rovenskaya, A. Polikarpov, I. Graur, Comparison of the numerical solutions of the full Boltzmann and S-model kinetic equations for gas flow through a slit. *Comput.& Fluids* 80 (2013) 71–78. <http://dx.doi.org/10.1016/j.compfluid.2012.05.007>

- [45] O. I. Rovenskaya. Comparative analysis of the numerical solution of full Boltzmann and BGK model equations for the Poiseuille flow in a planar microchannel. *Comput. & Fluids* 81 (2013) 45–56.
- [46] F. Sharipov, D.V. Kozak, Rarefied gas flow through a thin slit at an arbitrary pressure ratio. *Eur. J. Mech. B/Fluids* 30 (2011) 543–549.
- [47] Mala, G. M., Li, D., 1999, Flow characteristics of water in microtubes, *Int. J. Heat Mass Transfer*, 20, pp. 142–148.
- [48] Wu, P. Y., Little, W. A., 1983, Measurement of friction factor for the flow of gases in very fine channels used for microminiature Joule–Thomson refrigerator, *Cryogenics*, **23**, pp. 273–277.
- [49] Wu, P. Y., Little, W. A., 1984, Measurement of the heat transfer characteristics of gas flow in fine channel heat exchangers used for microminiature refrigerators, *Cryogenics*, **24**, pp. 415–420.
- [50] Choi, S. B., Barron, R. F., Warrington, R. O., 1991, Fluid Flow and Heat Transfer in Microtubes, *ASME J. Dyn. Syst., Measure., Control*, 32, p. 123.
- [51] Morini, G. L., 2004, Single-phase convective heat transfer in microchannels: a review of experimental results, *Int. J. Therm. Sci.*, **43**(7), pp. 631–651
- [52] Kandlikar, S., Schmitt, D., Carrano, A., Taylor, J., 2005, Characterization of Surface Roughness Effects on Pressure Drop in Single-Phase Flow in Minichannels, *Phys. Fluids*, **17** (10), pp. 1–11.
- [53] Croce, G., D'Agaro, P., Nonino, C., 2007, Three-dimensional roughness effect on microchannel heat transfer and pressure drop, *Int. J. Heat Mass Tran.*, **50**, pp. 5249–5259.
- [54] Turner, S.E., Lam, L.C., Faghri, M., Gregory, O.J., 2004, Experimental investigation of gas flow in microchannels, *ASME J. Heat Transfer*, **126**, pp. 753–762.

- [55] Lorenzini, G., Morini, G. L., Salvigni, S., 2010, Laminar, transitional and turbulent friction factors for gas flows in smooth and rough microchannels, *Int. J. Therm. Sci.*, **49**, pp. 248-255
- [56] Demsis, A., Prabhu, S.V., Agrawal, A., 2010, Influence of wall conditions on friction factor for flow of gases under slip conditions, *Experimental Therm. and Fluid Sci.*, **34**, pp. 1448-1455.
- [57] Tang, G. H., Li, Z., He, Y. L., Tao, W. Q., 2007, Experimental study of compressibility, roughness and rarefaction influences on microchannel flow. *Int. J. Heat Mass Tran.*, **50**, pp. 2282-2295.
- [58] Hu, Y., Werner, C., Li, D., 2003, Influence of Three-Dimensional Roughness on Pressure-Driven Flow through Microchannels. *ASME J. Fluid Eng.*, **125**, pp. 871–879.
- [59] Croce, G., D’Agaro, P., 2005, Numerical simulation of roughness effect on microchannel heat transfer and pressure drop in laminar flow. *J. Phys. D: Appl. Phys.*, 38 (10), pp. 1518-1530.
- [60] Valses, R., Miana, J., Pelegay, L., Nunez, L., Putz, T., 2007, Numerical investigation of the influence of roughness on the laminar incompressible fluid flow through annular microchannels. *Int. J. Heat Mass Tran.*, **50**, pp. 1865–1878.
- [61] Kleinstreuer, C., Koo, J., 2004, Computational analysis of wall roughness effects for liquid flow in micro-conduits. *ASME J. Fluid Eng.*, **126**, pp. 1–9.
- [62] Koo, J., and Kleinstreuer, C., 2005, Analysis of surface roughness effects on heat transfer in micro-conduits, *Int. J. Heat Mass Tran.*, **48**, pp. 2625–2634.
- [63] Sun, H., and Faghri, M., 2003, Effect of surface roughness on nitrogen flow in a microchannel using the direct simulation Monte Carlo method. *Numer. Heat Tran. Part A*, **43**, pp. 1–8.
- [64] Cao, B., Chen, M., Guo, Z., 2004, Rarefied Gas Flow in Rough Microchannels by Molecular Dynamics Simulation. *Chinese Phys. Lett.*, **21**(9), pp. 1777–1779.

- [65] Liu, C., Yanga, J., Y. Ni, 2011. A multiplicative decomposition of Poiseuille number on rarefaction and roughness by lattice Boltzmann simulation. *Comp. and Math. with Applic.*, **61**, pp. 3528–3536.
- [66] Ji, Y., Yuan, K., Chung, J., 2006. Numerical Simulation of Wall Roughness on Gaseous Flow and Heat Transfer in a Microchannel. *Int. J. Heat Mass Tran.*, **49**, pp. 1329–1339, 2006.
- [67] Croce, G., and D'Agaro, P., 2007. Compressibility and Rarefaction Effects on Pressure Drop in Rough Microchannels. *Heat Transfer Eng.*, **28** (8–9), pp. 688-695
- [68] Hakak Khadem, M., Shams, M., and Hossainpour, S., 2009, Effects of Rarefaction and Compressibility on Fluid Flow at Slip Flow Regime by Direct Simulation of Roughness, *Int. J. Aero. Mech. Eng.*, **3**(4), pp. 204-210.
- [69] Asako, Y., Pi, T., Turner, S. E., and Faghri, M., 2002, Effect of compressibility on gaseous flows in micro-channels, *Int. J. Heat Mass Tran.*, **46**, pp. 3041–3050.
- [70] Croce, G., D'Agaro, P., 2009. Compressibility and Rarefaction Effects on Heat Transfer in Rough Microchannels. *Int. Journal of Thermal Sciences*, **48** (2), pp. 252-260
- [71] Colin, S., 2012. Gas Microflows in the Slip Flow Regime: A Critical Review on Convective Heat Transfer,” *ASME J. Heat Transfer*, **134** (2), pp. 1-13
- [72] Rovenskaya, O.I. Kinetic analysis of surface roughness in a microchannel. *Computers & Fluids* 77 (2013) 159–165 <http://dx.doi.org/10.1016/j.compfluid.2013.03.008>

## List of Publications

1. O. Rovenskaya, G. Croce (2013): Coupling Kinetic and Continuum Equations for Micro Scale Flow Computations, Heat Transfer Engineering, 34:2-3, 192-203  
DOI:10.1080/01457632.2013.703542
2. O. Rovenskaya, G. Croce Numerical Investigation of Microflow Over Rough Surfaces: Coupling Approach J. Heat Transfer Vol. 135, 10 (2013) 101005 DOI: 10.1115/1.4024500
3. O. Rovenskaya, G. Croce 2014 Application a hybrid solver to gas flow through a slit at arbitrary pressure ratio Volume 109, November 2014, Pages 266–274, DOI: 10.1016/j.vacuum.2014.04.018
4. O. Rovenskaya, A. Polikarpov, I. Graur, Comparison of the numerical solutions of the full Boltzmann and S-model kinetic equations for gas flow through a slit. Comput.&Fluids 80 (2013) 71–78. <http://dx.doi.org/10.1016/j.compfluid.2012.05.007>
5. O. I. Rovenskaya, Comparative analysis of the numerical solution of full Boltzmann and BGK model equations for the Poiseuille flow in a planar microchannel. Comput.& Fluids 81 (2013) 45–56.
6. O.I. Rovenskaya, Kinetic analysis of surface roughness in a microchannel. Computers & Fluids 77 (2013) 159–165 <http://dx.doi.org/10.1016/j.compfluid.2013.03.008>